Quantitative Assessment of Submodes of Stress Corrosion Cracking on the Secondary Side of Steam Generator Tubing in Pressurized Water Reactors: Part 2

R.W. Staehle‡, and J.A. Gorman***

ABSTRACT

The work in this article is part of a project to develop a quantitative description of stress corrosion cracking (SCC) on the secondary side of pressurized water reactor (PWR) steam generator tubing based on existing information from operating plants and from laboratory experiments. This work is the second step in developing a predictive model for SCC on the secondary side. The first step involved developing a statistical framework into which dependencies of the various submodes of SCC can be inserted. The results of the present work will lead to quantitative descriptions of corrosion processes that, in turn, will be incorporated into the statistical framework. The chemistry of heat-transfer crevices will then be assessed to determine the proper inputs to the dependencies of the various submodes of SCC, and these will be connected to bulk environments. The modeling here is directed toward predicting the early occurrence of SCC that is too shallow to be detected by nondestructive examination (NDE).

The various submodes of SCC considered in this article include: alkaline stress corrosion cracking (AkSCC), low-potential stress corrosion cracking (LPSCC), acidic stress corrosion cracking (AcSCC), high-potential stress corrosion cracking (HPSCC), lead stress corrosion cracking (PbSCC), low-valence stress corrosion cracking (S^{y-}SCC), organic stress corrosion cracking (OgSCC), doped steam stress corrosion cracking (DSSCC), and low-temperature stress corrosion cracking (LTSCC). To develop a model for each of these submodes, their dependencies on the seven primary variables are evaluated in this article; these variables are pH, potential, species, alloy composition, alloy structure, temperature, and stress. For some of these submodes, there is broad agreement in the literature on dependencies. In other cases there is some disagreement, but these are mostly related to lack of information or to inconsistencies among experiments that have been conducted under different conditions. To develop a framework for this discussion of submodes, supporting sections are included on designs of steam generators as they affect corrosion, bulk water chemistry as it relates to chemistry in heat-transfer crevices, and the chemistry of heat-transfer crevices. At the end of each section, the state of present knowledge is summarized including the lessons learned from service and laboratory experience. In addition, possible problems for future reliable performance as affected by corrosion are identified.

KEY WORDS: Alloy 600, Alloy 690, Alloy 800, heat-transfer crevices, secondary side, steam generator, stress corrosion cracking, water chemistry

TABLE OF CONTENTS

Part 1 of this manuscript, with the complete set of references, appeared in *Corrosion* 59, 11 (2003), p. 931-994.

‡ Corresponding author.
* 22 Red Fox Road, North Oaks, MN 55127.
** Dominion Engineering, Inc., 11730 Plaza America Drive, Suite 310, Reston, VA 20190.

Note References, figures, and tables are sometimes referred to out of order. This has been necessary first to maintain the integrity of sections and second to show connections among previous and succeeding sections.

0010-9312/04/000001/$5.00+$0.50/0

4.0 THE HEAT-TRANSFER CREVICE AND DEPOSITS

4.1 Background

This section describes the present knowledge of chemistry and physical conditions inside heat-transfer crevices and assesses the state of modeling.

The heat-transfer crevices, as shown in Figures 3, 4, 10, 11, 12, 13, 21, and 22, dominate the conditions that control the occurrence of corrosion on the secondary side. The chemical environments that accumulate inside these crevices, as well as the thermal, mechanical, and electrochemical conditions, determine whether corrosion can occur as well as its rate. Despite the importance of these crevices, the corrosion processes have eluded quantitative characterization; the extent of available characterizations is described in this section. This section addresses the step of "environmental definition," as it is used in the corrosion-based design approach (CBDA), which should be understood before selecting materials and which should be the basis for quantifying modes of corrosion.[124,147-148]

What is known about heat-transfer crevices as well as the means for dealing with their uncertainties include the following:

1. Some "Knowns" about Heat-Transfer Crevices —

a. The rates of failures at heat-transfer crevices, as well as for low-potential stress corrosion cracking (LPSCC) on the primary side, for Alloy 600 (UNS N06600)[(1)] with drilled hole carbon steel support plates are shown for a typical case in Figure 24. The occurrences of these failures follow Weibull cumulative distributions.[21] The rates of failure and their locations are well defined.
b. The superheat in heat-transfer crevices is the primary factor affecting concentration and the phase state of chemical species.
c. Stress corrosion cracking (SCC) failures are almost nonexistent in steam generators (SGs) with Alloy 800 (UNS N08800) tubes and stainless steel egg crate tube supports, although wastage has been a problem with phosphate water treatment.
d. Failures with Alloy 600MA occur in heat-transfer crevices in deep tubesheet crevices, at tube support plates (TSPs), and at top of tubesheets (TTSs).
e. Adding hydrazine (N_2H_4) has been found to reduce significantly the rate of SCC in some cases; this suggests that at least some of the SCC in heat-transfer crevices is affected by modest changes in the electrochemical potential.
f. Adding boric acid (H_3BO_3) reduces SCC somewhat, as shown in Figure 34; this suggests that the SCC depends on pH.
g. The calculated average pH in heat-transfer crevices tends to be in the mid-range due to the presence of silicates. This is based on hideout return data that is discussed in connection with Figure 53. However, laboratory testing shows that the pH at the tube surfaces is considerably more alkaline.
h. Widespread intergranular attack (IGA) and occasional SCC occur in the upper bundle of once-through steam generators (OTSGs) where the surfaces are superheated (Figures 8 and 25); IGA and SCC are not observed in the upper hot tubesheet crevice, which suggests that no aqueous phase is present.
i. Elevated concentrations of oxidants such as copper ions or copper oxides together with carbon steel TSPs and the presence of anions such as chlorides or sulfates produce extensive corrosion of the carbon steel that leads to denting, as shown in Figures 14, 15, and 21.
j. The extent of tube corrosion at TSPs decreases with increasing height of the TSP, as shown in Figure 18. With increasing height the superheat is decreased.
k. The range of potentials that occur in heat-transfer crevices in SGs is defined by the

[(1)] UNS numbers are listed in *Metals and Alloys in the Unified Numbering System*, published by the Society of Automotive Engineers (SAE International) and cosponsored by ASTM International.

NiO/Ni and H_2O/H_2 half-cell equilibrium potentials. This range, practically, is narrow, being in the range of 100 mV. The origin of this range is shown schematically in Figure 41. This is the nominal range of potentials if there are no other oxidants, such as Cu^{1+}, Cu^{2+}, and Fe^{3+}. During steady-state operation, about 2 ppb of Fe enters the SG in the feedwater, about half of which is Fe^{3+}. It is reasonable that some of this Fe^{3+} would enter crevices before being reduced by the N_2H_4. Higher potentials are especially likely just after startup when the concentrations of Fe^{3+} may be ten times higher than at steady state.

l. Packing of crevices with corrosion products and sludge can occur relatively early in SG life, producing mainly a local environment of superheated steam with possible droplets or films of water containing concentrated chemistries.

m. The range of aqueous chemistries calculated to occur in heat-transfer crevices is broad, and specific attribution of SCC to specific environments is not possible.

2. Some "Unknowns" about Heat-Transfer Crevices —

a. The relative extent and importance of the steam phase as the corroding medium inside heat-transfer crevices are not well defined nor is there significant published research to determine how the steam phase interacts with the average chemistry of heat-transfer crevices to produce corrosion.

b. The range of compositions of deposits and residual chemistries in heat-transfer crevices is not well defined, nor are there reliable rules, correlations, or other guides for their prediction. Although, as shown in Sections 4.5 and 4.6, there are some generally systematic patterns available from hideout return and analysis of deposits. The generality of these data is not clear.

c. The properties of line contact crevices, as shown in Figures 3, 10, and 13 with respect to concentrating impurities and forming superheated steam environments, are not well known; therefore, the bases for predicting performance in plants with such designs are not clear. However, some testing has been conducted to show that line contact crevices develop lower superheats and collect fewer deposits than drilled hole crevices; thus, some useful comparative information is available.

d. Most corrosion research, which has not utilized model boilers, applicable to the secondary side has been conducted in the liquid phase while the environments in heat-transfer crevices of operating steam generators are generally either two-phase or steam blanketed as illustrated in Figures 10 and 80. The importance of this local steam or two-phase condition has not been established.

e. Most corrosion research applicable to the secondary side has not been conducted at conditions where the hydrogen concentration is in the range of that sustained in operating SGs, as illustrated in Figure 42; therefore, data that have been taken without accounting for this condition, may not be applicable to operating conditions.

f. The effects of the coupling that occurs in crevices between the nickel alloy tubes and the steel materials of supports and tubesheets are not well understood. For example, this coupling could affect the potential at the tube surface, and thus influence the occurrence of SCC, e.g., LPSCC. Further, how the strength and influence of this coupling vary as the pH of the concentrated solutions change, e.g., become more acidic, are not known.

Thus, what is known about the local conditions in heat-transfer crevices is sparse in detail; but the available information plus engineering judgment have provided good bases for decisions. With regard to predicting the future performance of new steam generators with Alloy 690TT (UNS N06690) tubes, stainless steel supports, and line contact support crevices, the available information indicates that this combination will perform substantially better than previous steam generators with Alloy 600MA tubes and drilled hole carbon steel supports. However, the available information does not provide reliable bases for predicting the useful life of new steam generators nor their capacity to resist aggressive upset conditions that occasionally occur in plants.

4.2 Electrochemical Properties

The electrochemical potential in deaerated heat-transfer crevices can be readily bounded according to the approach in Figure 41, which shows that the potential at any pH must lie between the H_2O/H_2 and NiO/Ni half-cell equilibria, which are close together depending on the partial pressure of hydrogen. In view of the narrow range of possible potentials, only changes in pH inside heated crevices can affect the potential significantly unless other half cells are available for changing the potential. Such half cells that could occur in steam generators would be N_2/N_2H_4, Cu^{1+}/Cu, Cu^{2+}/Cu, and Fe^{3+}/Fe^{2+}.

Lumsden and coworkers[149-151] have measured open-circuit potentials in a heated crevice autoclave system using solutions containing sodium chloride (NaCl) and sodium hydroxide (NaOH) with additions of N_2H_4. Their results are shown in Figure 47 where they report measurements from adjacent surfaces in both the non-crevice and crevice locations. The val-

Test No.	Feedwater Containing NaCl Plus Additions	E_{crv} mV	E_{bulk} mV	Bulk $pH_{300°C}$
1	12 ppm NaCl, pH 5.54	–590	–460	5.54
2	12 ppm NaCl + 11 ppm NH_4Cl, pH 4.18	–320	–410	4.18
3	12 ppm NaCl + 200 ppm N_2H_4, pH 7.03	–630	–700	7.03
4	12 ppm NaCl + 11 ppm NH_4Cl + 200 ppm N_2H_4, pH 6.27	–410	–590	6.27

(a)

Test No.	Feedwater Containing NaOH Plus Additions	Time (h)	E_{crv} (mV)	E_{bulk} (mV)	Bulk $pH_{300°C}$
5	40 ppm NaOH, pH 8.46	2.5	–780	–690	—
		5	–820	–680	—
		16	–830	–640	8.46
6	0.4 ppm NaOH, pH 6.49	16	–590	–520	6.49
7	0.4 ppm NaOH + 2 ppm N_2H_4, pH 6.54	16	–730	–580	6.54

(b)

FIGURE 47. *Results from measurements of potential from a heated crevice experiment where environments have been prepared using pure deaerated feedwater to which combinations of NaCl, NH_4Cl, N_2H_4, and NaOH have been added. Potentials measured with an external silver/silver chloride (Ag/AgCl) reference electrode and results converted to SHE. Bulk temperature was 280°C. Surface heat fluxes produced temperatures of heated surfaces in the range of 320°C. Potentials in crevices were measured with heaters off (allowing the steam bubble to collapse and to establish electrical contact with the reference electrode), and the temperature of the crevice water was approximately 300°C. pH was calculated from MULTEQ.[51-53] From Lumsden, et al.[149-151]*

ues of pH were calculated here at 310°C using MULTEQ†.[51-53] The results in Figure 47 seem to follow qualitatively expected patterns although they are quantitatively not consistent. For example:

1. The electrochemical potential of a metal surface exposed to bulk water (E_{bulk}) decreases from –520 mV to –640 mV for a 100X change in the concentration of NaOH between Tests 6 and 5. While the change in potential, 120 mV, is in the right direction, it should be about 200 mV. On the other hand, in the same rows, the electrochemical potential of a metal surface exposed to the environment in a crevice (E_{crv}) changes in the right direction and by about 240 mV, which is close to the expectation of 110 mV/pH, although the amount of NaOH in the respective crevices is not known.
2. The change in potential upon the addition of ammonium chloride (NH_4Cl) for E_{bulk} is about a third of what it should be; whereas, E_{crv} changes more than predicted, assuming a proportionality of crevice to bulk concentration but is more in accordance with a magnitude expected based on the MULTEQ calculation of pH.
3. For Rows 5, 6, and 7 for NaOH solutions, E_{crv} is more alkaline than E_{bulk} for every case, and this is in accordance with expectations. Conversely, for Rows 2, 3, 4, E_{crv} is more acidic, as it should be, than E_{bulk}. The fact that E_{crv} is significantly lower in Row 1 (indicating a more alkaline environment) than E_{bulk} relative to the trends for the other chloride environments seems out of place.
4. Adding N_2H_4 as in Case 3 vs Case 1, Case 4 vs Case 2, and Case 7 vs Case 6 causes the potential to decrease, as it should. However, while these decreased potentials follow expected trends from the relatively low equilibrium potential for the N_2H_4 oxidation, the lowered potentials could result from the formation of H_2 from the decomposition of N_2H_4.

During the investigation of the potential inside and outside the crevice, Lumsden, et al.,[151] observed that the potential of the crevice would rise when the heaters were activated. This rise would continue, as noted in Figure 48, until the crevice was saturated with liquid. The potential would then drop to a value consistent with the crevice being wetted. It appears that the first stage of rise in potential is associated with the presence of steam in the crevice. When the potential dropped, the average potential in the crevice was observed by Lumsden to be about 274 mV below the potential of the external surface. The extraction of solution from the crevice at this point was measured to have a concentration of 28% Na^+ (280,000 ppm) relative to the input feedwater of 40 ppm NaOH.

Corrosion potentials in acidic and alkaline solutions have been measured by Kawamura and

† Trade name.

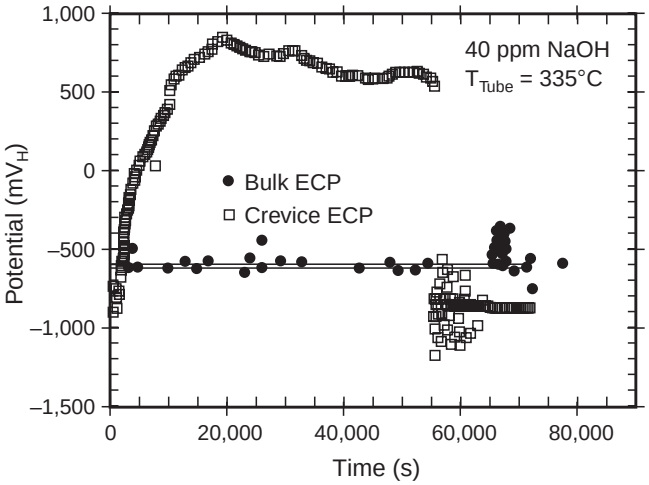

FIGURE 48. *Potential vs time for a heated crevice with potential probes inside and outside the crevice. Feedwater contains 40 ppm NaOH, and temperature of the molten salt heat-transfer fluid inside the tube was 335°C. Crevice packed to 50 v/o with diamond powder. From Lumsden, et al.*[151]

Hirano[152] over a range of temperatures. Their results in Figure 49 show generally that the potentials follow the slope of the temperature-dependent coefficient of the log of the hydrogen activity. A similar result was obtained by deBouvier, et al.,[153] from work on several alloys at 320°C, as shown in Figure 50.

4.3 Accumulation of Solutes and Solids in Crevices

Solutes concentrate substantially in heat-transfer crevices. The concentration of solutes depends mainly on the chemical identity of the species, the concentration of species in the bulk environment as shown in Figure 20, time, and heat flux. Limits of concentration of solutes are determined by the solubility limit and the volatility of the species being concentrated.

The chemical identity of species that concentrate has been studied by Takamatsu, et al.,[66] where they show in Figure 20 that the maximum concentration of impurity species in the crevice is proportional to the concentration in the environment and that the cations Na^+ and K^+ concentrate to a factor of ten greater than the anions Cl^- and F^-. Figure 20 shows that boron concentrates to more than an order of magnitude less than the Cl^- and F^- anions. These patterns seem to follow the vapor pressures. A similar result has been obtained by Shoda, et al.,[154] as shown in Figure 51(a) for data from six Japanese plants. Here, the cations of Na^+, K^+, Ca^{2+}, Mg^{2+}, as well as the SO_4^{2-} anion all seem to concentrate to about the same amount; whereas, the anions of F^- and Cl^- concentrate less, although the dependence is less clear than that shown in Figure 20. A similar pattern was observed by Lumsden, et al.,[149] as shown in Figure 51(b) for direct measurements at the Ohi

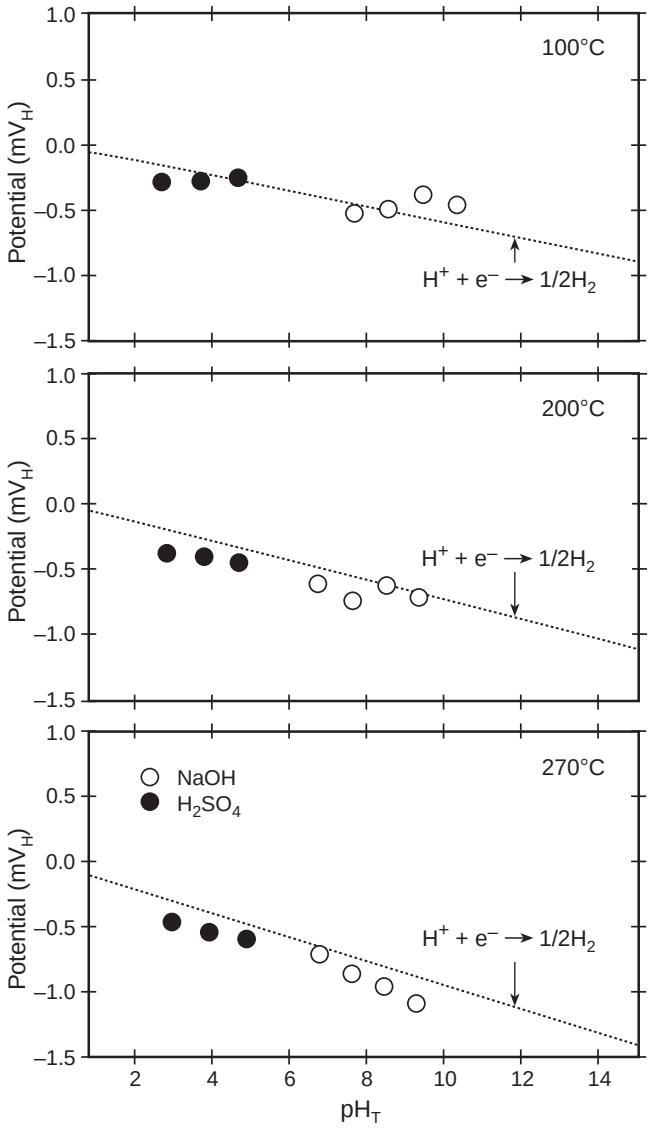

FIGURE 49. *Corrosion potential of Alloy 600 vs pH_T in deaerated NaOH and H_2SO_4 solutions where the NaOH used 1, 10, 100, and 1,000 ppm; the H_2SO_4 used 1, 10, and 100 ppm. Measurements taken with Ag/AgCl electrode and converted to SHE. pH_T determined with MULTEQ. From Kawamura and Hirano.*[152]

plant in Japan, although there was no discernible difference between the anions and cations.

In general, the concentration of chemical species has been found to be correlated by the product of bulk concentration times exposure duration. Such a pattern is illustrated in Figure 51(c) for chloride from the work of Mann and Castle,[155] as compared with the theoretical calculations of Millett and Fenton.[156] Lumsden, et al.,[149] found a similar pattern for NaOH, as shown in Figure 51(d). In the work of both Mann and Lumsden, the rate of concentration declines after some time and begins to saturate when ppm concentrations are present in the feedwater.

The effect of heat flux on the concentration of species has been studied by Kawamura and Hirano[152]

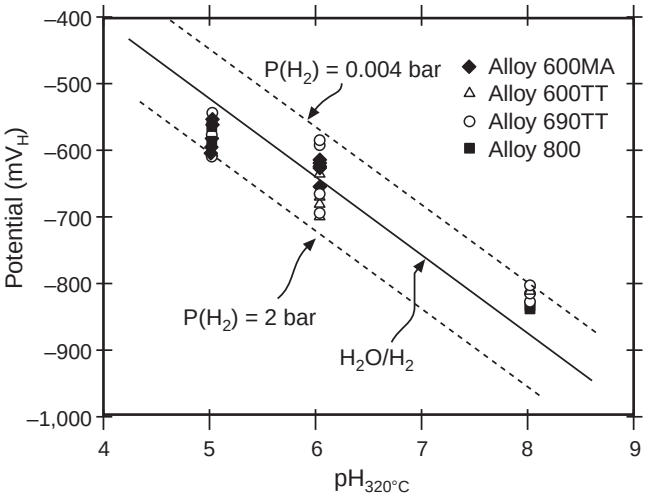

FIGURE 50. *Corrosion potential of four alloys vs pH adjusted by varying relative concentrations of H_2SO_4 and NaOH. Tests conducted at 320°C. Ag/AgCl electrode used and converted using a direct correlation with a hydrogen electrode. Hydrogen removed by cold trapping. pH_T determined with MULTEQ. From deBouvier, et al.[153] Courtesy of TMS, Warrendale, Pennsylvania.*

for sulfuric acid (H_2SO_4) and NaOH at 270°C, as shown in Figure 52. NaOH was found to concentrate more than H_2SO_4. This result is consistent with the work shown in Figure 20 as well as that in Figure 51(a) where the anions of Cl^- and F^- are shown to concentrate less than the cations and the anion of SO_4^{2-}. The work of Kawamura and Hirano shows that the maximum concentration is generally independent of bulk temperature, given sufficiently high feedwater concentrations, suggesting that heat flux is the dominating influence, as shown in Figure 18 where the failure rate is shown for three plants as a function of height of the tube support. This is illustrated by the set of data in Table 7 from an analysis based on their results. Using the crevice potentials reported in Figure 5-1 of Kawamura and Hirano[152] for 10 ppm NaOH at 270°C, and using their assumption that the potential is set by the hydrogen equilibrium line in their Figure 49 for 270°C, the estimated pH_T (pH at temperature and calculated or measured at temperature) and concentrations of sodium vary, as shown in Table 7, as a function of the heat flux. This dependence shows that higher heat flux leads to higher concentrations; thus, for NaOH-contaminated bulk water, higher heat flux produces a higher crevice pH.[157]

4.4 pH in Heat-Transfer Crevices

The pH in crevices has been estimated by Shoda, et al.,[154] and by Ollar and Viricel-Honorez,[158] as shown in Figure 53, by measuring hideout return and then using MULTEQ to calculate the pH in the crevices. Figure 53(a) shows results from nine Japanese plants where the pH was calculated at 280°C for four plants with partial-flow condensate polishers and six plants with full-flow condensate polishers, with measurements for several cycles for most plants. The data are generally in the neutral range although somewhat scattered. Shoda, et al., regard the results as indicating a benign environment in the heat-transfer crevices.

A similar result has been obtained by Ollar and Viricel-Honorez,[158] as shown in Figure 53(b). Here, the pH is taken at 320°C and is determined using MULTEQ from an expression for the hideout return molar ratio. As with Figure 53(a), the pH tends to be in the mid-range and slightly alkaline.

pH as inferred from hideout return was also investigated by Sawochka, et al.[144] They found it was not possible to obtain good correlations between pH and either molar ratio or Na/Cl ratios. This result is consistent with the broad range of pH shown in Figures 53(a) and (b), although the latter exhibit trends that show that crevice pH is generally in the mid-range of pH and is not predominantly alkaline.

The crevice pH depends significantly on the relative concentrations of Si, Na, and Al in the water according to You, et al.[159] When the Na is high relative to Si and Al, then the pH tends to be high. Relationships among these species and their effects on pH are shown in Figure 54.

4.5 Crevice Chemistry from Hideout Return

Figure 55, from the work of Ollar and Viricel-Honorez,[158] correlates the occurrence of IGA with chemistry determined from 76 hideout returns from 20 units. This figure has organized the data into categories of >50 IGA affected tubes, <50 IGA affected tubes, and no IGA affected tubes. Figure 56 correlates hideout return over time, more specifically from a single plant, Bugey-3.

IGA, as shown in Figure 55(a), is favored by the lack of some elements and the presence of others:

1. IGA is favored by the lack of species: SO_4, Ca, glycolates, Mg, Na, and Cl.
2. IGA is favored by the presence of species: acetates, PO_4, formates.

The onset of IGA in Figure 56 seems correlated as follows:

1. IGA onset seems favored by the decrease of Na, K, and Cl.
2. IGA onset seems favored by the increase of F.

However, the apparent correlation for a single plant in Figure 56, which is based on increases in IGA at the same time as hideout return quantities of species changed at a single unit, does not provide a reliable guide as to the importance of such changes. For example, as pointed out by Ollar and Viricel-Honorez,[158] comparing Bugey-3 to other EDF plants, it has had lower rates of IGA and lower rates of sodium return, leading to the opposite conclusion to that based on Bugey-3 alone.

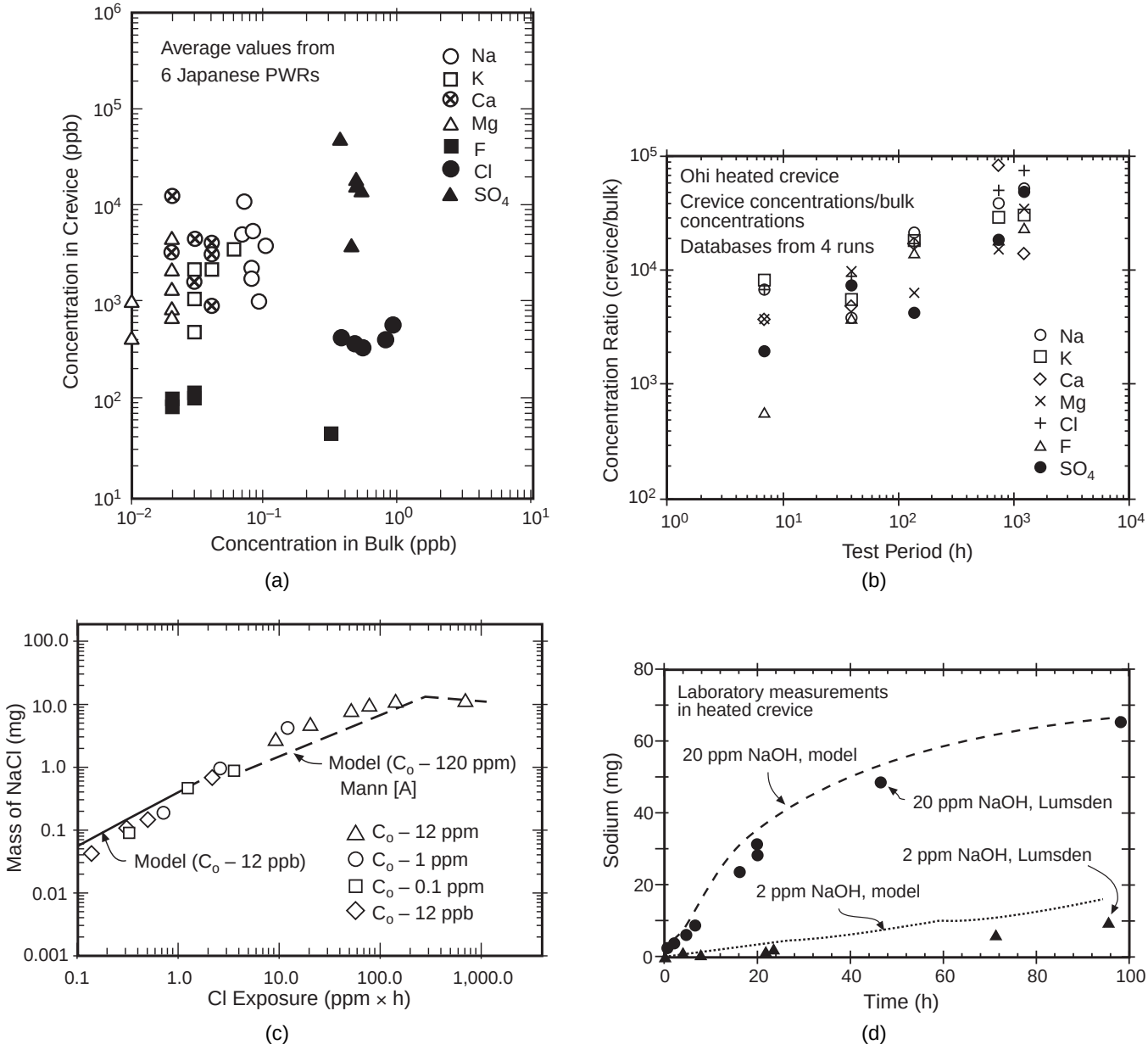

FIGURE 51. *(a) Concentration in crevice vs concentration in bulk for anions and cations taken from six Japanese PWRs. From Shoda, et al.[154] ©1996 NACE International. (b) Crevice concentration ratio vs test periods as measured in Ohi-1. From Lumsden, et al.[149] Courtesy of TMS, Warrendale, Pennsylvania. (c) Mass of NaCl vs ppm × hours of exposure to chloride-containing solutions. Data from [A] Mann, et al.,[155] and analysis from Millett and Fenton.[156] ©1992 by the American Nuclear Society, La Grange Park, Illinois. (d) Measurements in laboratory autoclave heated crevice. Weight of Na^+ in a crevice packed with diamond powder with 64% packing density at constant heat flux and 20 ppm Na^+ in the feedwater. From Lumsden, et al.[149] Courtesy of TMS, Warrendale, Pennsylvania.*

Explanations of these influences of various species are speculative. The meaning of the trends in hideout return is affected by the buildup of deposits with time and the change in species in deposits with time. Also, water chemistry has become generally cleaner with time. It seems the best that can be concluded is that correlations between hideout return and IGA show some interesting patterns, but the meaning of these patterns is obscure.

Figure 55(b) and Table 8 compare the hideout returns from drilled holes and broached holes. While the magnitudes are somewhat similar overall, there are some significant differences between hideout return from drilled and broached holes. In general, as shown in Figure 55(b), with the exception of silica (SiO_2) and PO_4, the hideout return is less for broached holes. The phosphate return is significantly higher for the broached TSPs, and the silica is some-

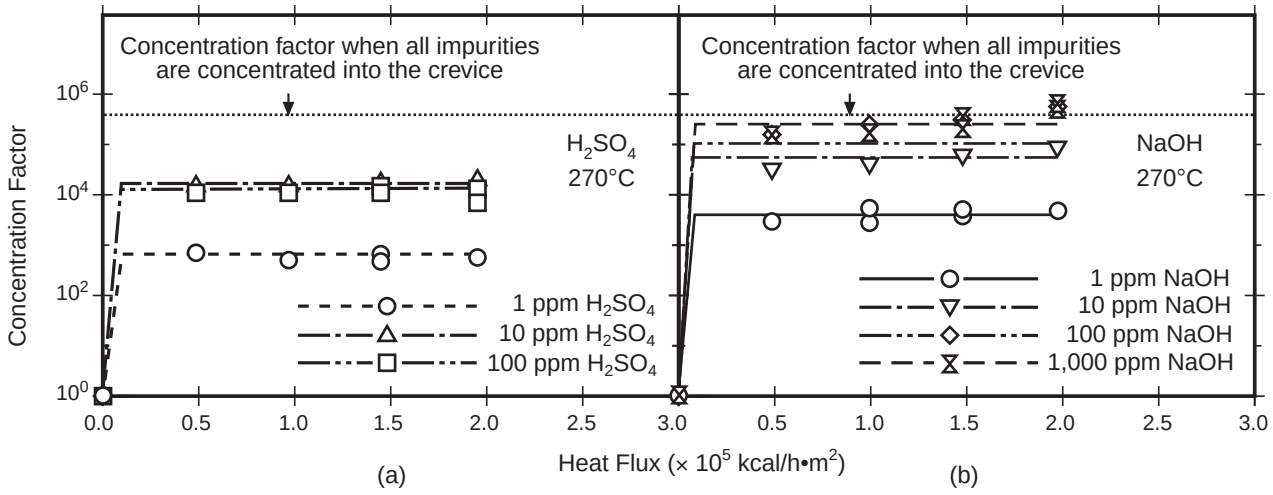

FIGURE 52. *(a) Concentration factor vs heat flux for four concentrations of H_2SO_4 in the bulk solution at 270°C. Concentrations based on monitoring the electrochemical potential. (b) Concentration factor vs heat flux for four concentrations of NaOH in the bulk solution at 270°C. Concentrations based on monitoring the electrochemical potential. From Kawamura and Hirano.[152]*

TABLE 7
pH_T in Crevice vs Heat Flux[(A)]

Heat Flux 10^5 kcal/h·m^2	pH_T	w/o Na
0.49	9.90	0.51
0.99	10.02	0.94
1.48	10.19	2.7
2.06	10.40	8.2

[(A)] Based on data from Kawamura and Hirano.[152]

what higher. On the other hand, the hideout returns for many species are significantly lower for the broached holes than for the drilled holes (e.g., Ca, SO_4, acetates, Na, K, C, and Cl). These differences are larger than the differences in Figure 55(a) for the presence and absence of IGA in drilled hole SGs.

Table 8 shows data for hideout return taken at different temperatures. At the right of this table, ratios of the coldest to hottest locations are calculated. These data are distinguished by the high ratios for phosphate and sulfate. Such high ratios are due to the retrograde solubility of phosphate and sulfate compounds as discussed in connection with Figure 31; it appears also that calcium and magnesium participate in these retrograde compounds.

In Table 9 the ratios of hideout returns for broached holes to drilled holes based on mean values of returned weights are tabulated for data from both Figure 55(b) and Table 8. The ratios from Table 8 are based on summing the hideout return from the three columns that are based on different temperatures. Values at 0.5 or less include the following species: acetates, Ca, Cl, Na, SO_4. Only PO_4 and SiO_2 are greater than unity, and this results from their retrograde solubility at an elevated temperature. There is good agreement between data from the same species.

Baum, et al.,[160] and Prabhu[161] have analyzed steam generator blowdown chemistry relative to correlations with outside diameter stress corrosion cracking (ODSCC). They find that low SiO_2 correlates positively with high incidences of ODSCC, as shown in Figure 57. They find that other correlations with cation/anion, Na^+, Na/Cl, and molar ratios provide poor correlations. Unfortunately, Figure 55(a) does not contain analyses for SiO_2. Baum and Prabhu conclude that the SiO_2 is an inhibitor and that low concentrations in the blowdown indicate a loss of inhibition by SiO_2. The work of Navas, et al., in Figure 57(b)[162] shows that silica in two forms inhibits alkaline stress corrosion cracking (AkSCC) over a range of potentials, thereby confirming the speculation of Baum, et al.[160] The work of Bergen in Figures 57(c) and (d)[163] shows that AkSCC of Alloy 600 and Alloy 690 is inhibited by certain ranges of sodium monoxide (Na_2O) and SiO_2 but accelerated in others. Such a result is consistent both with the work of Sala and coworkers[164-166] and Baum, et al.[160] Implications for AkSCC are discussed in Section 5.2.1.

Hideout return has been investigated by Balakrishnan[167] where he found the anionic species are released more slowly than cationic ones when oxidizing conditions are present. This effect seems to result from a counterforce of the potential gradient in crevices. These results indicate that data from hideout return should allow for such delays, although the specific implications of his work for the studies described in this section are not clear.

4.6 Deposits (Recirculating Steam Generator, Once-Through Steam Generator)

Deposits that form in heat-transfer crevices and other locations contain chemicals that provide clues to the surrounding aqueous phases. Chemical infor-

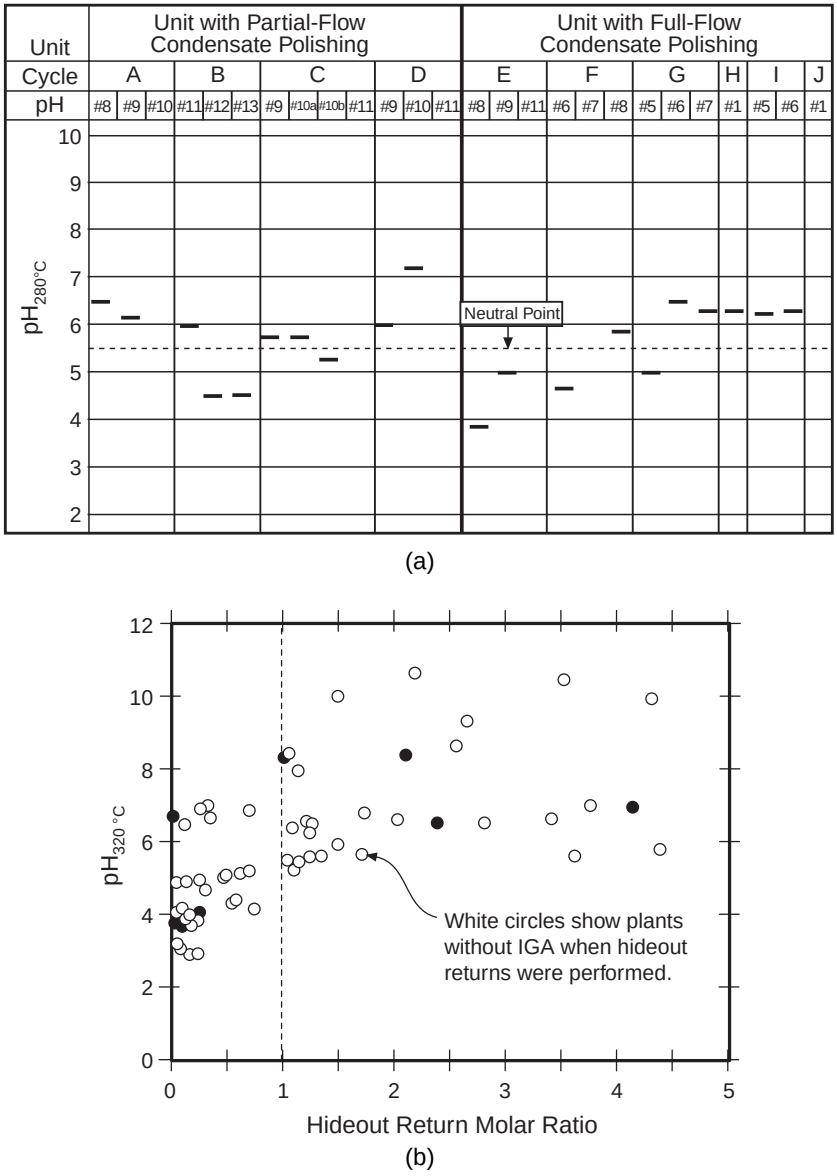

FIGURE 53. *(a) pH at 280°C vs cycle for nine Japanese plants. (PFCP = partial-flow condensate polishing [or polishers]; FFCP = full-flow condensate polishing [or polishers]). From Shoda, et al.[154] ©1996 NACE International. (b) pH at 320°C vs hideout return molar ratio. Open symbols show plants without IGA when hideout returns were performed. pH determined with MULTEQ. From Ollar and Viricel-Honorez.[158] Courtesy EDF.*

mation from deposits can be compared with that from hideout return from plants and from laboratory tests of heated crevices. Synthesizing these sets of information should provide a good view of the chemistry in heat-transfer crevices in operating steam generators.

Deposits of interest are the following:

1. Top of the tubesheet crevice.
2. Sludge at the top of the tubesheet.
3. Sludge crevice.
4. Free surfaces including boiling and non-boiling.
5. Free surfaces adjacent to tube support crevices.
6. Tube support crevices.
7. Upper bundle of OTSGs.

An overall view of the locations and types of deposits in SGs is given in Figure 58.

Obtaining chemical information from these crevice locations is often difficult because they must be removed from active steam generators during shutdowns when there are great pressures to avoid delays. Further, the materials and pieces to be removed have to be removed from tight surroundings, and some of the materials are radioactive from the primary side. Finally, much of the deposits may be scraped from tubes as they are pulled from steam generators.

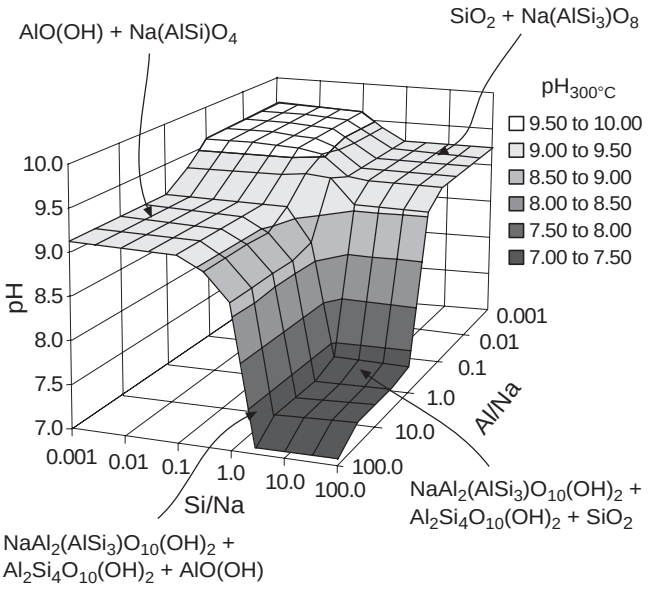

FIGURE 54. *pH vs Si/Na and Al/Na ratios for a liquid crevice as calculated from MULTEQ for 300°C. From You, et al.*[159]

Information from the chemistry of deposits is available as follows:

1. Morphology and Compositions of Deposits — Figures 59 through 66 show the results of detailed analyses of surfaces of tubes from plants that have been exposed to different conditions as identified in Table 10. Important observations from these surface analyses are the following:

a. Alumino-silicates: Sala and coworkers[164-166] observed that the occurrence of SCC is related to the formation of alumino-silicate compounds and this correlation is shown in Table 10. Little or no SCC occurs where the alumino-silicates are absent as for seaside plants. This occurrence of alumino-silicates would be expected for pH in a range on the order of 8 or lower at temperature and would not occur in the range where alkaline SCC would be expected.
   The detailed processes by which alumino-silicates produce SCC are not clear. For example, as shown in Figure 57(b), silicates can function as inhibitors in alkaline solutions.
b. Layers: There seem to be generally three layers in deposits inside heat-transfer crevices. The inside layer seems to contain metallic species or their oxides such as Cu, Zn, Pb, As, Sb, Ba, and alloying elements. The second layer in some cases is composed of silica gels. The outside layers tend to contain various compounds of Fe, Ni, Si, Ca, Mg, Al, and Mn that seem to have crystallized from solutions during shutdown.
c. Inside crevice vs outside on free surface: In Figures 59 through 66, the chemistry and morphology of the surface are shown for adjacent regions inside and outside the crevice. There are some similarities in the regions. However, generally, the alumino-silicate compounds seem to occur more inside the crevices, and there are fewer, if any, alumino-silicates associated with the tubes where IGA is not occurring, except for Figure 66 and Line 8 of Table 10 where the alumino-silicates are extensive and no IGA occurs.
d. Copper vs titanium: In Figures 63 and 64, where the plants use titanium condensers, little or no copper is observed. In the figures corresponding to the use of copper condensers, copper is observed.
e. Organics: Various organic species are observed and occur mostly inside the crevices but sometimes outside.

2. Analyses of Deposits from Surfaces — Chemistries of surfaces have been analyzed directly to compare the chemistry with the occurrence of failure and to discern differences between the heated crevices and the free-span.

Table 11 shows average results from Boursier, et al.,[172] taken from four locations of corrosion damage. These results are generally consistent with those in Figures 59 through 66 in that aluminum and silicon are observed as well as PO_4, Zn, Cu, and Mn. Pb and As are both observed in significant quantities.

While the layers in the deposits of Figures 59 through 66 are somewhat miscellaneous, there is nonetheless some order according to Cattant, et al.[171] Figure 59 shows three layers with respect to the region inside the heated crevice designated at the right with L_I at the outside, L_{II} next, and L_{III} adjacent to the metal. He characterizes these layers, with respect to Figure 59, as follows:

L_I (outside)

This layer is the thickest of the deposit, about 25 μm to 30 μm, and consists primarily of recently precipitated silicates sealed by calcium phosphate ($Ca_3[PO_4]_2$) and probably by calcium sulfate ($CaSO_4$) or barium sulfate ($BaSO_4$). Carbon-containing compounds were occasionally identified. Zinc was deposited on the silicates as zinc oxide (ZnO). Copper was present in the cupric oxide (CuO) or Cu^+ valence. When magnetite was present, copper deposited on it preferentially, and the ZnO deposited on the silicates.

L_{II} (middle)

Silicates were deposited on an alumino-silicate alveolar gel. Closer to the matrix the gel becomes enriched in Fe, Ni, and Cr. The gel is highly hydrolyzed and combines somewhat with oxidized organic compounds.

L_{III} (inside)

Under the silica gel layer there was a thin layer about 0.5 μm thick enriched in Cr, Fe, Cu, Zn, carbon compounds, and Pb. This layer was amorphous

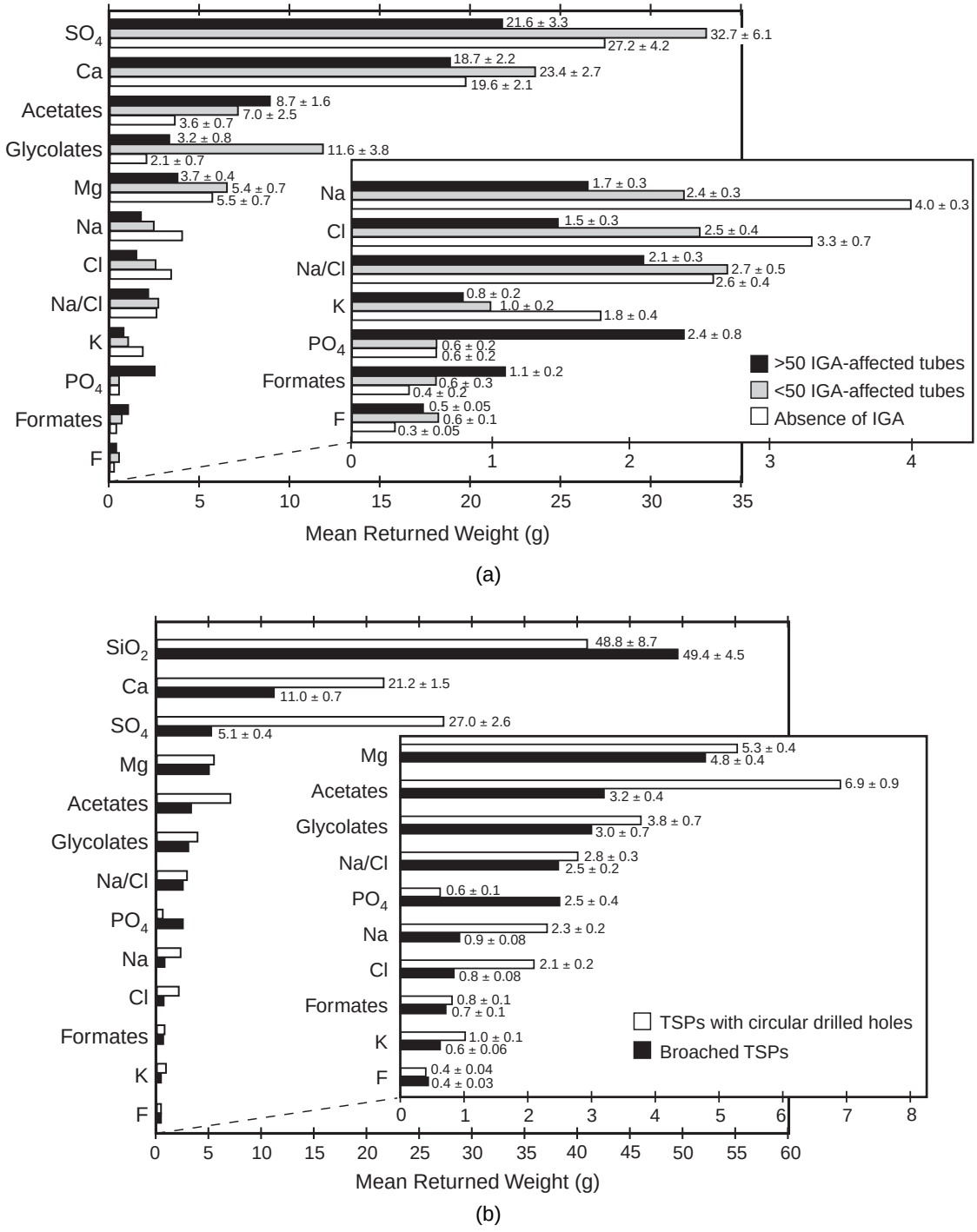

FIGURE 55. *(a) Species analyzed vs mean weight per steam generator equipped with drilled holes. Hideout return analysis compared with extent of damage to tubes. Data from 76 hideout returns from 20 units. From Ollar and Viricel-Honorez.[158] (b) Species analyzed vs mean weight per steam generator equipped with either circular drilled holes or broached holes. Data from 150 hideout returns from 20 units. From Ollar and Viricel-Honorez.[158] Courtesy EDF.*

and brittle. IGA, when it occurred, was observed under this layer.

Table 12, from work by Goffin, et al.,[173] was developed from measurements of hideout return and chemical analyses of deposits on tubing from seven Belgian power stations and subsequent analyses with MULTEQ. The species observed in hideout return are similar to those in Figures 55 and 56. The analyses of deposits indicate also about the same species that are present in Figures 59 through 66. This table notes that there are certain species that were not foreseen in MULTEQ.

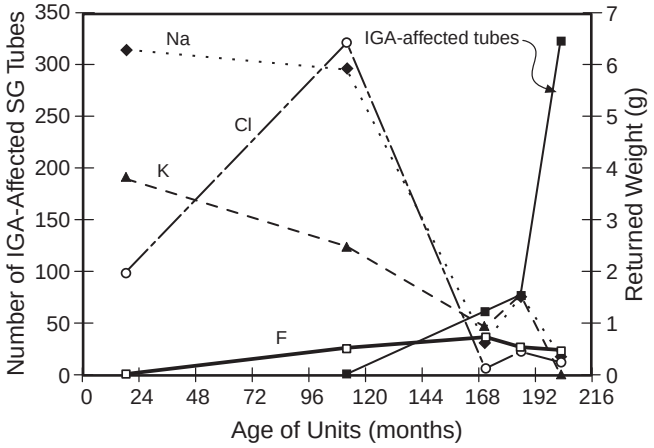

FIGURE 56. *Number of IGA-affected SG tubes and returned weights vs age from Bugey-3. From Ollar and Viricel-Honorez.[158] Courtesy EDF.*

Figure 67 shows results from elemental analyses (expressed mostly as oxides) of surfaces of about 340 pulled tubes from the work of Cattant, et al.[171] Here, a ratio is plotted for species in the restricted flow area, i.e., the heated crevice, to the concentration in the nonrestricted flow area immediately adjacent to the occluded region. These results show the following important patterns:

1. Ca, alumina (Al_2O_3), SiO_2, and Mg exhibit the highest ratios and are consistent with the observations in Figures 59 through 66. These high ratios of SiO_2 may account for the low concentrations in the blowdown shown in Figure 57 that correlate with failures, i.e., if the SiO_2 concentrates in the crevices, it does not appear in the blowdown.
2. Both Pb and As are concentrated in the heat-transfer crevices. While the former is expected, the latter has not been investigated for its effect on SCC except for a brief study by Pement, et al.[174]
3. The precipitation of stannic oxide (SnO_2) and molybdenum trioxide (MoO_3) indicate that the environment is in the neutral range.
4. For copper and titanium dioxide (TiO_2) there is little difference between the two locations.

A study similar to that by Cattant, et al.,[171] was conducted by Laire, et al.,[175] and is shown in Figure 68. The results for Ca, Al, and Si are similar to those in Figure 67. The ratio for copper is also similar. However, Pb was found about equally on both free-span and TSP surfaces; whereas, Cattant, in Figure 67, observed a ratio favoring the TSP surface of about 3.1 to 1.0.

3. Analyses through the Thickness — Figure 69 from Cattant, et al.,[171] shows the elemental composition through the third layers of both the occluded and free-span regions from Figure 59 and Line 1 of Table 10. Here, the most important difference seems to be with the Si, which is greatly enriched in the occluded region relative to the free-span. This result is consistent with the results in Figure 67. Chromium also is somewhat enriched in the deposit suggesting that the region is acidic. Iron, clearly, is enriched on the free-span relative to the occluded region and the

TABLE 8

Species vs Mean Returned Weights for Broached Holes and Drilled Holes at End of Hideout Returns for Three Thermal Conditions[A]

	TSPs with Circular-Drilled Holes			Broached TSPs			TSPs with Drilled Holes	Broached TSPs
Species	HSD[B] ~286°C	RHRS[C] ~170°C	CSD[D] <170°C	HSD[B] ~286°C	RHRS[C] ~170°C	CSD[D] <170°C	CSD/HSD, <170°C/ ~286°C	CSD/HSD, <170°C/ ~286°C
Na	1.9 ± 0.5[E]	1.9 ± 0.5[E]	3.7 ± 2.2[E]	1.2 ± 0.4[E]	0.7 ± 0.1[E]	0.8 ± 0.5[E]	1.9	0.7
K	0.7 ± 0.2	1.0 ± 0.1	1.0 ± 0.2	0.8 ± 0.2[E]	0.4 ± 0.05[E]	0.5 ± 0.2[E]	1.4	0.6
Cl	2.2 ± 0.5	2.2 ± 0.3	1.9 ± 0.4	0.7 ± 0.2	0.7 ± 0.09	0.9 ± 0.2	0.9	1.3
Na/Cl	5.0 ± 1.8[E]	4.3 ± 0.8[E]	4.2 ± 2.3[E]	3.3 ± 1.1[E]	2.3 ± 0.3[E]	6.7 ± 5.0[E]	0.8	2.0
F	0.5 ± 0.09	0.4 ± 0.05	0.5 ± 0.1	0.4 ± 0.07	0.4 ± 0.04	0.5 ± 0.2	1.0	1.3
Ca	9.0 ± 1.1	20.0 ± 1.8	26.4 ± 2.4	8.5 ± 1.6	11.7 ± 0.8	11.8 ± 2.5	2.9	1.4
Mg	2.2 ± 0.4	5.2 ± 0.4	7.7 ± 1.0	3.8 ± 0.8	4.9 ± 0.4	8.8 ± 2.4	3.5	2.3
SO_4	6.7 ± 1.1	25.7 ± 3.3	41.7 ± 5.6	3.5 ± 0.7	5.4 ± 0.5	12.8 ± 4.4	6.2	3.7
PO_4	0.1 ± 0.04	0.6 ± 0.2	4.1 ± 1.2	0.6 ± 0.2	3.3 ± 0.6	14.3 ± 5.5	41.0	23.8
Acetate	13.2 ± 6.5[E]	2.9 ± 0.5[E]	4.1 ± 1.9[E]	1.0 ± 0.3[E]	3.6 ± 0.7[E]	1.4 ± 1.0[E]	0.3	1.4
Formate	0.7 ± 0.3[E]	0.4 ± 0.2[E]	0.3 ± 0.1[E]	0.4 ± 0.1	0.8 ± 0.1	1.0 ± 0.6	0.4	2.5
Glycolate	11.4 ± 4.0	2.8 ± 0.6	5.0 ± 2.2	—	—	—	0.4	—

[A] From Ollar and Viricel-Honorez.[158] CSD/HSD ratios calculated by present authors.
[B] HSD = hot shut down (about 286°C).
[C] RHRS = residual heat removal system conditions (about 170°C).
[D] CSD = temperature <170°C (taken here as cold shut down).
[E] Results obtained from populations in which unusual contaminants were removed.

results suggest that iron deposits form preferentially on the free-span surface. Interpreting these results is speculative. The actual situation might be that other species, being more dilute than iron in the feedwater, do not precipitate readily in free-span deposits since the concentration factor is too low, about 1,000X. In crevices, where the concentration factor can reach a million or more, they deposit.

4. Sulfide Deposits — Deposits of sulfides and the occurrence of sulfides in deposits in heated crevices is a special case, but an important one, since the sulfides are so important in producing SCC, including SCC of Alloy 690 as discussed in Section 5.2.6. Figure 33 shows the oxidation/reduction half cells including those for N_2/N_2H_4 and SO_4^{2-}/S^{2-}. The positions of these half-cell equilibria show that N_2H_4 should reduce SO_4^{2-} to S^{2-}. Thus, in operating steam generators, SO_4^{2-} impurities should be chemically reduced, especially by the relatively large concentrations of N_2H_4. If N_2H_4 were not present, the very low hydrogen concentration in the secondary side would not reduce the sulfates according to Figure 33.

Daret, et al.,[176] have demonstrated that the presence of sulfide is directly related to the occurrence of SCC in Alloy 600 in a model boiler experiment, as shown in Figure 70; here, the SCC occurs where the sulfide is maximum. Further, another lower valence sulfur oxyanion, thiosulfate ($S_2O_3^{2-}$), produced extensive SCC in sensitized Alloy 600 in TMI-1 when a tank of sodium thiosulfate ($Na_2S_2O_3$) was accidentally connected to the primary system.[177-178]

The reduction of SO_4^{2-} to S^{2-} by N_2H_4 also has been confirmed by Sakai, et al.,[179] Sala, et al.,[180] and Allmon, et al.[181]

5. Deposits in the Upper Bundle of OTSGs — While much of this discussion deals with heat-transfer crevices of the type shown in Figures 2, 4, 10, and 21, Figure 8(b) notes that a superheated surface also exhibits the capacity to concentrate impurities similar to the heat-transfer crevice geometry. Such a surface occurs in the upper bundle of OTSGs, and Figure 25 shows the rate of failure of tubing in this region. SCC in the upper bundle of OTSGs, shown in Figure 1(b), is mostly associated with scratches introduced during fabrication. Aside from this SCC related to scratches, most damage to OTSGs is described in Table 5. While the OTSGs have generally exhibited good performance, as described by Sherburne,[182] and have not sustained significant corrosion at tube supports or tubesheets, the SCC in the upper bundle seems unique to the OTSGs in spite of the generally good water chemistry, the compressive stresses applied to the tubes during operation, and the sensitized metallurgy that generally mitigates both LPSCC and AkSCC.

The chemistry of outer secondary surfaces and the inside of SCC and IGC surfaces on tubing in the upper bundle of Oconee OTSGs have been investigated by Rochester, et al.,[183] Rochester and Eaker,[184] and Rochester.[185] Chemical analyses shown in Figure 71 from Rochester on the outside surfaces near the scratches and near the SCC from an OTSG show that there are four distinguishable regions, including the mouth of the SCC and its tip:

TABLE 9
Ratios of Returned Weight from Broached Holes vs Drilled Holes[A]

	Figure 55(b)[B]	Table 8[C]
Acetates	0.5	0.3
Ca	0.5	0.6
Cl	0.4	0.4
F	1.0	0.9
Formates	0.9	1.6
Glycolates	0.8	—
Mg	0.9	1.2
PO_4	4.2	3.8
K	0.6	0.6
SiO_2	1.2	—
Na	0.4	0.4
Na/Cl	0.9	0.9
SO_4	0.2	0.3

[A] From Ollar and Viricel-Honorez.[158] Courtesy EDF.
[B] Ratios based on mean values.
[C] Ratios taken from sums of HSD+RHRS+CSD for broached and drilled holes.

Typical OD Surface

On the outer surface the chemical species are similar to those that are observed in heat-transfer crevices of RSGs, as shown in Figures 59 through 68. In Figure 71, these species include Mg, Si, Al, Ca, K, SO_4, Zn, Cu, Ni, and Na. Beneath this outer layer is a Cr-rich oxide, which may have been formed during the post-weld heat treatment that was given to the vessel during fabrication. Below the Cr-rich oxide is a Cr-depleted layer suggesting either that this region exists at a relatively high potential due to the formation of soluble +6 valence resulting from very low H_2 as shown in Figure 33, or that it is somewhat alkaline, or that Cr was enriched in the aluminosilicate deposit as observed in RSG crevices by Cattant, et al.[171]

Typical Scratch Surface

Most of the aspects typical of the OD surface are similar to the surface of the scratch, suggesting that both surfaces were exposed to the same environment and that the scratch was present at the beginning of the operation. Again, these species and their extent are similar to those on surfaces of tubes in the heat-transfer crevices of RSGs.

Crack Mouth

Some of the same species are present at the crack mouth as on the exterior surfaces. What appears to be fewer species and lesser amounts is due to both the geometry and later development of the crack. Also, generally, there has not been sufficient time for depletion of Cr as shown in Figure 71. How-

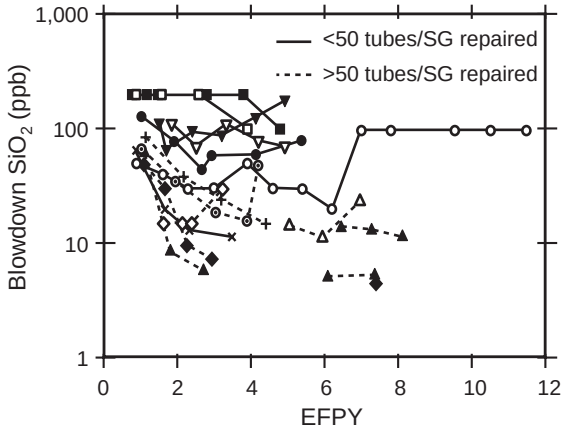

(a)

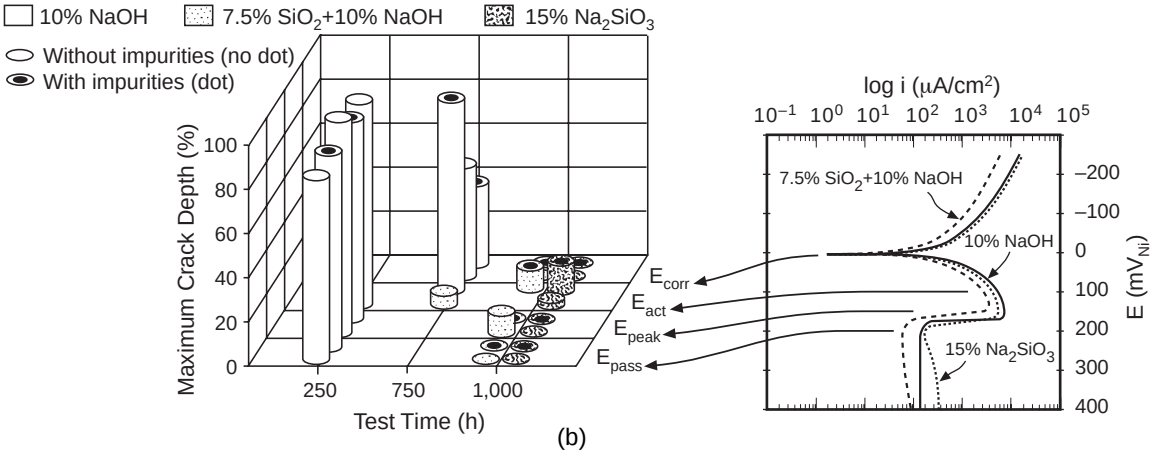

(b)

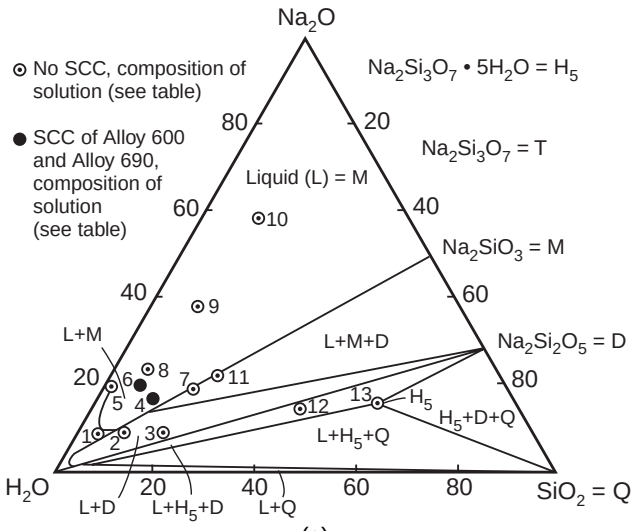

(c)

Composition of Test Solutions, mol%. Test Results from Alloy 600 and 690 at 325°C in H_2O + Na_2O + SiO_2 Solutions

Soln. No.	Na_2O	SiO_2[2]	Alloy 600			Alloy 690[1]	
			Test duration (h)	U-bends (cracked/ total)	Deepest crack (mm)	Test duration (h)	U-bends, (cracked/ total)
1	8.2	4.5M	175	(0/6)	—	—	—
2	8.2	9M	175	(0/6)	—	—	—
3	8.2	17[3]M	175	(0/6)	—	—	—
4	16	12M	175	(2/6)	1.3	175	(6/6)
			343	(3/6)	2.1	—	—
5	19	2M	343	(0/6)	—	—	—
6	19	7M	175	(1/6)	0.05	175	(6/6)
7	19	17[3]M	175	(0/6)	—	—	—
8	23	7M	343	(0/6)	—	—	—
9	37	10M	175	(0/6)	—	—	—
10	58	12.5M	175	(0/6)	—	—	—
11	22	16M+6D	175	(0/6)	—	—	—
12	14	42T	175	(0/6)	—	—	—
13	19	55T	175	(0/6)	—	—	—

(1) Alloy 690 as received. Exhibited SCC.
(2) M = monomer, D = dimer, T = timer.
(3) This solution was made up as monomeric Na_2SiO_3 but is in a regime where some dimer should be present.

(d)

FIGURE 57. *(a) Blowdown SiO_2 vs EFPY for 16 plants affected by ODSCC showing tubes with high and low incidence of ODSCC. From Baum, et al.[160] ©1997 by the American Nuclear Society, La Grange Park, Illinois. (b) Maximum crack depth vs time for environments of 10% NaOH, 7.5% SiO_2+10% NaOH, or 15% Na_2SiO_3 at 315°C, each environment with and without additional impurities of 0.8 g/L Cl^-, 0.3 g/L Mg^{2+}, 14 g/L SO_4^{2-}, and 5.8 g/L Ca^{2+} (added as $MgCl_2$ and $CaSO_4$). Measurements taken at four potentials and over time. From Navas, et al.[162] Courtesy of Gomez-Briceno, CIEMAT, Spain. (c) Combinations of H_2O+Na_2O+SiO_2 in mol% tested for 175 h plus 343 h at 325°C using U-bends of as-received sheet. Phase diagram taken at 300°C.[168] Q = SiO_2, M = monomer (Na_2SiO_3), D = dimer ($Na_2Si_2O_5$), T = trimer ($Na_2Si_3O_7$), L = liquid, H_5 = $Na_2Si_3O_7 \cdot 5H_2O$. Open circles show tests with no SCC; closed circles show tests for Alloy 600 and Alloy 690 that sustain SCC. From Bergen.[163] ©1985 NACE International. (d) Results from testing Alloys 600 and 690 in combinations of H_2O+Na_2O+SiO_2 at 325°C. From Bergen.[163] ©1985 NACE International.*

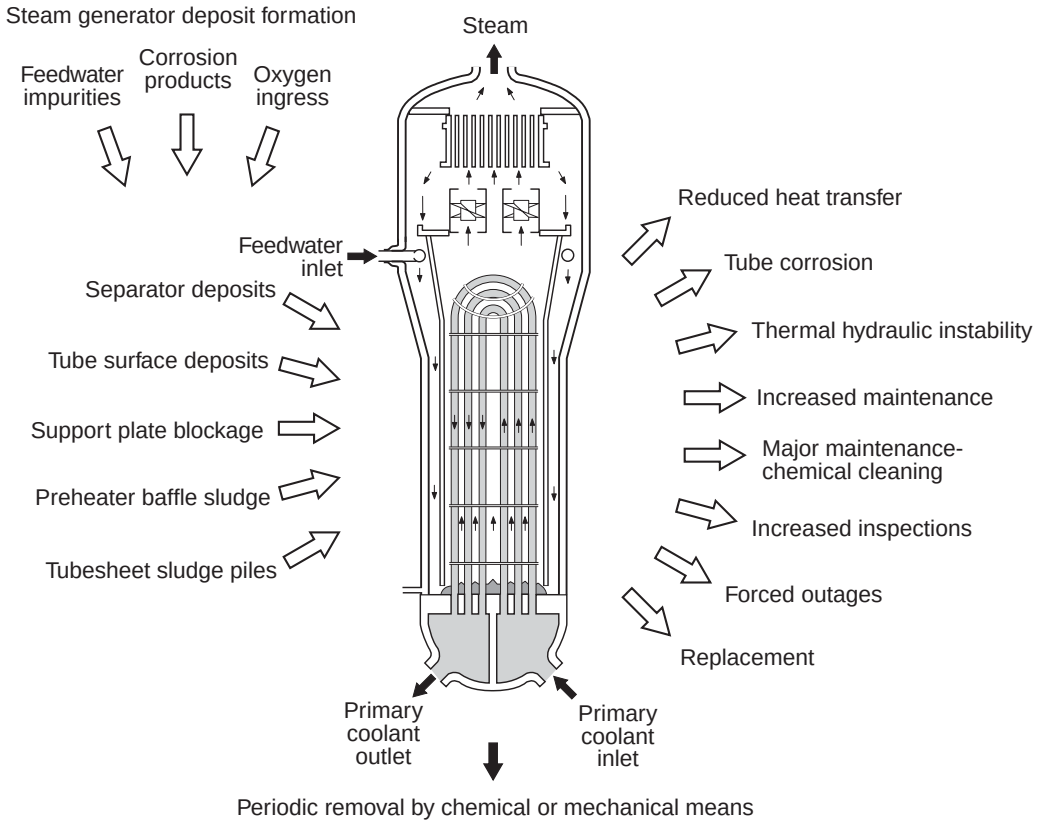

FIGURE 58. *Schematic view of locations where deposits form in steam generators and their implications. From Varrin.[169] Used by permission of EPRI.*

ever, a series of measurements of internal surfaces of SCC as a function of height inside an OTSG show possible evidence of depletion of chromium in some cases as indicated by the Ni/Cr ratio in Table 13 compared with the ratio at the ductile fracture surface. This table also notes the presence of sulfides inside cracks, which suggests a reducing trend together with possible alkalinity. The alkalinity, or reaction without alumino-silicates, would account for the depletion of chromium. The presence of sulfides inside the cracks is reasonable in view of the low potentials near the NiO/Ni equilibrium as suggested in Figure 41.

Crack Tip

The dominant presence of SO_4^{2-} and Cl^- at the crack tip suggests that this region may be somewhat acidic, which would be consistent with an oxidizing condition on the outside surface due to the low H_2. However, OTSGs operate with N_2H_4 so that such an oxidizing condition is not credible. K and Si may relate to this acidity. Also, the lack of Cr depletion, similar to that found at the crack mouth, further suggests that this region may be acidic.

In addition to the chemistry shown in Figure 71 and Table 13, more detailed analyses with the advanced transmission electron microscope (ATEM) near tips of SCC have identified substantial concentrations of lead, indicating how perceptions can change with analytical resolutions. Table 14 shows the results of analyses at eight different locations on two specimens. The highest concentration of lead observed was 7.7% of the total species at a given location. This finding suggests that lead might be the main species that activates the SCC of the upper bundles in the Oconee OTSGs.[185] Also calculated for Table 14 were the Ni/Cr ratios similar to those in Table 13. In some cases Cr enrichment was observed and in other cases it was not. The meaning of this pattern is not clear except to note that 6 of the 8 specimens exhibited depletion of chromium from the matrix.

In addition to the SCC observed at scratches, IGC was observed on the surface away from the scratches and was found randomly over the surface as shown in Figure 72. An overall view of the cross section is shown in Figure 72(a). This pattern of SCC under the scratches with IGC in an adjacent, less-stressed region is similar to the occurrence of other SCC, where SCC and IGC occur together or where the first one occurs and then the other, as suggested for AkSCC in Figures 82(a) and 97.

Four generally distinct chemical layers are shown in Figure 72(a), and these are generally similar to those in the heated crevices of the RSGs shown

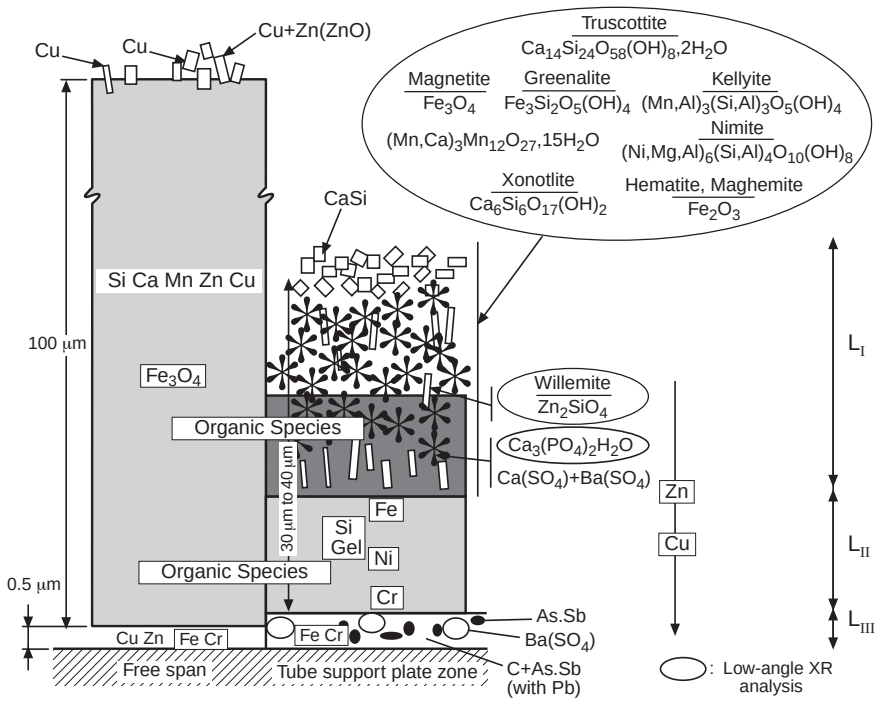

FIGURE 59. *From Line 1 of Table 10. Schematic view of OD tube surface from TSP 2 showing adjacent regions from inside the tube support plate and outside in the free-span. The condenser was brass, and morpholine was used for water conditioning. The tube was examined for 65,952 h. From Sala, et al.[164] Noted to be taken from St. Laurent B-1 from Cattant, et al.[171] ©1996 NACE International.*

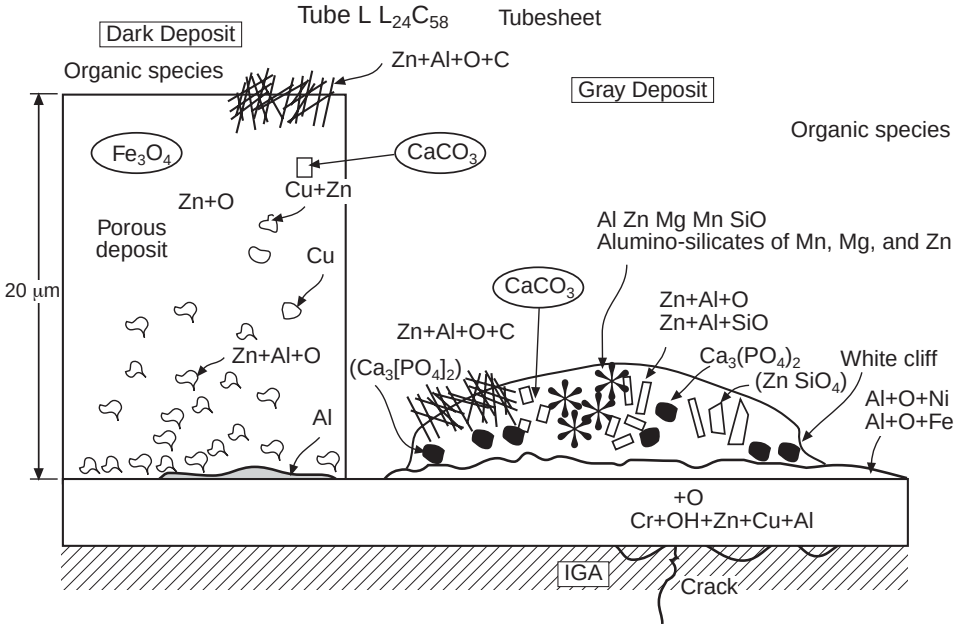

FIGURE 60. *From Line 2 of Table 10. Schematic view of OD tube surface from the top of the tubesheet. The condenser was brass and the water conditioning was morpholine. The tube was examined for 85,120 h. From Sala, et al.[166] Courtesy EDF/GDL.*

in Figures 59 through 66. Details of the chemistry are shown in Figure 72(b). The depths shown in the Auger analysis in Figure 72(b) are similar to those in Figure 71.

To clarify the environment in the upper bundle, Figure 73 shows relevant equilibria relating to the hydrogen electrode and the stability of chromium. Other relevant equilibria are shown in Figure 33. Fig-

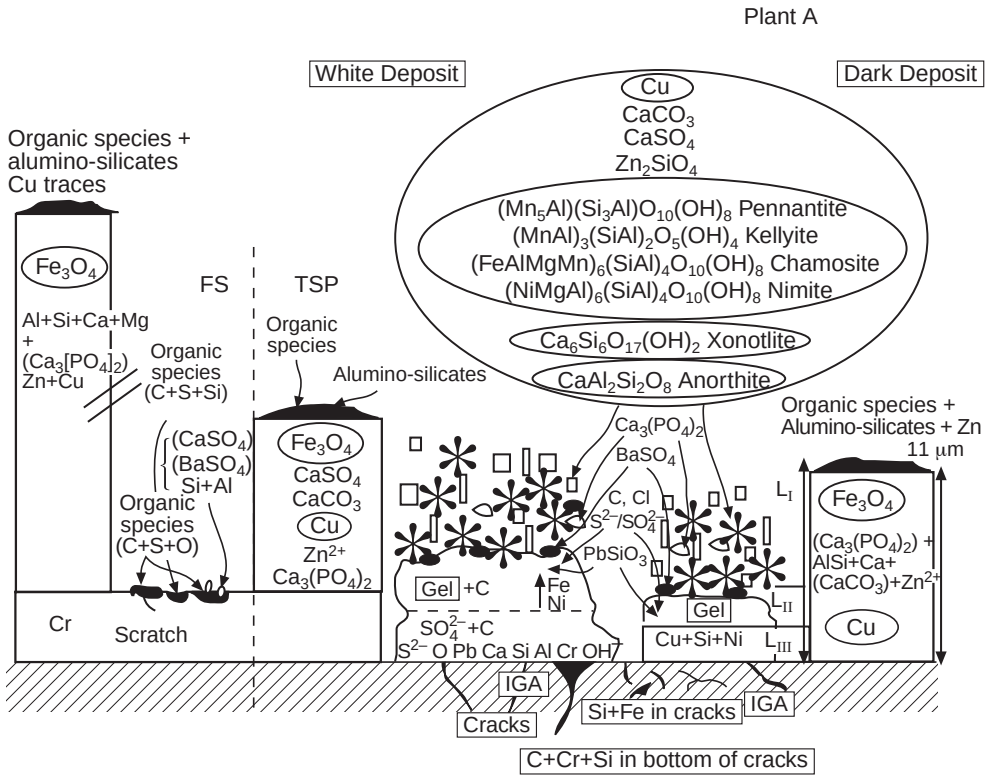

FIGURE 61. *From Line 3 of Table 10. Schematic view of OD tube surface from the TSP 2 showing adjacent regions from inside the TSP and outside on the free surface. The condenser was brass, the water treatment was 2.5 years on NH_3 and the remainder on morpholine. The tube was examined for 83,300 h. From Cattant, et al.[171] Courtesy of CEFRACOR (Centre Français de L'Anticorrosion), Paris, France.*

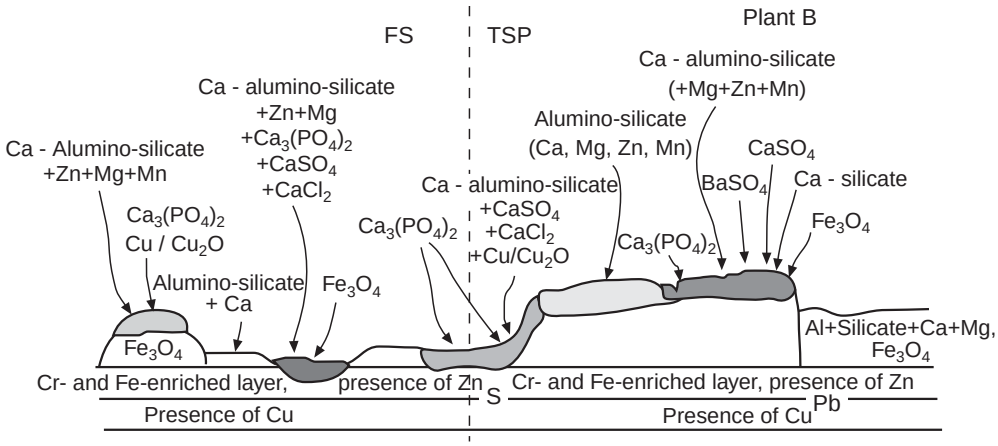

FIGURE 62. *From Line 4 of Table 10. Schematic view of OD tubesheet from a TSP showing adjacent regions from inside the TSP and outside on the free surface. The condenser was brass and the water chemistry was morpholine. From Cattant, et al.[171] Courtesy of CEFRACOR (Centre Français de L'Anticorrosion), Paris, France.*

ure 73 is concerned mainly with aqueous equilibria. While this is apparently inconsistent with the upper bundle being superheated, Figure 71 shows that certain aqueous species have been transported to the tips of advancing SCC, thereby indicating that aqueous phases occur in advancing SCC.

Figure 73 shows that the H_2O/H_2 equilibrium line intersects the CrO_4^{2-}/Cr_2O_3 line at about pH 8. This indicates that 1 ppb H_2 in the H_2O/H_2 equilibrium half cell permits water to oxidize Cr_2O_3 to CrO_4^{2-} above pH of about 8 at 300°C. This reaction is facilitated by the fact that the E-pH slope of the $CrO_4^{2-}/$

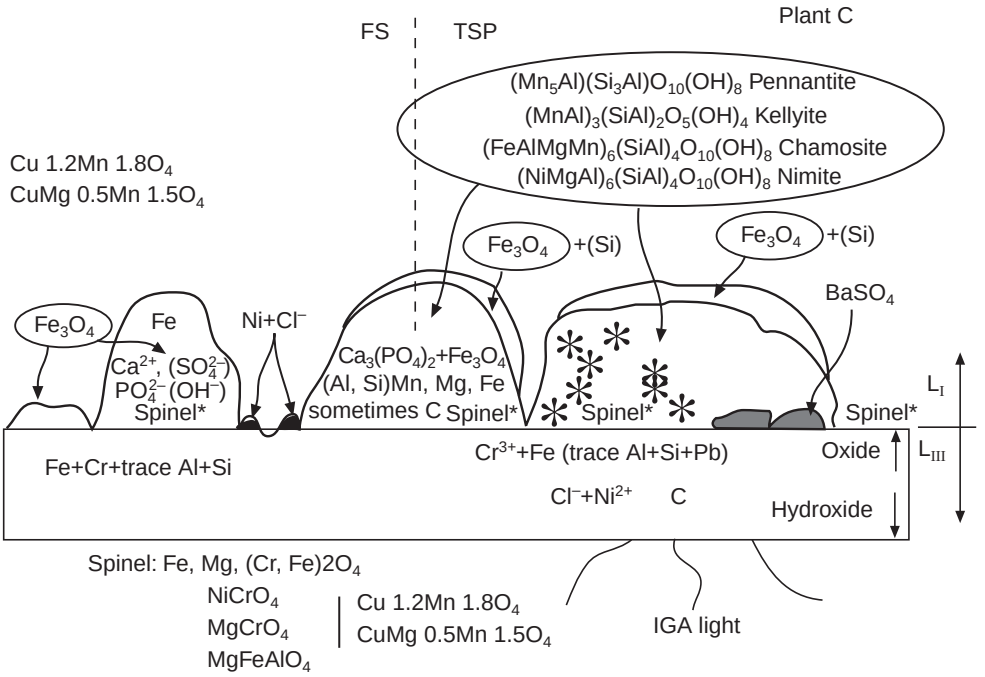

FIGURE 63. *From Line 5 of Table 10. Schematic view of OD tube surface from TSP 2 showing adjacent regions inside the TSP and outside on the free surface. The condenser was titanium and the water conditioning was NH_3. The tube was examined after 79,900 h. From Cattant, et al.[171] Courtesy of CEFRACOR (Centre Français de L'Anticorrosion), Paris, France.*

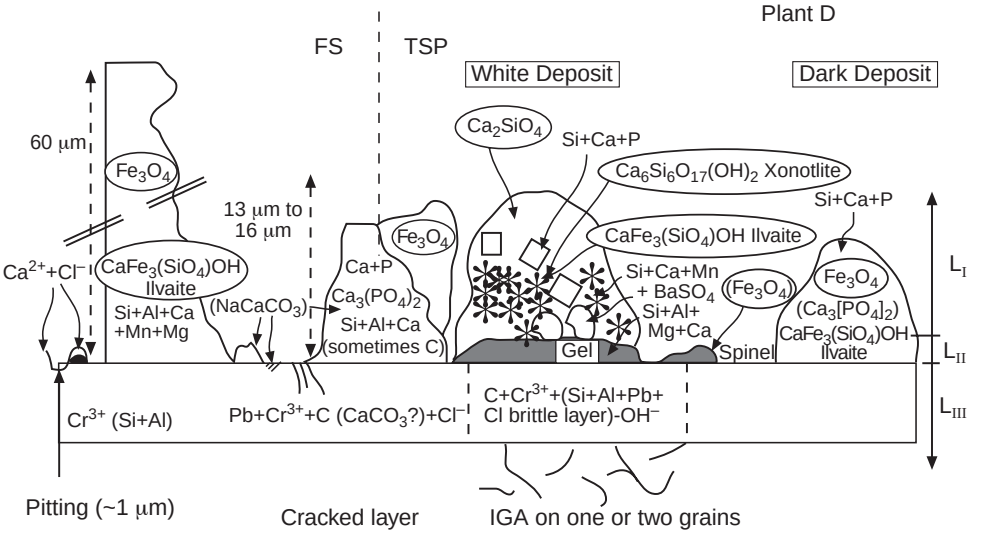

FIGURE 64. *From Line 6 of Table 10. Schematic view of OD tube surface from TSP 2 showing adjacent regions inside the TSP and outside on the free surface. The condenser was titanium and the water conditioning was NH_3. The tube was examined after 81,900 h. From Cattant, et al.[171] Courtesy of CEFRACOR (Centre Français de L'Anticorrosion), Paris, France.*

Cr_2O_3 half-cell equilibrium is twice the negative value of the H_2O/H_2 half-cell equilibrium. Figure 73 also shows the pH equilibria at the alkaline end noting that the 10^{-6} M solubility is at about pH 7. Cr_2O_3 can be solubilized by either alkalization or oxidation above pH 8; in fact, it is quite likely that the combining influences would be synergistic above pH 8. It is the ready solubility of Cr that leads to the Cr depletion noted in Tables 13 and 14 and in Figure 71.

4.7 Modeling Heat-Transfer Crevices

The objective of modeling the heat-transfer crevice is to provide a basis for predicting the local environment on the surface of the tubes and thereby to

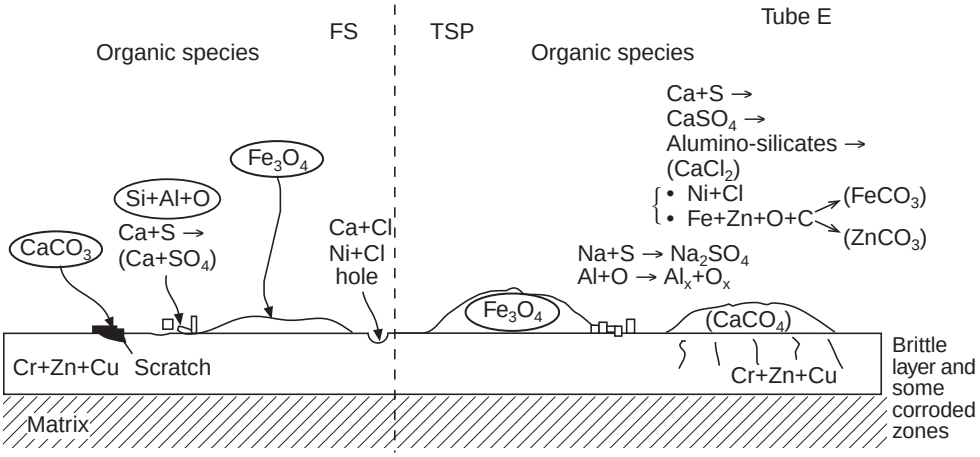

FIGURE 65. *From Line 7 of Table 10. Schematic view of OD of tube surface from TSP 1 showing adjacent regions inside the TSP and outside on the free surface. The condenser was brass and the water treatment was 3.5 years on NH_3 and 10 years on morpholine. From Sala, et al.[166] Courtesy EDF/GDL.*

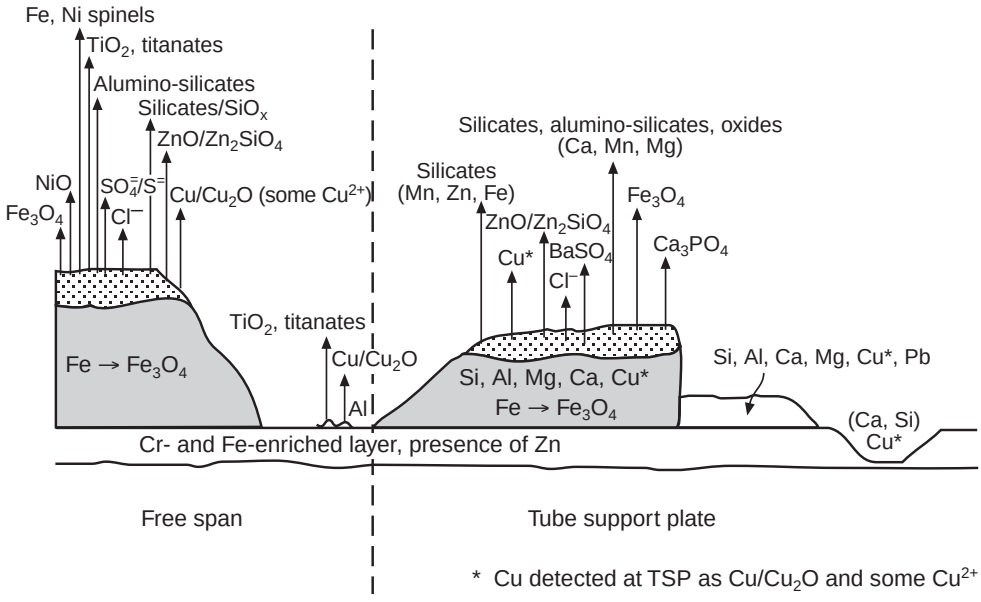

FIGURE 66. *From Line 8 of Table 10. Schematic view of OD of tube surface from TSP 1 showing adjacent regions inside the TSP and outside on the free surface. The tubes were exposed from time of commercial operation in 1981 until the SG was removed. The tubes were extracted in 1996. The tubes were subjected to additions of titanium as Degussa anatase TiO_2 at 1 ppb during 4 months of the last operating cycle. Blowdown concentration of TiO_2 was 5 ppb to 10 ppb. From Lancha, et al.[170] ©1997 by the American Nuclear Society, La Grange Park, Illinois.*

predict the occurrence of various modes of corrosion. Most importantly, modeling the heat-transfer crevice should predict the local chemistries and their distribution within the crevice.

Modeling a heat-transfer crevice is particularly challenging for the reasons shown in Figure 10. There are four essential reasons for this complexity:

- The accumulated chemistry varies greatly as the very dilute input changes and also changes variously as species precipitate and change identity as when SO_4^{2-} is reduced to S^{2-} by N_2H_4.
- The packing of the crevice varies in its density and properties.
- The two-phase nature of the water, including the steam/water interface, changes the distribution of chemicals and the nature of the environment on the surface of the tube.
- Within the crevice there are sharp gradients in temperature, phase of water, composition, pH, electrochemical potential as it is affected by pH, and fluid density.

A further challenge has to do with the specific kind of environment on the surfaces of tubes. For

TABLE 10

Characteristics of Tubes Used for Analysis of Deposits[A]

	Reference of the Tubes	TSP or Top of Tubesheet	Condenser Material	Water Conditioning	Operating Hours	Corrosion	Deposit Over the Cracks
1	L L	TSP2 TSP2	Brass Brass	Morpholine Morpholine	65,952 65,952	IGA + many cracks (300 μm)	Under alumino-silicate[B]
2	L	TTS	Brass	Morpholine	85,120	Shallow IGA few cracks (250 μm)	Under aluminate[B]
3	A	TSP2	Brass	2.5 years NH_3 + morpholine	83,300	Few small zones with IGA + cracks	Under alumino-silicate[B] migration of Cr with organic species in the Al-Si deposit[B]
4	B	—	Brass	Morpholine	—	IGA + small cracks (45 μm)	—
5	C	TSP2	Titanium	NH_3	79,900	No IGA, no crack	—
6	D	TSP2	Titanium	NH_3	81,900	Shallow IGA, no crack	Under alumino-silicate deposit
7	E	TSP1	Brass	3.5 years NH_3 10 years morpholine	90,567	No IGA, no crack	No deposit of alumino-silicate but magnetite and calcite
8	Lancha Ringhals-3	TSP1	Ferrous	—	1981-1994 (years)	No IGA	Extensive alumino-silicate

[A] Lines 1 through 7 from Sala, et al.[166] Courtesy of EDF/GDL. Line 8 from Lancha, et al.[170]
[B] Alumino-silicate deposit contains calcium phosphate, iron oxide, copper, and zinc (the two last elements for brass condenser).

example, most of the corrosion testing in support of understanding the secondary side has been conducted in single-phase liquid water except for the extensive work of Daret, et al., in model boilers.[176] However, the environment on the tube surfaces where corrosion occurs is some combination of water, water/steam interface, and steam as shown in Figure 10. Preferential SCC in steam phases is discussed in Section 5.2.7. Only in pure water has it been shown by many investigators, including Economy, et al.,[186] that the LPSCC of Alloy 600MA exhibits a continuous behavior vs 1/T from steam to water, as shown in Figure 74.

In more complex environments such as the doped steam experiments of Dehmlow,[187] SCC and intergranular corrosion (IGC) are greatly accelerated, as shown in Figure 75. The conditions of the Dehmlow experiments could be the kind of environments in the steam phase of a heated crevice. Doped steam SCC (DSSCC) is discussed in Section 5.2.7. Also, Miglin and Sarver[188] have shown that there are substantial differences between the behavior in liquid water and saturated steam in the same closed environment, as discussed in connection with Figures 136 and 137, depending on the chemistry of the water phase and on the alloy. For example, Alloy 690 sustains lead stress corrosion cracking (PbSCC) readily in both vapor and liquid phases when the aqueous phase is NaOH and Pb; whereas, the Alloy 600 samples were generally less prone to PbSCC in the vapor phase.

If modeling cannot predict the chemistry of heat-transfer crevices that produce corrosion and interact with the dependencies of the modes and submodes of corrosion, it is of little scientific or practical fundamental use, although it might provide some useful qualitative insights. Essentially, models should rationalize the chemistries of Figures 59 through 71, as well as Tables 11 through 14. In fact, such modeling and predictions are not practically achievable as can be seen by the comparison of conditions that produce high and low intensities of SCC/IGC in Figures 55, 56, and 57(a), as well as by the variation of SCC intensity summarized in Table 10 together with subsequent figures. Here, while the patterns are interesting, they are not always consistent.

TABLE 11

Mean Compositions of Deposits from Various Tubes Removed from Steam Generators for Different Locations and Damage Configurations[A]

Degradation	Species									
	Fe_3O_4	ZnO	Cu	MnO	Al_2O_3	PbO	Na	PO_4^{3-}	SiO_2	As_2O_3
Longitudinal cracking above the top-of-tubesheet in the sludge pile zone	35.61	6.50	9.21	2.82	8.54	0.72	0.29	3.82	12.06	0.15
Circumferential cracking under the top-of-tubesheet in the sludge pile zone	33.70	3.03	4.21	2.32	8.59	0.48	0.20	3.79	19.38	0.15
Circumferential cracking under the top-of-tubesheet out of the sludge pile zone	50.30	6.19	5.47	5.75	3.93	0.31	0.49	4.60	3.68	0.06
IGA/SCC at the tube support plate elevations	42.92	9.00	1.18	3.40	3.28	0.30	0.16	1.11	17.12	0.04

[A] From Boursier, et al.[172] Courtesy of TMS, Warrendale, PA.

Nonetheless, some useful modeling has been developed. Millett with his coworkers[189-193] developed and clarified both the relationship of wetted length to the available superheat as shown in Figure 76(a) and the relationship of concentration to crevice length as a function of time for 7 ppm NaOH as shown in Figure 76(b). Figure 76(a) shows that the wetted length, i.e., the part that is not steam, decreases with increasing superheat and with decreasing permeability. Figure 76(b) shows that the accumulation of chemical species increases as some function of time, which would also depend on permeability. A relatively high initial concentration was chosen here because the accumulation of impurities in a heat-transfer crevice is proportional to the product of concentration in the bulk environment and the time of exposure as shown in Figure 51(c).

In general, Millett and his coworkers developed a model that dealt with dimensions of the heated crevice, permeability of the deposits, concentration in the bulk environment, superheat, two-phase conditions, and time. This is a broad view of some of the main influences on the behavior of heat-transfer crevices.

Macdonald, Engelhardt, and coworkers[194-196] have added to the Millett work by introducing electrochemical and transport elements to the modeling. Their electrochemical elements include charge balance for the species, migration, and zero summation of anodic and cathodic reactions. Using their model shown in Figures 77(a) and (b) they obtain a distribution of species in a simple system as shown in Figure 77(c). Here, the region less than 0.5 cm corresponds to a convective region; the region greater than 0.5 cm corresponds to the concentration of species being independent of distance and represents the maximum concentrations achievable. These concentrations are similar in order of magnitude to those shown in Figures 51(c) and (d).

Contributions by Savchik and Burke,[197] Keefer and Keeton,[198] and Duncan, et al.,[199] have considered thermal hydraulic aspects of heat-transfer crevices. Keefer and Keeton have applied a computational fluid dynamics methodology to modeling heat-transfer crevices and have developed a damage parameter shown in Figure 78, which shows that the worst case involves the highest tube-metal temperatures and lowest heat fluxes. In this formulation the damage parameter equaled calculated concentration factor times the liquid collapse level, which is the equivalent height of the liquid volume fraction in the heat-transfer crevice. The damage parameter indicates, essentially, that the greatest damage occurs when the tube surface temperature is the highest. This increases reactivity and maximizes superheat, which also maximizes the concentration of dissolved species.

Duncan, et al.,[199] have applied computational fluid dynamics to calculating the size of the dry-out region of a tube support crevice geometry with a tube located asymmetrically inside a drilled hole using various assumptions about pressure drops, heat fluxes, and surface tension. For a cylindrical crevice 1-in. long with an average 0.015-in. diametrical gap and a 0.002-in. minimum gap, the table in Figure 79(c) gives the size of the dryout bubble as illustrated in Figure 79(a) for a 1.0-in. vertical crevice as a function of pressure drop, surface tension, pressure, and heat flux. Peak temperatures of the configuration in Figure 79(a) are shown in Figure 79(b) and indicate that cooling lowers the surface temperature; whereas, intimate juxtaposition of the tube to the TSP produces the highest temperature.

Fauchon[200] has refined the model of Englehardt, et al.,[195] and has built also on the model of Millett[189] to produce a more flexible model that accounts for the electrochemical and thermal-hydraulic aspects of

TABLE 12

Comparison of Deposits and MULTEQ Precipitates (Typical Results)[A]

Hide Out Return (Between ( ): Not Foreseen in MULTEQ)		MULTEQ			Analysis of Deposits (Underlined: Not Precipitated in MULTEQ Between ( ): Not Introduced in MULTEQ)		
Cations	**Anions**	**pH_T**		**Precipitates**	**Cations**	**Anions**	**Molecular Compounds**
Na	Si	5 to 7	Na_2SO_4	SiO_2, $Na_2Si_2O_5$	Na	Si	SiO_2, complex silicates of Fe, Ni, Al, Mg... e.g., $(Ni,Mg)_3Si_4O_{10}(OH)_2$
Mg	SO_4		$MgSO_4$	Mg_2SiO_4, $Mg_3Si_2O_5$ $Mg_4Si_6O_{15}$	Mg	SO_4	Sulfides, complex sulfates of Fe, Mg,... e.g., $Na_2Fe(SO_4)_2(OH),3H_2O$
Ca	Cl		$CaSO_4$	$CaSiO_3$, $CaMg(SiO_3)$, $MgCa(SiO_4)$	Ca	Cl	($CaCO_3$), $CaSO_4$, $CaSiO_3$ ($BaSO_4$)
Al			AlO(OH)	$Ca_2Mg_5Si_5O_{22}(OH)_2$	Al		
Fe				$FeSiO_3$, Fe_2SiO_4 $CaFeSi_2O_6$	Fe		Fe_3O_4, Fe_2O_3, FeO, $(Fe, Mg)_2SiO_4$
Ni			NiO	Complex aluminosilicates $(NaAl_2[AlSi_3]O_{10}[OH]_2)$	Ni	(PO_4)	
Cr			Cr_2O_3		Cr		Cr_2O_3
Cu			CuO		Cu		
	NO_3				(Pb)	NO_3	(Pb oxides, sulfates, carbonates)
	NO_2				(Zn)	CO_3	(Zn oxide, silicates)
	Acetate	4 to 5			(Ti)	CH_3COO	Carboxylates
	Formate						(Oxidized oils)
	(Propionate)				(Mn)	HCOO	Intermetallic compounds Ni-Cu,
	(Pyruvate)				(Mo)		(NiAs, Ni-Pb, Ni-Pb-S)
	(Valerianate)						Coordination compounds
	(Oxalate)						(M-O-C)

[A] From Goffin, et al.[173] Courtesy of Laborelec.

the deposit-filled crevice. Her model predicts the evolution of wetting of the steam region in the heat crevice and has provided more extensive analysis of electrochemical properties. However, it has not considered any of the issues associated with deposits, as shown in Figures 59 through 68.

The modeling of real, deposit-filled crevices, as exemplified by the data of Figures 59 through 68, has been most realistically considered by Baum[201-206] and is epitomized in Figure 80. Here, Baum recognizes the major issues that affect the essential processes in heat-transfer crevices. In particular, he recognizes the problem of gradients within heated crevices, as in Figure 10, and the importance of the transport from hot to cold surfaces together with the concentrations at liquid/steam interfaces. Such conditions are difficult to describe quantitatively.

The data from Figures 10, 55, 56, 59 through 68, and Tables 8, 11, and 12 show that the chemistries inside heat-transfer crevices are complex. Baum[201-206] indicates that this complexity is produced by the large thermal gradients with associated superheat effects on the water/steam interface and by the large variations in volatility of species. In addition, gradients occur in electrochemical potential and pH that affect solubilities and transport. Also, other processes such as retrograde solubility and volatilization affect the solubilities of sulfate and phosphate compounds. This array of components, gradients, and reactions is summarized in Figure 10.

While this discussion mainly concerns surfaces inside heat-transfer crevices, deposits also accumulate on free-spans. Free-spans adjacent to heat-transfer crevices and free-spans for OTSGs are described in Figures 55, 56, 59 through 71, and Tables 8 and 9. This subject, as well as that of deposits in general, has been considered extensively, as shown in Figure 81, by Varrin,[73] who suggests a schematic view of how deposits and their morphologies on free surfaces evolve with time. It is reasonable that such surfaces would sequester impurities that possibly could concentrate and accelerate corrosion. However, such interactions have not been investigated extensively.

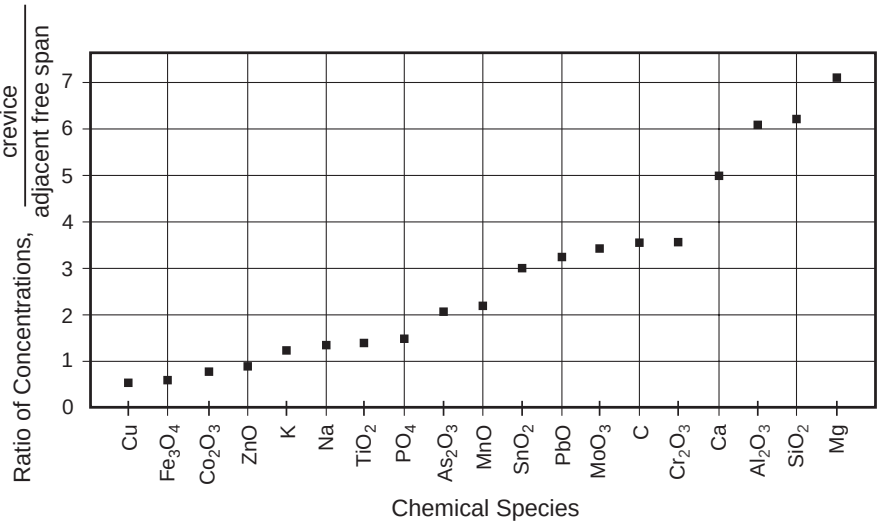

FIGURE 67. *Ratio of concentrations of species in deposits from occluded heat-transfer crevices vs those from adjacent free-span surfaces. Species given in ascending order of ratio. Data from 340 pulled tubes. From Cattant, et al.[171] Courtesy EDF.*

4.8 Significance

4.8.1 Experience —

1. Environments in heat-transfer crevices are subjected to many influences that cause the chemical compositions inside to vary greatly in spite of the well-controlled bulk secondary environment. Influences affecting the chemistry inside heat-transfer crevices include variations among the concentrations of impurities, temperature gradients, variations of packing of deposits including corrosion products, variations of the extent of the local steam phase, variations in volatility of species, and in the location of the steam/water interface. In view of such differences, it is not surprising that the occurrence of significant corrosion, as influenced by local environments in heat-transfer crevices, is so variable.
2. In addition to the usual impurities found in feedwater, lead and sometimes arsenic are present and have been shown to promote SCC as shown in Section 5.0. The fact that extensive SCC due to lead is not observed in many cases is probably due to the combination of lead with anions such as silicate, chloride, iron oxide, and others that form compounds of very low solubility. These lead-forming compounds may be important in suppressing PbSCC.
3. N_2H_4 and H_3BO_4 have been shown to mitigate some of the forms of corrosion that affect SGs, especially SCC. However, despite their use, already initiated SCC continues to propagate. It is not known whether their use from start of operation would prevent initiation of IGC/SCC.

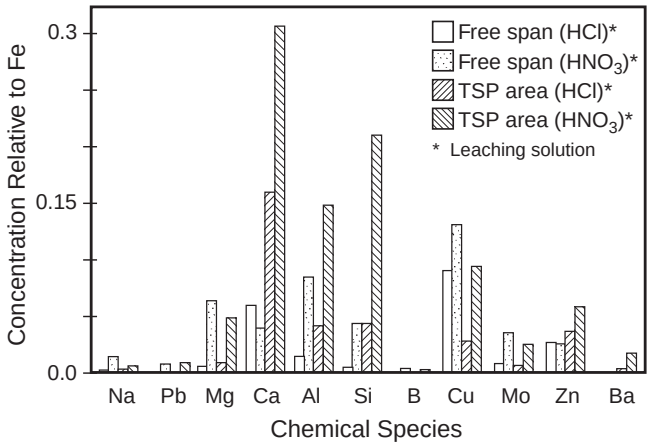

FIGURE 68. *Concentration of species relative to Fe vs species for measurements from free-span and occluded regions of heated crevice. Two different acidic extraction environments used. From Laire.[175] ©1995 NACE International.*

4. The presence of N_2H_4, while mitigating some forms of SCC, also reduces sulfates to lower valence species including sulfides. These have been shown to produce SCC readily in many Ni-based alloys, and to produce SCC in Alloy 690 under caustic conditions. Thus, the use of N_2H_4 needs to be considered carefully in view of the occurrence of reduction processes that are not desirable.
5. In the upper bundle of OTSGs where the environment is superheated, SCC and IGC are occurring and the chemistry of surface environments is probably quite similar to those in heat-transfer crevices.
6. While, in detail, the occurrence of corrosion is variable owing to the many influences inside

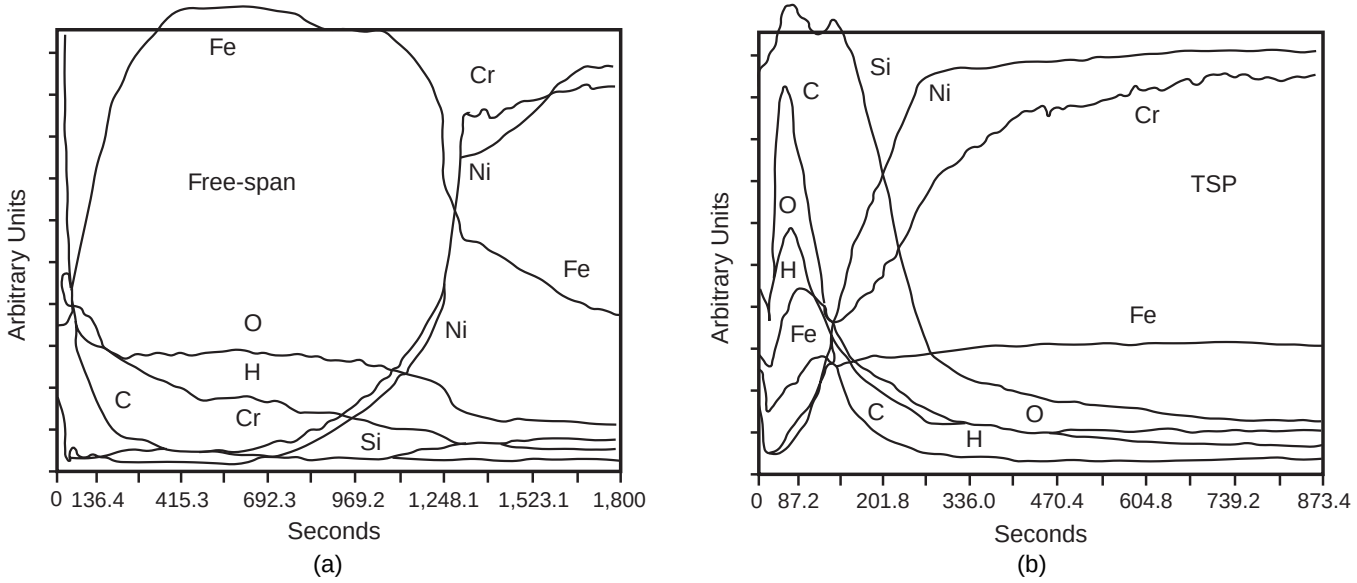

FIGURE 69. *Profiles of elements Fe, Cr, Ni, Si, C, O, and H in the inside layer L_{III} measured by glow discharge optical spectrometry (GDOS) in deposits at free-spans and in the occluded region from the third layer corresponding to Figure 59 and Line 1 of Table 9. From Cattant, et al.[171] Courtesy EDF.*

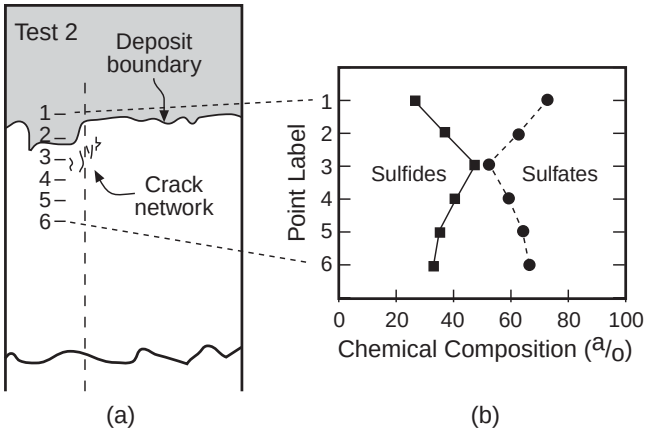

FIGURE 70. *Results from model boiler experiments with primary temperature in the range from 330°C to 350°C and secondary-side temperatures in the range from 290°C to 295°C with AVT chemistry. Sodium sulfate added at 0.5 mg/kg in makeup water, and N_2H_4 was in the range from 10 μg/kg to 50 μg/kg. Dissolved oxygen less than 1 μg/kg. (a) Location of SCC, boundary of deposit, and locations of analysis for sulfates and sulfides (1 through 6) for Alloy 600MA. (b) Atomic percent of sulfates and sulfides vs distance from the boundary of the deposit into the metal and through the SCC. From Daret, et al.[176] Courtesy of TMS, Warrendale, Pennsylvania.*

crevices, there is broad agreement in patterns of chemical composition as determined from hideout return and examination of deposits. However, these results do not strongly point to any specific local environments that produce IGC/SCC.

7. There are clear differences between the chemistry inside heat-transfer crevices and immediately adjacent on free surfaces. For example, alumino-silicates are much more prominent inside the crevices. Also, alkaline-forming species are more prevalent inside crevices where they seem to have concentrated preferentially to forming on the free-spans adjacent to crevices.
8. In the heat-transfer crevices of deaerated environments, there is little difference in potential between the outside surface and the inside surface owing to the propinquity of the NiO/Ni and H_2O/H_2 half-cell equilibria. Thus, there is no basis for significant potential gradients inside the heat-transfer crevice except for effects of pH on the equilibrium potentials of the half cells and oxidation effects prior to and just after startup.
9. Existing modeling of heat-transfer crevices does not provide the adequate detail needed to predict quantitatively the factors that affect the occurrence of corrosion of tubes.

4.8.2 Potential Problems and Approaches —

1. In view of the importance of predicting longer lives of steam generators where deposits accumulate in line contact crevices, modeling should be substantially improved. Specifically considered should be the presence of local steam environments, steam/water interfaces, the chemical reduction of sulfates as well as other chemical transformations, the partition of species within crevices in both radial and axial directions as a result of the different volatilities, the chemistry of precipitating lead compounds, the general formation of compounds, and the possible capacity of

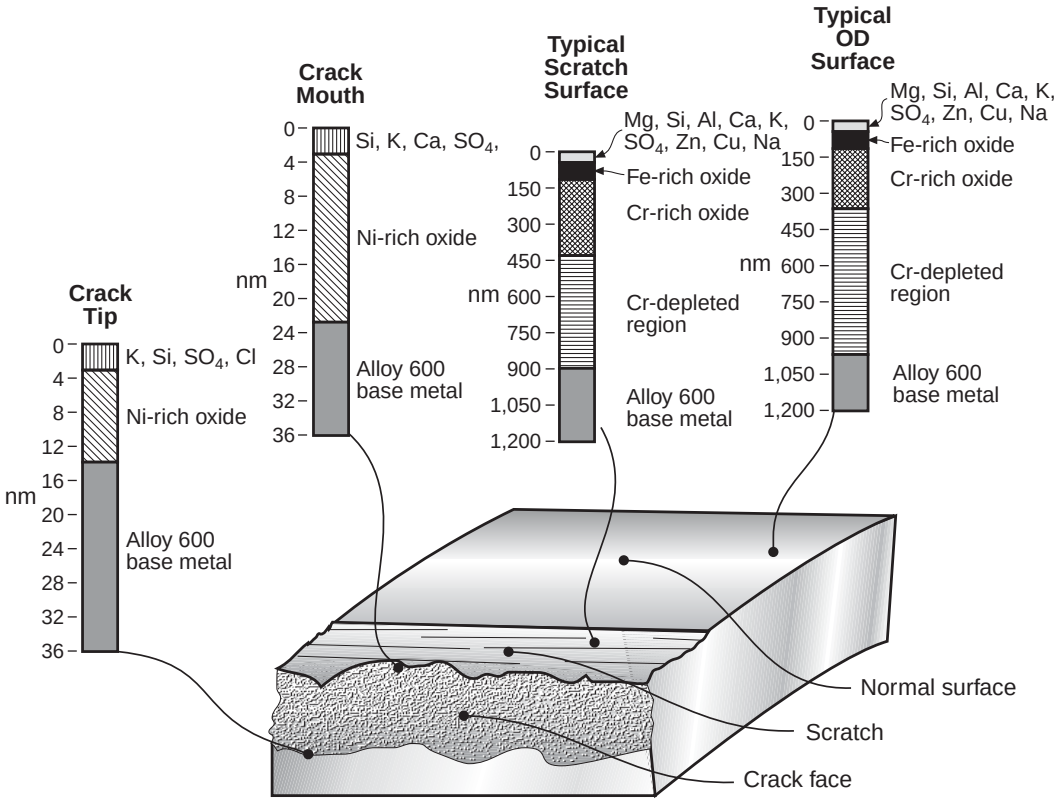

FIGURE 71. *Compositions of surfaces of tubes at four locations in the upper bundle of Oconee Nuclear Station. Outside and inside SCC and IGC as determined by Auger spectroscopy. From Rochester.[185] Courtesy BNES.*

oxidizing species that enter the steam generator with the feedwater to reach crevices and increase the potential. Models, to be useful, must consider such complexities of local environments that are discussed in this section.

2. Evaluations of crevice deposits and oxides of samples removed from plants provide one of the most useful approaches for determining the chemical and electrochemical conditions that develop in crevices and for validating models. However, these evaluations are hampered by a lack of reliable baseline data relating the composition and morphology of the deposits and compounds to the bulk water chemistry. Also, model boiler experiments should be undertaken to obtain such information as well as to evaluate the behavior of deposits at line contact geometries. Further, additional studies of deposits and crevices removed from operating plants should be undertaken.
3. To further improve the capacity to model the uncertain heat-transfer crevices, the heated crevice experiments using electrochemical monitoring should be applied to line contact geometries.

5.0 MODES AND SUBMODES OF CORROSION

5.1 Introduction

In the framework of the corrosion-based design approach (CBDA)[147] for predicting and assuring performance, the most important first step is defining local environments on the surfaces of components or subcomponents. For the SG, the local environments, where corrosion has been the most aggressive on the secondary side, are in heat-transfer crevices. The step of environmental definition is discussed in Section 3.0 for the bulk environment and in Section 4.0 for the local heat-transfer crevices. For the purpose of this discussion, the second step in the CBDA, alloy definition, comprises the choice of Alloys 800, 600, and 690 in their various heat-treated modifications. The evolution of the application of these alloys is shown in Figure 92. Some features of material definition are discussed in this section as they interact with the submodes of SCC. This section, 5.0, is concerned with the third step in the CBDA, defining the modes and submodes of corrosion. Alloy compositions and structures as they interact with the submodes of corrosion are discussed in this section. In the fourth step of the CBDA, superposition, the dependencies of the modes and submodes are compared with the properties of environments, as in

TABLE 13

Chemistry Inside Cracks at Increasing Elevations Inside OTSG[A]

Elevation (m)	Composition (a/o)														
	Ni	Cr	Fe	O	C	N	Si	Al	Mg	Ca	Sulfate	Sulfide	Zn	Na	Ni/Cr
8.8	16.93	1.62	—	34.43	40.91	2.61	1.77	—	—	—	0.14	—	—	0.88	10.45
10.1	15.15	1.60	0.07	35.99	41.38	0.58	3.39	—	—	—	0.18	—	Trace	—	9.47
10.4	6.41	0.64	—	37.04	39.07	—	6.25	10.12	0.48	—	—	—	—	—	10.02
11.2	6.19	2.90	0.89	29.47	46.22	1.23	3.31	8.79	—	0.76	—	—	—	—	2.13
11.8	9.21	1.52	0.76	34.98	49.20	—	2.78	—	—	—	—	0.83	—	0.57	6.06
12.6	13.30	0.94	0.80	45.62	35.11	1.17	1.56	—	—	—	0.45	—	—	—	14.15
13.8	18.51	2.38	0.90	31.91	41.08	—	4.67	—	—	—	0.55	—	—	—	7.78
14.2	9.78	2.48	0.58	39.12	43.13	1.21	2.01	—	0.38	0.37	0.42	0.22	—	0.33	3.98
15.0	11.58	0.93	—	41.06	45.12	0.89	—	—	—	—	—	0.42	—	—	12.45
16.7	6.02	2.72	1.53	37.27	41.48	0.09	3.33	3.82	1.42	1.09	0.79	—	0.09	—	2.21
Ductile fracture	16 to 21	2 to 3	0.5 to 1.6	27 to 34	41 to 48	—	1 to 3	—	—	—	—	—	—	—	6.3 to 7.9

[A] From Rochester and Eaker.[184] Courtesy of TMS, Warrendale, PA.

TABLE 14

Chemical Analyses by Nano-EDS (0.7 nm spot) of Local Regions. Near Tip of SCC as Identified by TEM[A]

Location Designation No.	a/o O	a/o Si	a/o S	a/o Ca	a/o Cr	a/o Fe	a/o Ni	a/o Pb	Ni/Cr	Impurities
49	26.5	0.3	0.3	0.0	33.7	4.5	32.8	2.0	0.97	Cr-Ni-O with Pb
50	2.3	0.5	0.2	0.0	11.4	7.7	80.8	0.2	7.1	Metal matrix
51	0.7	0.0	0.1	0.0	3.8	2.1	91.5	2.6	24.1	Fe-Cr-depleted boundary—with Pb
52	1.5	0.0	0.0	0.0	2.6	2.3	94.2	0.4	32.4	Fe-Cr-depleted boundary—with minor Pb
53	30.2	0.6	0.2	0.1	30.3	12.4	25.3	1.2	0.8	Cr-Ni-O with Pb
45	21.1	0.4	3.7	0.1	23.8	6.3	37.2	7.5	1.6	High Pb, S in degraded GB particle
48	28.8	0.7	2.7	0.0	30.1	5.8	29.2	4.6	0.97	High Pb, S in degraded GB particle
31	25.3	0.2	0.4	0.0	38.2	3.6	28.8	7.7	0.7	High Pb in degraded GB particle

[A] From Rochester.[185] Courtesy of BNES.

Section 4.0, to determine whether significant corrosion can occur.

The purpose of Section 5.0 is to define the present state of understanding of the modes and submodes of corrosion of Alloys 600 and 690 as applied in steam generators. Alloy 800 is not discussed extensively, although available data are integrated into this discussion. For each submode, the "state of understanding" is based on the extent to which seven principal variables affecting corrosion (pH, potential, species, alloy composition, alloy structure, temperature, and stress) can be quantified. Important aspects for the background of Section 5.0 are as follows:

1. Modes and Submodes — The background of modes and submodes of corrosion has been discussed extensively.[124,147,208-209] A "mode" of corrosion is the morphology of the corrosion, e.g., general (GC); pitting; IGC; SCC, which can be either intergranular or transgranular (SCC, IGSCC, TGSSC); and corrosion fatigue (CF). A "submode" refers to a given mode, e.g., SCC, that occurs according to unique dependencies. Thus, when SCC in Alloy 600 occurs in alkaline environments, AkSCC, the dependencies of this submode are quite different from those of low-potential SCC (LPSCC).

Figure 82 shows the major and minor submodes for the SCC of Alloy 600MA in the range of temperatures from 300°C to 350°C. The four major submodes of SCC, as shown in Figure 82(a), are AkSCC, LPSCC, acidic SCC (AcSCC), and high-potential SCC (HPSCC).

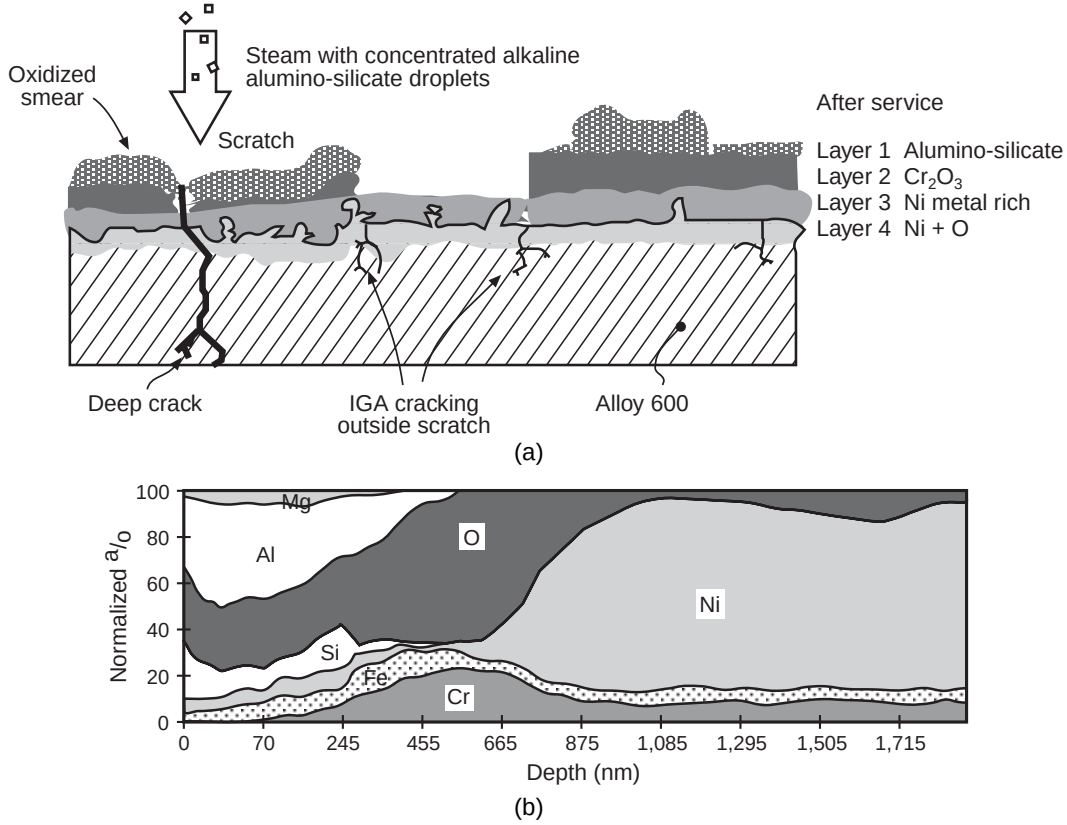

FIGURE 72. *(a) Schematic view of SCC and IGC together with four chemical layers on surface from upper bundle of tubes from the Oconee Nuclear Station. (b) Distribution of chemical species on OD surfaces from the 11th TSP in ONS-2 from tube R93T69. From Rochester and Eaker.[184] Courtesy of TMS, Warrendale, Pennsylvania.*

These same submodes are common to the stainless steels and low-alloy steels as shown by Parkins[116] and Congleton, et al.,[117] in Figure 83. In Figure 83(b), it is shown that the minimum intensity in the anodic submodes of SCC of steel occurs at the solubility minimum for iron. Such a minimum in the SCC of Alloy 600MA also occurs as shown in Figure 46. Further, such solubility minima for the Fe, Cr, and Ni oxides are shown in Figure 38 and indicate expected minima for SCC with pH.

The major submodes in Figure 82(a), generally, tend to be associated with thermodynamic patterns that affect the stability of protective films. While this connection is qualitative, following the pattern of Figure 83 where the minimum in SCC depends on the solubility minimum for iron oxides, each of the submodes depends generally on recognizable features of the potential-pH diagrams: e.g., LPSCC is usually in the region near and below the standard hydrogen equilibrium, although some argue that the NiO/Ni half-cell equilibrium is more relevant. AkSCC occurs in a region of transition between stable and unstable NiO. Similarly, AcSCC occurs comparably in the neutral to mildly acidic region. HPSCC corresponds with the breakdown of protective films at higher potentials and seems especially associated with the instability of chromic oxide (Cr_2O_3) at higher potentials as shown in Figures 7 and 73 in the alkaline region.

Figure 82(a) also shows three lines: $HPSCC_{MA}$, $HPSCC_{SNP}$, and $HPSCC_{SNC}$. These designations refer to HPSCC associated with the mill-annealed condition (MA), the sensitized condition (SN) in pure water (P), and the sensitized condition (SN) in contaminated water (C). The locations of these lines and their slopes are estimated.

The major submode LPSCC was formerly called "primary water SCC" (PWSCC). However, there is good evidence that the same mechanistic process occurs on the secondary side. Further, to give a submode of SCC the title of a component or location is no more logical than to call the ammonia SCC of brasses "condenser SCC" or the SCC of martensitic stainless steel in steam turbines "turbine SCC." The term, LPSCC, is now widely used and applies to the region of potentials in Figure 82(a), where this submode occurs just as AkSCC uniquely occurs in the alkaline region and is mechanistically related to the effects of high pH.

Identifying the submodes by their chemical locations as in Figures 82 and 83 is descriptive of the conditions that account for their uniquenesses; the

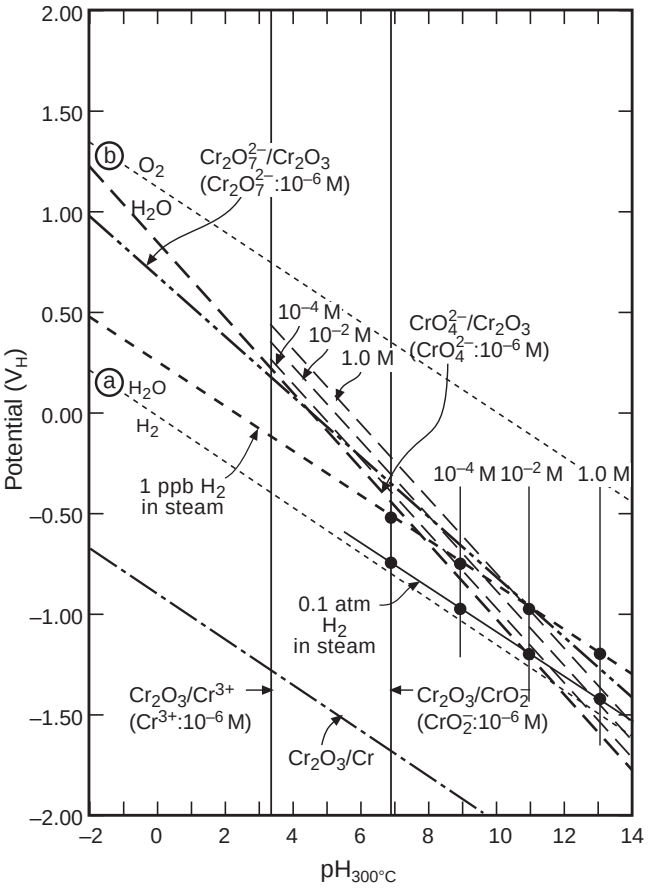

FIGURE 73. *Potential vs pH for the Cr-H_2O equilibria at 300°C. Equilibria shown for Cr^{3+} to Cr^{6+} and Cr^{3+} to Cr^{3+} for solubilities from 10^{-6} M to 1.0 M. Diagram from Chen, et al.[108]*

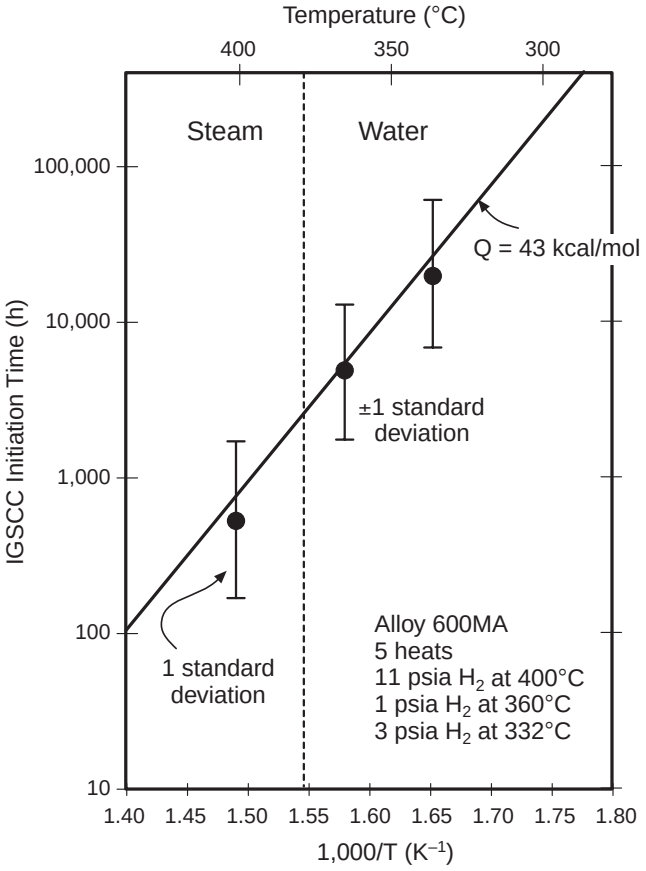

FIGURE 74. *IGSCC initiation time vs reciprocal temperature for five heats of material from 19 mm OD tubing of Alloy 600MA. Bars show the range of 20% and 80% of specimens failed. From Economy, et al.[186] ©1987 NACE International.*

use of this approach does not encroach on mechanistic interpretations. For example, LPSCC is called by some workers "hydrogen embrittlement" because of the relatively low potential of its domain. The action of hydrogen here is believed to affect the dislocation flow process but does not produce direct brittleness. Further, to call, for example, AkSCC "anodically controlled" avoids the possible critical role of hydrogen at the crack tip. Thus, the approach of describing the submodes in essentially phenomenological and chemical terms describes the essential conditions for occurrence of the submodes without presuming on any of the possible mechanisms by which the SCC initiates or propagates.

Incidentally, some have suggested that PWSCC means "pure water SCC." This is misleading since, although the phenomenon has been studied mainly in relatively pure water, there is no reason that this mechanistic process cannot occur in chemically modified solutions such as those that occur on the secondary side. Thus, again, the important descriptive term should be LPSCC.

The minor submodes are distinguished as a group in Figure 82(b) partly because they are not so well defined and also because their domains do not relate so readily to features of the potential-pH diagram as do the major submodes. Further, some of the minor submodes, e.g., in the acidic region, may be part of the same submodes, as is discussed in Section 5.2.3. As shown in Figure 82(b), the minor submodes of SCC are:

a. Copper-acidic SCC (CuSCC) as initially studied by Pierson and Laire.[210] CuSCC is taken here as being part of the acidic submode since it appears that it belongs in this category by virtue of its dependence upon acidic environments. The copper, in the form of CuO, seems to act as an oxidizer just as it operates in AkSCC.
b. AcSCC as initially studied by Jacko.[211] This submode is probably more of a "sulfate SCC," because AcSCC has been studied mostly in sulfate solutions. Further, SCC in sulfate solutions has been the most extensively studied of the acidic submodes.
c. Chloride SCC (ClSCC) as initially reported by Berge and Donati[212] and by Berge, et al.,[213] in a solution of H_3BO_4 and Cl^-. While this

submode has not been studied extensively, its initial patterns indicate that it should be considered a part of AcSCC.

d. DSSCC as initially reported by Dehmlow.[187]

e. PbSCC that occurs over the full range of pH as initially reported by Copson and Dean.[214]

f. Reduced sulfur SCC (S^{y-}SCC) as initially reported by Gomez-Briceno and Castano.[215]

g. SCC in alumino-silicate surface chemistry (ASSCC) as described by Sala and coworkers.[164-166] This submode is taken here as an extension and as part of AkSCC since it seems to have important similarities.

h. SCC in organic environments (OgSCC) according to speculation about the possible effects of the organic species observed in deposits as shown in Figures 59 through 66. There is no authoritative work yet on this subject; existing work suggests that there is little effect of organic environments by themselves as observed in Figures 59 through 66. However, there is so little work on this subject that it is not possible to determine the domains of existence.

i. Low-temperature SCC (LTSCC) as reported by Brown and Mills.[216]

During inspections of SG tubing with eddy-current probes, it is often not possible to determine the submode without further investigation. However, it is usually possible to determine whether the SCC is starting from the outside or inside. When the SCC is starting from the inner primary-side surface, it is inside diameter SCC (IDSCC), although it is sometimes assumed to be LPSCC. When SCC starts from the outside secondary surface, it is usually called outer diameter SCC (ODSCC). Sometimes, where there is not sufficient precision, the ODSCC is called IGA and includes both SCC and IGC.

It is reasonable that CuSCC, AcSCC, and ClSCC, as shown in Figure 82(b), may all be part of the same

Material	Stress (ksi)	IGSCC (Y = yes, N = no)*			
		7 days	14 days	21 days	56 days
Alloy 600	0	Y	Y	Y	No specimen
	10.3	N	Y	Y	Y
	20.5	Y	Y	Y	Y
	30.8	Y	Y	Y	Y
Alloy 690	0	N	N	N	N
	20.1	N	N	N	N
	40.1	N	N	N	N
	60.2	N	N	N	N
EN82H	0	N	N	N	N
	7.7	N	N	N	N
	15.5	Y	Y	Y	Y
	23.2	Y	Y	Y	Y
R127	0	N	N	N	N
	19.6	N	N	N	N
	39.2	N	N	N	N
	58.8	N	N	N	N

* Environment: 11 psi hydrogen, 3,000 psig, 400°C steam; water doped with: 100 ppm sodium sulfate, 100 ppm sodium nitrate, 100 ppm sodium chloride, 100 ppm sodium fluoride.

FIGURE 75. *Threshold beam results from testing two wrought alloys and two weld metals in doped steam at 400°C with four additions of species, each at the 100-ppm concentration. From Dehmlow.[187] Used by permission of EPRI.*

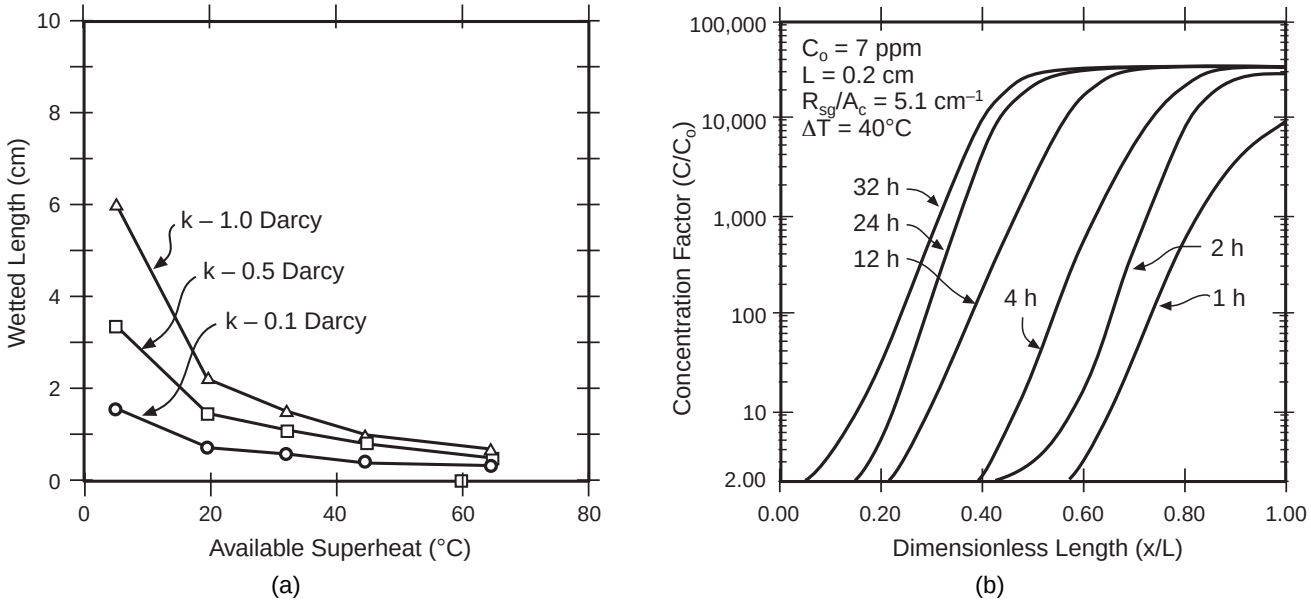

FIGURE 76. *(a) Wetted length vs available superheat with varying permeability for initial conditions in a heated crevice. (b) Concentration factor vs dimensionless length as a function of time. C_o = bulk density concentration; L = depth of crevice or deposit; R_{sg} = SG tube circumferences; A_c = heated area; ΔT = superheat. From Millett, et al.[190]*

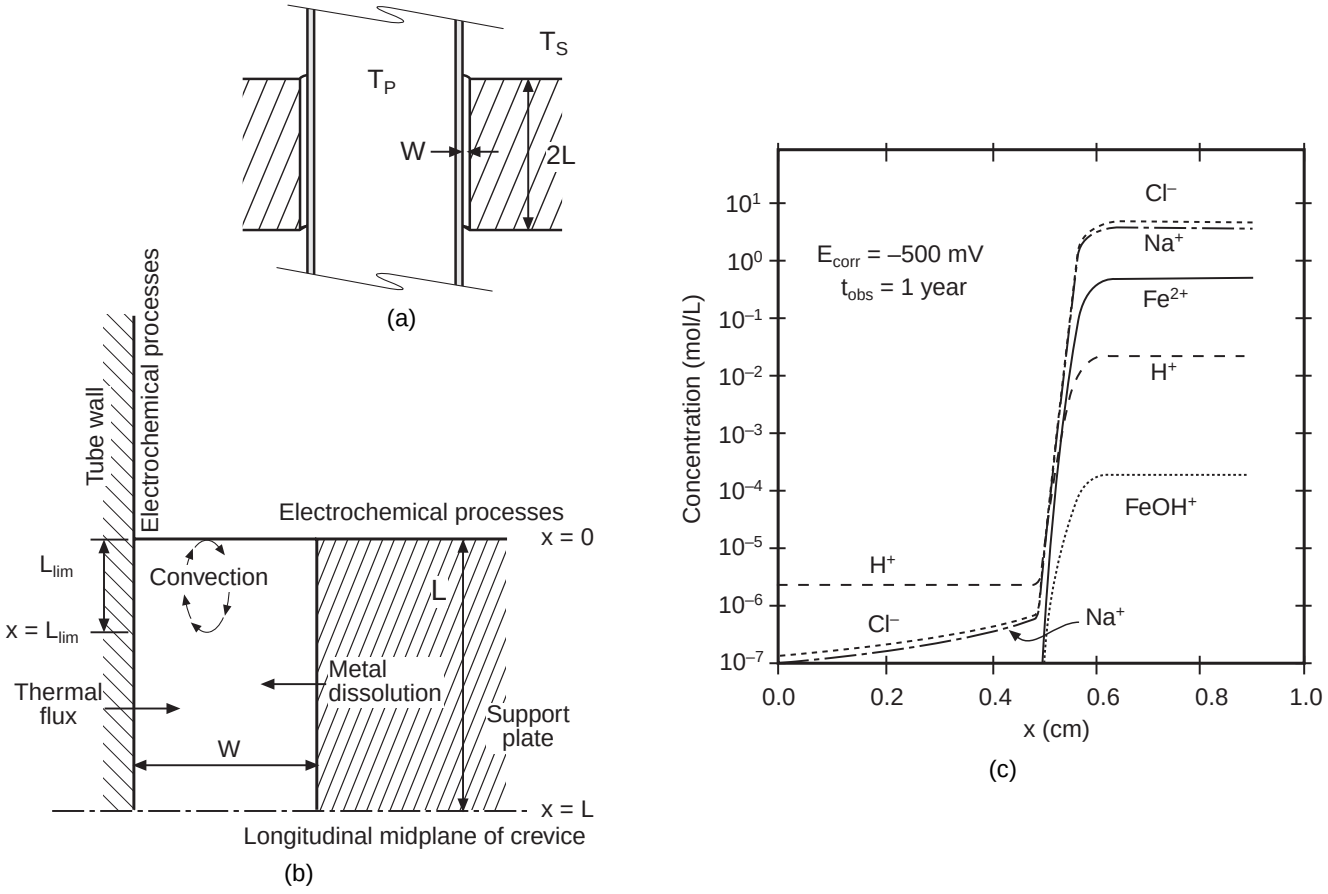

FIGURE 77. *(a) and (b) Model for calculating properties of heat-transfer crevices using hydraulic and electrochemical elements. Crevice is 2L long. L_{lim} is distance over which convective processes operate. (c) Concentration vs distance from mouth of crevice to midpoint after 1 year with an external corrosion potential of E_{corr} = –500 mV. From Engelhardt, et al.[196] ©1999 Elsevier Science.*

submode, AcSCC, as discussed in Section 5.2.3. The S^{y-}SCC, as discussed in Section 5.2.6, is clearly a separate submode since its dependencies are different from the others, and it is aggressive toward Alloy 690 at high pH. It is also possible that the ASSCC is part of the AkSCC, as discussed in Section 5.2.1; but this, like the aggregation of AcSCC, has yet to be confirmed. The PbSCC, as discussed in Section 5.2.5, is also a clearly different submode since its dependencies are not similar to any of the other submodes; in fact, it is likely that species such as Sb and As may produce SCC phenomena similar to those of lead.

SCC of the high-nickel alloys has not been studied extensively in the organic acids that have been identified in the deposits of Figures 59 through 66. In view of the well-known ionic complexations between nickel and some organic species, it is likely that these organic species could produce SCC. Work to date has considered mostly acetates to epitomize organic species. However, the behavior of acetates may be quite different from formates, which are also observed. Carbon-nitrogen ligands also should be considered.

Scott and Combrade,[217] Combrade, et al.,[218] and Combrade,[219] as shown in Figures 84(a) and (b), have developed diagrams similar to that in Figure 82(a). Figure 84(a) illustrates the three submodes relevant to the secondary side of SGs together with the domain of potential and pH for the secondary side similar to Figure 39. The secondary domain in Figure 84(a) seems not to consider the effect of N_2H_4 as shown in Figure 45(a), although the upper bound seems consistent with the low H_2 in the secondary side as shown in Figure 33. Also, the extents of the three submodes do not reflect the contours of potential and pH described in Section 5.2. Figure 84(b) provides mechanistic interpretations of the submodes together with their extents.

Another version of the approach in Figure 82(a), defined by an organized experimental program and review of literature, has been developed by Ohsaki, et al.,[220] and Tsujikawa and Yashima,[221] and is shown in Figure 85. This figure does not include LPSCC or a full description of HPSCC. Also, Figure 85 does not account for the extent of AkSCC and AcSCC as described in Sections 5.2.1 through 5.2.3.

The broad use of the mode diagram framework for the Alloy 600, 690 group in Figures 82 through 85 shows that this approach is useful and is based on reliable data. The ranges of the submodes as described in Figures 82 through 85 differ somewhat in details of the ranges of the submodes, but they agree well on the general locations and extent of the submodes with respect to pH and potential.

The mode diagrams do not give rates nor do they indicate dependencies upon variables, e.g., microstructure, other than potential and pH. The other dependencies are discussed in 5.1.2 and in the respective subsections of Section 5.2, which deal with the submodes. Nonetheless, potential and pH are the dominant variables since the tubing alloy sets the submodes; temperature is set by operating conditions; and stress is usually in the range of the yield stress owing to methods of fabrication. With thermal treatment and careful installation, stresses can be relatively low at tube support crevices. There is no evidence for high stress in TT tubes at the TSPs in the absence of denting or scratches.

2. Seven Primary Variables — To define a submode is to define its dependence on the "seven primary variables" as illustrated in Figure 86. Here, the general relationship is widely used for correlating SCC data, although such a formulation does not apply to all modes and submodes nor are the same mathematical dependencies always applicable. In the case of the stress variable, there are modifications having to do with crack growth, cyclic stressing, and ranges of stress; however, these are subsumed in the implication of stress being an important variable. Finally, some of the dependencies are interrelated such as the chemical activation energy and the stress exponent.[222-223] The submodes are principally distinguished by their different dependencies upon the seven primary variables as can be seen simply from the different locations of submodes in Figures 82 through 85. Important dependencies are described in discussions on the respective submodes in Section 5.2.

3. Initiation and Propagation — Much of the data upon which the mode diagrams of Figures 82 through 84 are based comes from tests using initially smooth surfaces or from constant extension rate test (CERT) specimens. In these cases, the SCC responds mainly to the environmental chemistry as it occurs directly on surfaces. However, as a crack propagates and is progressively less connected chemically with the surface, it is reasonable to expect that propagation might depend more on the electrochemistry of the crack tip and less on the details of the surface chemistry. The bounding aspects of this condition are illustrated in Figure 41 and the associated discussion. While it seems possible that conditions for initiation and propagation might differ, the comparisons between initiation and propagation, which are

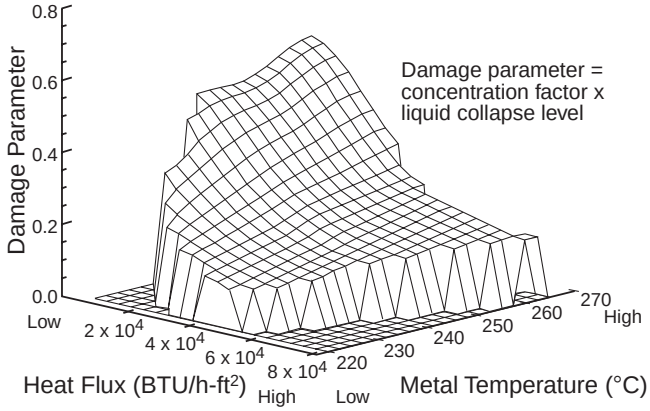

FIGURE 78. *Surface plot of damage parameter vs heat flux and metal surface temperature for a heat-transfer crevice as calculated using computational fluid dynamics. The liquid collapse level = equivalent height of liquid volume fraction in the heat-transfer crevice assuming complete stratification. From Keefer and Keeton.[198] ©1996 NACE International.*

discussed in connection with Figure 88, suggest in some cases that there is little difference in chemical conditions that control initiation and propagation.

Details of what constitutes initiation and propagation have been discussed in detail by Staehle.[61,224] However, these stages can be divided simply by considering Figure 87. Here, the log of stress vs the log of crack depth is plotted, and the formats that apply to correlating the data from smooth and pre-cracked surfaces are identified. As illustrated in Figure 87(a), SCC data from initially smooth surfaces are usually correlated by a plot of stress vs time to produce a threshold or a quasi-threshold; whereas, SCC data from pre-cracked specimens are plotted as crack growth rate, da/dt, vs stress intensity. From this plot, a value, or at least a practical value, of $K_{I_{SCC}}$ is obtained, and an array of such values is shown in Figure 87(b).

Using Figure 87(b), assuming that a reasonable threshold stress for AkSCC of Alloy 600MA is 100 MPa and that a reasonable value for $K_{I_{SCC}}$ is 5 MPa $m^{1/2}$, the intersection of this horizontal line at 100 MPa and the –1/2 sloping line of 5 MPa $m^{1/2}$ occurs at about 800 μm, which is close to three quarters of the full thickness of a tube in a steam generator. This result indicates that much of the penetration of a steam generator tube from the secondary side occurs in the initiation regime. For thicker applications, such as control rod drive mechanisms (CRDM), the fraction of time in the propagation region increases. However, even for CRDMs, a relatively small fraction of the failure time is probably in the propagation regime.

To assess the chemical dependencies of initiation vs propagation, Figures 88(a) through (c) compare the dependence of the initiation of SCC for various alloys upon the concentration of NaOH (Figure 88[a])

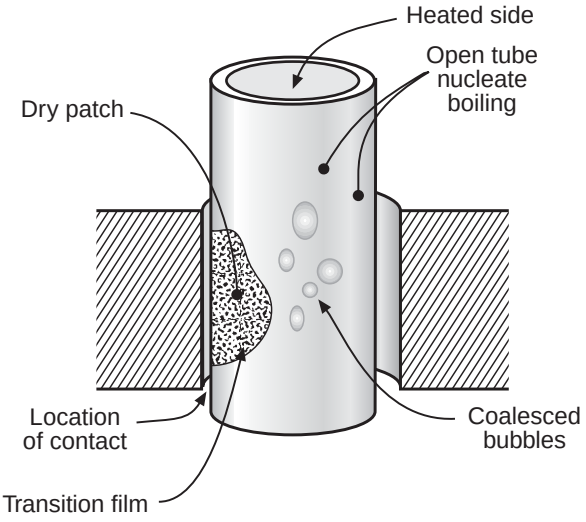

(a)

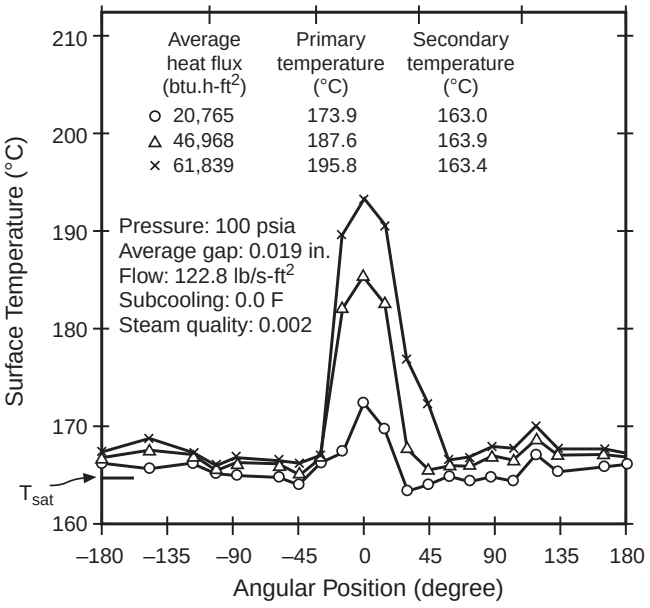

(b)

Drypatch Size and Location, 1-in. Cylindrical Crevice

Heat flux, Btu.h-ft^2	89,000				23,000			
Pressure, psia	876				825			
Surface tension	Yes		No		Yes		No	
Pressure drop, psf	8	6	8	6	8	6	8	6
Bubble axial length, in.	0.420	0.620	0.480	0.807	0.246	0.284	0.460	0.626
Bubble area, in.^{2}	0.160	0.333	0.190	0.423	0.094	0.127	0.183	0.343
Axial location in the land, in.	0.580	0.380	0.520	0.112	0.522	0.388	0.540	0.294

(c)

FIGURE 79. *(a) Model for calculation of dry patch location and dimensions for vertical 1-in.-long, deposit-free heated crevice with the tube located asymmetrically and in contact with the tube support at 0°. From Duncan, et al.[199] (b) Surface temperature of tube vs angular position as a function of heat flux. 0° corresponds to the contact point. From the work of Bankoff and Tankin,[207] reported by Duncan, et al.[199] (c) Size of dry patch and location in a vertical cylindrical crevice 1 in. in length as a function of heat flux, pressure, surface tension, and pressure drop. From Duncan, et al.[199] ©1996 NACE International.*

with the response of pre-cracked specimens (Figures 88[b] and [c]) of Alloys 600 and 690. This comparison shows that the dependence of initiation upon the concentration of NaOH is about the same as that for propagation. A similar comparison is shown in Figures 88(d) and (e) for initiation and propagation of HPSCC for sensitized Type 304 (UNS S30400) stainless steel, respectively, as they depend on electrochemical potential. The minimum potential at which significant SCC stops, from an initiation point of view, is generally regarded as –240 mV_H. The use of CERT testing shown in Figure 88(d) shows that such a potential may be slightly conservative. This limit of –240 mV_H for propagation seems to occur at a lower plateau, as shown in Figure 88(e), of velocity that corresponds to about 2×10^{-12} m/s or about 100 μm of penetration per year after initiation occurs. –240 mV_H seems to define the upper objective of potentials sought with hydrogen water chemistry. Thus, the dependence of HPSCC on potential for both initiation and propagation is similar.

The comparisons in Figures 88(a) through (c) suggest that the initiation and propagation exhibit similar dependencies for the AkSCC. This same pattern applies to the potential dependence of HPSCC in oxygenated pure water, shown in Figures 88(d) and (e), where the lower threshold of electrochemical potential is about the same for specimens with initially

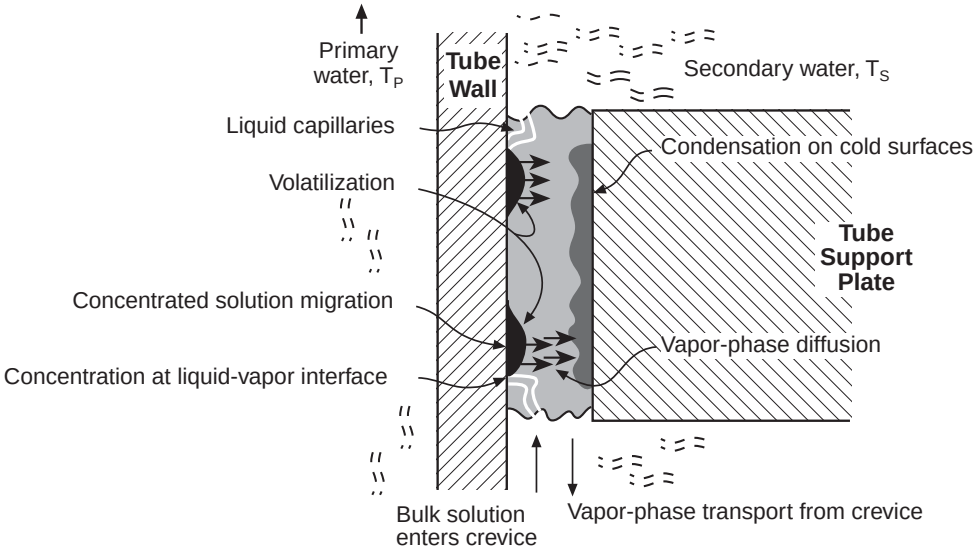

FIGURE 80. *Volatile solute mass-transport processes in heated crevices at TSPs. From Baum.[203] Used by permission of EPRI.*

smooth surfaces and pre-cracked specimens. Whether these similarities in conditions, which control initiation and propagation, apply to all submodes is not clear; further work is necessary for developing credible predictions.

4. Chronology — The development of Alloys 800, 600, and 690 for applications to nuclear steam generators starts with the work of Copson in 1957,[227-228] where he studied the effect of nickel concentration at constant 20% Cr on the SCC of Fe-Cr-Ni alloys in boiling $MgCl_2$ at about 145°C and showed that no SCC occurred above about 45% Ni. His results are shown in Figure 89(a). It was assumed that any alloy that would not sustain SCC in such an aggressive environment generally would be resistant to SCC and especially to SCC in chloride solutions. If fact, the work of Berge and Donati[212] in 1981 showed that Alloy 600MA would sustain SCC in an acidic chloride solution, similar to the $MgCl_2$ environment, as shown in Figure 89(b), but at a lower temperature of 100°C. Thus, the prediction of Copson was not a general one. Nonetheless, it was the work of Copson that supplied the basis for choosing Alloy 600 for commercial applications as early as 1962, as shown in Figure 92.

At about the same time as Copson was reporting his work, Coriou, et al.,[1] reported in 1959 that an alloy similar to Alloy 600 would sustain SCC in pure deoxygenated water, although the SCC required several months to develop. Such a result seemed preposterous at the time. First, Copson's work showed that the Fe-Cr-Ni alloys resisted SCC in a very aggressive environment as shown in Figure 89(a). Second, at that time it was conventional to assume that SCC would only occur in the presence of specific species, e.g., brass in ammoniacal solutions. Third, the idea of a tough and ductile alloy, such as Alloy 600, sustaining SCC in a pure and deaerated environment was inconsistent with the prevailing understanding about only higher potentials accelerating SCC.

To explain what was the nominally incredible finding of Coriou, Copson undertook research on the effects of lead, which he suspected of causing the SCC observed by Coriou, and on specimens with crevice geometries exposed to oxygenated environments, which he thought[229] would also explain some of Coriou's results. The lead work was published with Copson and Dean[214] in 1965, and the crevice work was published with Copson and Economy[230] in 1968. The work in lead-containing environments showed that Alloy 600 would sustain rapid SCC and that the SCC could be either intergranular or transgranular. The work on crevices showed that, in oxygenated environments, the inside surfaces of a double U-bend crevice would sustain rapid SCC. During this time, Coriou continued to publish his work[231-233] and continued to show that Alloy 600 would sustain SCC in pure deoxygenated water in the absence of lead crevices. Coriou published a simple diagram comparing the general behavior of the Fe-Cr-Ni alloys in pure deoxygenated water and in chlorides; this diagram is shown in Figure 90.

Several other investigators showed that Alloy 600 would sustain SCC, including Rentler and Welinski[234] and Hubner and coworkers.[235-236] In about 1967, Siemens decided, based on their own work, on experience with the Obrigheim plant, and on the work of Coriou, to shift from Alloy 600 to a modified grade of Alloy 800 for SG tubing, which they have used to the present time with great success. Figure 90, although schematic, suggests that Alloy 800 should resist SCC in pure water and should be minimally prone to SCC

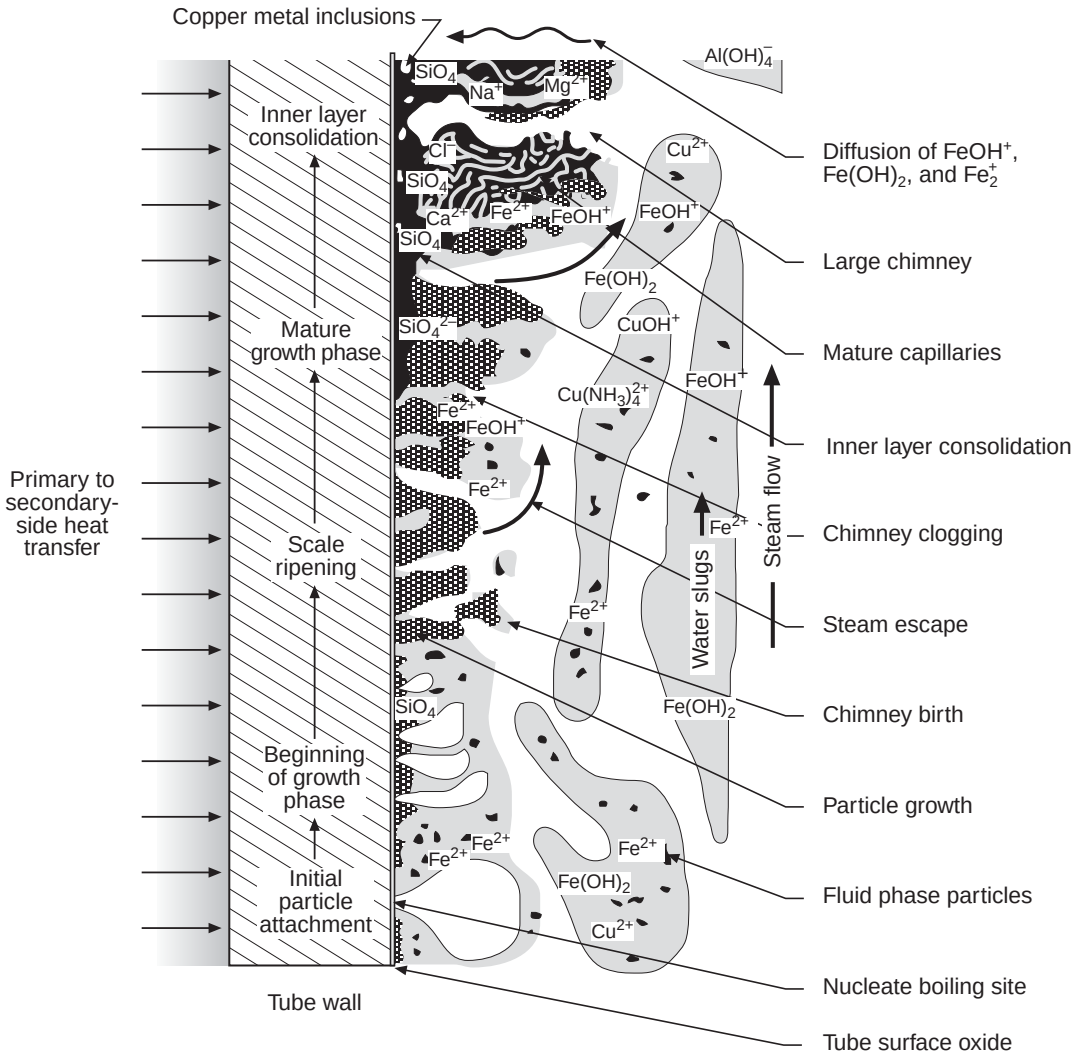

FIGURE 81. *Model for growth of tube deposits on free surfaces including important steps and morphologies. From Varrin.[71] Used by permission of EPRI.*

in chloride environments. This intuition was vindicated by later investigators.

When Coriou presented his work, including Figure 90, in 1967 during a meeting at The Ohio State University,[237] Copson prepared a detailed objection, part of which is excerpted here:

> In recent years there have been reports, such as described here today, showing intergranular corrosion and cracking of Alloy 600 in certain high pressure high temperature water environments. Naturally, we were surprised by this, and have made repeated attempts to reproduce such attack in pure water. One series of tests was run at Battelle Memorial Institute on specimens and water received from France. Careful micro-examination showed the absence of intergranular attack of any of these Alloy 600 specimens. (H.R. Copson, S.W. Dean, *Corrosion,* 21, 1 [1965], p. 1-8.)

"Continued laboratory testing soon revealed that certain contaminants in the water could promote attack. One of these was lead. In combination with tensile stresses a lead contaminant produced cracking which usually was predominantly transgranular, although in some instances the cracking was partly or largely intergranular. Another harmful contaminant was oxygen, but oxygen was detrimental only in the presence of both crevices and high tensile stresses. With this combination intergranular stress corrosion cracking occurred in the crevice area. The first results with these contaminants were included in the 1965 paper.

"We have continued the laboratory testing, and another paper dealing with oxygen contamination has been accepted by *Corrosion* for publication in 1968. This describes stress corrosion tests in pressurized water at 600°F using double bent beam specimens."[229]

Copson had explored some obvious avenues for explaining the results of Coriou; however, he did not recognize that, by the time of his objection, Coriou and coworkers had published three papers reproducing their initial results. Copson had missed the point that deaertion was the key factor supporting LPSCC based on the historical patterns of increasing oxygen accelerating SCC.

By about 1970 it had become clear that Alloy 600 was, indeed, resistant neither to the relatively pure water used for primary PWR coolants nor to the concentrated alkaline environments that could be expected in the heat-transfer crevices on the secondary side of steam generators with the then prevailing water chemistry as discussed in Section 3.0. As a result of the apparent deficiencies in Alloy 600, extensive work was undertaken to develop a replacement as described in the work of Flint and Weldon,[82] by McIlree and Michels[238] as shown in Figure 91, Figure 142 as discussed in connection with PbSCC in Section 5.2.5, and in Table 15 from the work of Copson, et al.,[239] on double crevices, which were exposed to oxygenated solutions.

Results from the work on double U-bend crevices in Table 25 shows that the Alloy 690 composition does not sustain SCC. Figure 142, which includes the 1972 work of Flint and Weldon[82] for the effects of alloy composition on corrosion in lead-containing solutions, shows again that the composition of Alloy 690 would be an optimum composition. These data are discussed in Section 5.2.5 concerning the PbSCC submode as well as in Section 5.3 concerning the selection of Alloy 690. The work by McIlree and Michels[238] in Figure 91, as well as the work by Sedricks, et al.,[240] shows that the Alloy 690 composition provides a substantial improvement over low-Ni alloys but is more prone to AkSCC than Alloy 600, even in what is approximately the TT condition. This result is not surprising in view of the high solubility of Cr in alkaline solutions. By about 1974, Alloy 690 was available for consideration by vendors of nuclear steam supply systems (NSSSs). The original MA heat treatment was modified to a TT heat treatment based on the relative success with the Alloy 600TT treatment and on the data shown for a sensitizing treatment in Table 16.

While the prevailing temperatures of commercial reactors, as shown in Figure 19, were relatively low in the early 1970s, which kept LPSCC from becoming a major concern, these temperatures were adequate to produce AkSCC and AkIGC; such failures occurred as discussed in Section 3.4. While the AkSCC-IGC was ameliorated by several changes in water chemistry, the fact that Alloy 600 could sustain such extensive corrosion was, by then, clear.

The final important event in this early history of Alloy 600 was the publication of research in 1973 by Blanchet, et al., that indicated sensitization of Alloy

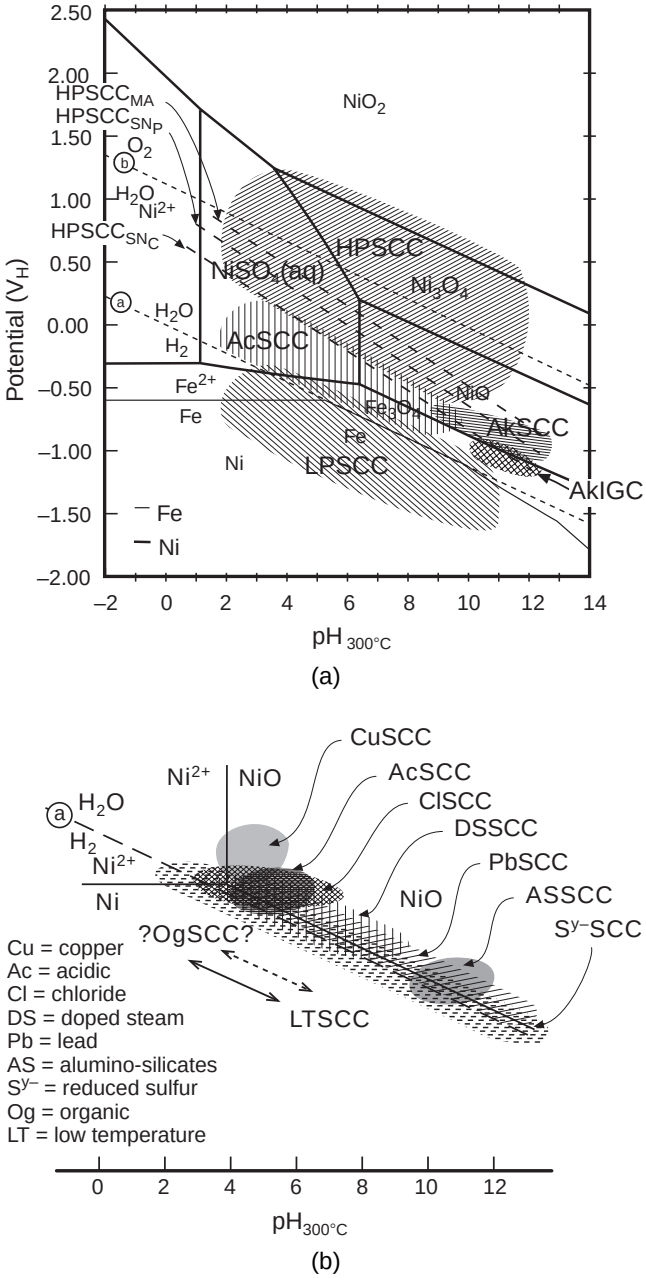

FIGURE 82. *(a) Major submodes of SCC plotted with respect to coordinates of potential for significant reactions of Ni and Fe at 300°C. Extent of the submodes based on experience from laboratories and reasonable interpolations and extrapolations. Submodes applicable to Alloy 600MA in the range from 300°C to 350°C. Diagram calculated based on a 0.01-M Na_2SO_4 titrant. (b) Minor submodes of SCC for Alloy 600MA plotted with respect mainly to the NiO/Ni half-cell equilibrium at 300°C.*

600 would improve its resistance to LPSCC, as shown in Table 16.[80] These results were then taken by the reactor manufacturers as a basis for the thermal treatment that was utilized with both Alloys 600TT and 690TT. The rest of the history of these alloys has been one of increasing use of Alloy 600TT for steam generators in units that were built in the

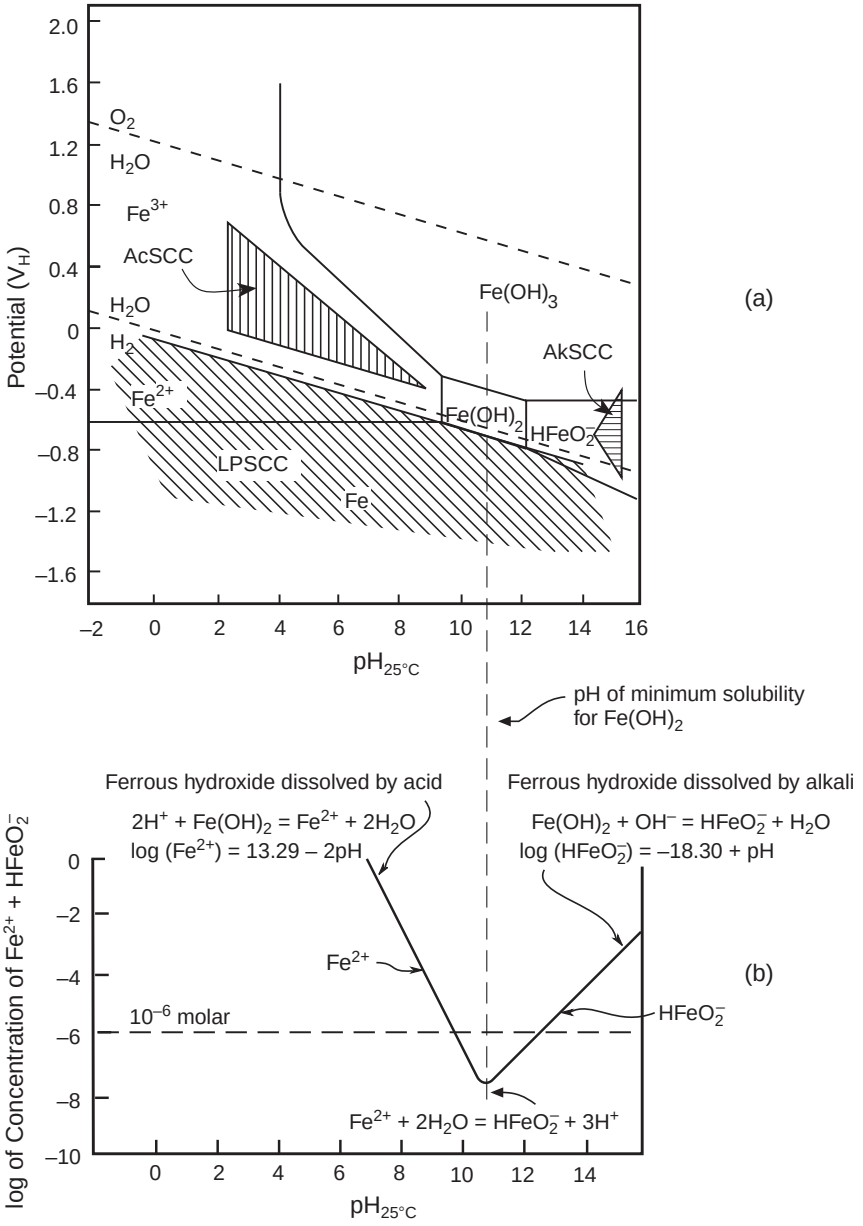

FIGURE 83. *(a) Mode diagram for steel at room temperature based on the work from Congleton, Parkins, and their coworkers.[116-117] (b) Concentration vs pH for the Fe-H_2O equilibria at 25°C. From Pourbaix.[88] Courtesy CEBELCOR, Brussels.*

latter 1970s or thereafter and then the application of Alloy 690TT in replacement steam generators and in new plants, as described in Figure 92.

The chronology of this early development of high-nickel alloy is shown in Figure 92 where laboratory experience is compared with service experience for the submodes of LPSCC and AkSCC. The industry response to the occurrence of these modes of corrosion is given with the same chronology. Essentially, these responses involved lowering stresses, eliminating deep tubesheet crevices, and improving alloys as summarized in Figures 28 and 29. Improvements in water chemistry along the same chronology are shown in Figures 36 and 37.

In addition to Alloy 600MA being used for tubing, this alloy was also used for various structural and welding applications as described in Table 17. In these applications, as in the steam generator tubes, Alloy 600 began to sustain SCC and in most cases LPSCC, since the applications involved the primary environments. While Figure 92 describes the early development of the Alloy 600, 690 group, Table 17 describes the chronology of later SCC in structural materials. Table 17 shows that LPSCC began to occur in CRDMs, pressurizer heater sleeves, tube plugs, instrumentation nozzles, and in the welding material, Alloys 182 and 82, used for attachment welds and buttering. The latter occurrences, as

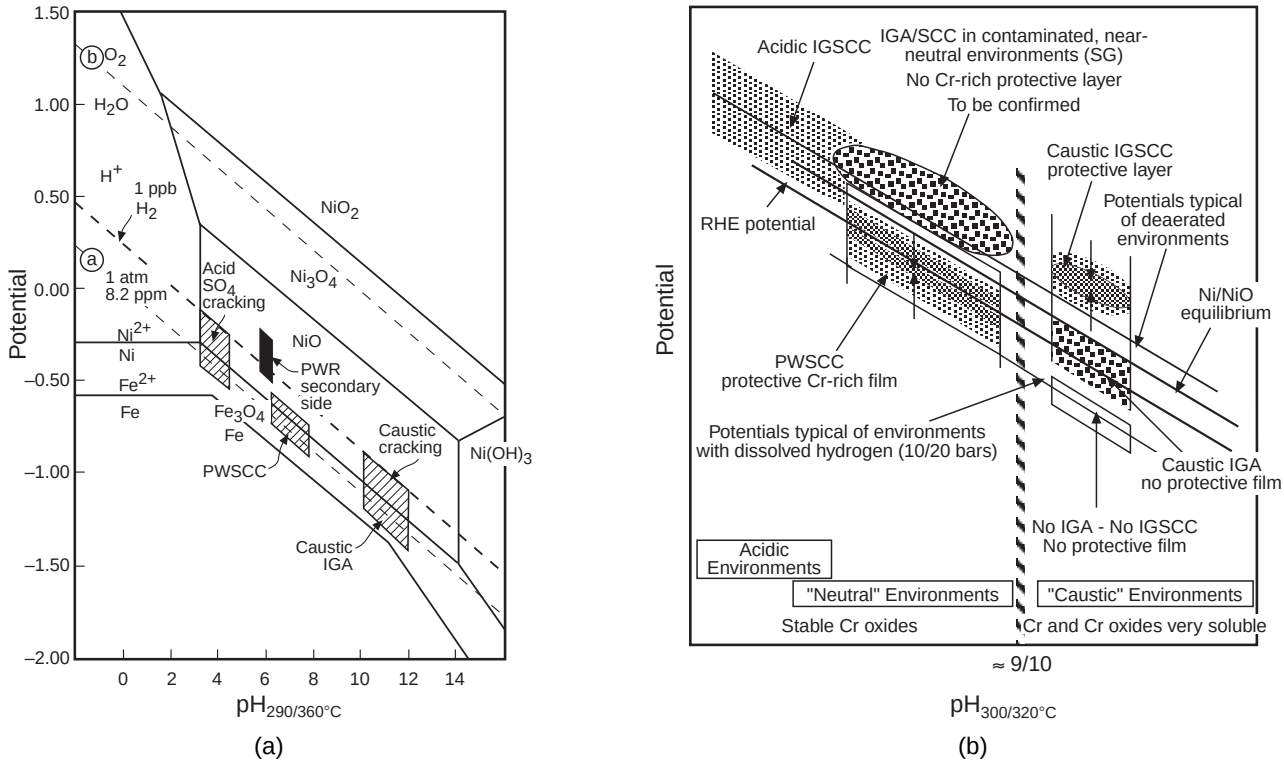

FIGURE 84. *(a) Main domains of IGA and IGSCC of Alloy 600 in aqueous solutions at 290°C/360°C. From Scott and Combrade.[217] ©1997 by the American Nuclear Society, La Grange Park, Illinois. (b) Explanation of important physical processes affecting SCC in terms of protective films and potentials. From Combrade, et al.[218-219] Courtesy of TMS, Warrendale, Pennsylvania.*

shown in Table 17, were quite predictable, even from the early work of Coriou. With the pressurizers, such a result was especially inevitable owing to their higher operating temperatures of about 343°C.

Ultimately, all of the failure modes found by work conducted in laboratories were realized in engineering practice, including SCC seen in the double crevice tests of Copson as manifest in the failure of safe ends of the Duane Arnold plant in 1979.[241] In fact, there was no reason for any fundamental difference in the behavior of tubing and structural applications, which were fabricated from Alloy 600MA; Alloy 600 in both applications is prone to LPSCC. Pressurizer applications sustained early LPSCC because of the higher temperatures at which they operate.

5. Continuity between HPSCC and LPSCC — Work, mostly by Andresen and coworkers,[121,242] has shown that the crack growth rates of Alloy 600 and Type 304 stainless steel in the sensitized condition are similar such that their SCC behavior is indistinguishable in the HPSCC range, as described in connection with the discussion of Figure 127. However, while Alloy 600MA is well known to sustain LPSCC at potentials in the range of the NiO/Ni equilibrium and lower, as described in the discussion of Figure 106, stainless steel does not exhibit such LPSCC except at even lower potentials and then at relatively slow rates.[243] Further, sensitization retards LPSCC of Alloy 600MA as shown in Table 16; whereas, it accelerates SCC of Type 304. The question to be addressed here is whether Alloy 600 and Type 304 behave similarly over both the HPSCC and LPSCC domains and whether, over this broad range, there is, at least, a somewhat monotonic and comparable response of the two materials to potential. The incentive to explore such a relationship is to extend the understanding of Alloy 600MA and similar materials for applications on the secondary side of steam generators.

To assess the possible monotonic relationship of both Alloy 600 and Type 304 stainless steel over the potential range, including HPSCC and LPSCC, Figure 93 compares both materials at the same conditions of pH, potential, and temperature, as extrapolated where necessary. Data at higher potentials in Figure 93 are taken from the dependence of crack growth rates of Alloy 600 and Type 304 in their sensitized conditions from testing conditions in the HPSCC region of water chemistry, as shown in Figure 88(e). These data are compared with data for crack growth rates of Alloy 600MA, taken from Figure 106(c), which are discussed in detail in Section 5.2.2, thereby providing a comparison with the dependence of SCC on potential over the range from HPSCC to LPSCC. The LPSCC data here are compared with the

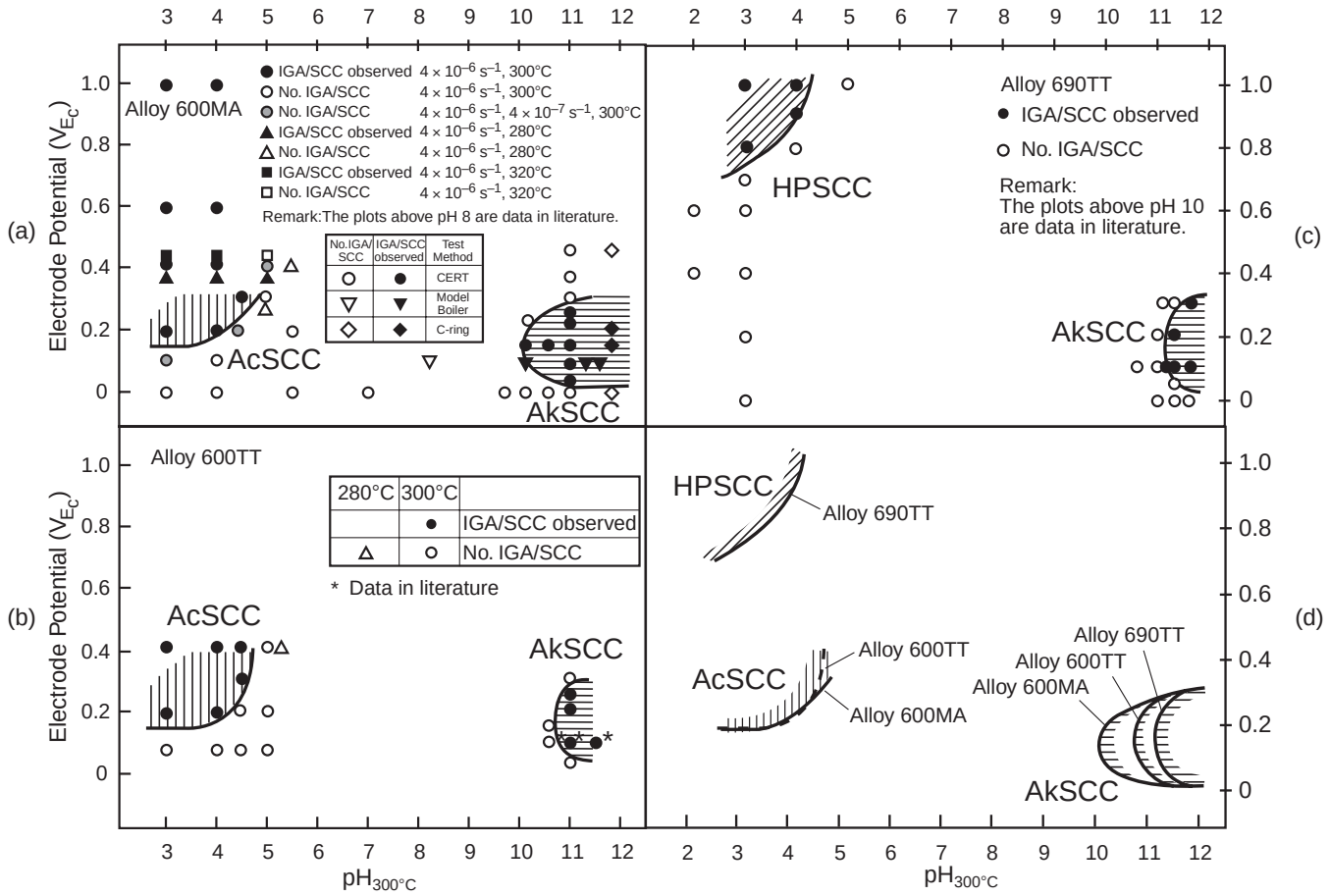

FIGURE 85. *IGA/SCC tests results in the range from 180°C to 320°C range as a function of electrode potential and pH taken at 320°C for: (a) Alloy 600MA, (b) Alloy 600TT, and (c) Alloy 690TT. From Ohsaki, et al.[220] Reproduced with permission of Canadian Nuclear Society. (d) Comparison of IGA susceptibility among Alloy 600MA, Alloy 600TT, and Alloy 690TT in the range of 280°C to 320°C as a function of electrode potential and pH taken at 300°C. From Tsujikawa and Yashima.[221] Reproduced with permission of Canadian Nuclear Society.*

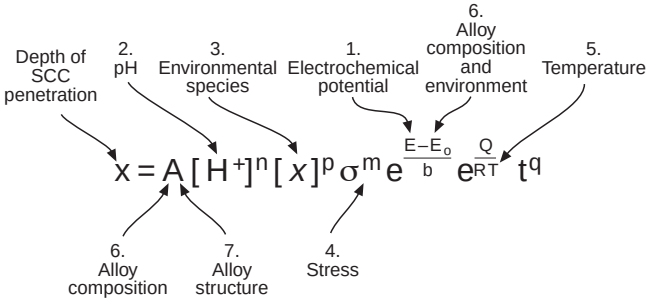

FIGURE 86. *General relationship for the penetration of SCC following commonly accepted dependencies. Locations where principal variables enter this equation are noted.*

HPSCC data by reducing the temperature of the LPSCC data to 288°C using a Q = 30 kcal/mol and adjusting the pH to boiling water reactor (BWR) conditions parallel to the standard hydrogen half cell.

In Figure 93, it should be noted that –240 mV at BWR hydrogen water chemistry and 288°C is taken as the minimum value below which sensitized Type 304 does not sustain HPSCC. Also, the work of Shoji[248] discussed in connection with Figure 128 shows that the onset of SCC for Alloy 600MA in the HPSCC range occurs at significantly higher potentials than for sensitized Alloy 600MA. From Figure 93, it is clear that HPSCC and LPSCC are different processes and that there is no integrated monotonic behavior.

Smialowska, et al.,[249] investigated the dependence of LPSCC and HPSCC and showed that there is about a 200+ mV gap between LPSCC and HPSCC, although they did not extend their work in the HPSCC range beyond a single data point. Smialowska's data are shown in Table 22.[249]

6. SCC of SG Vessel — While this discussion is concerned primarily with the SG secondary side and with SG tubing, other indications of SCC have occurred on the secondary side in the low-alloy steel of SG vessels.[250] This SCC seemed to be associated with the following: low postweld heat treatment tempera-

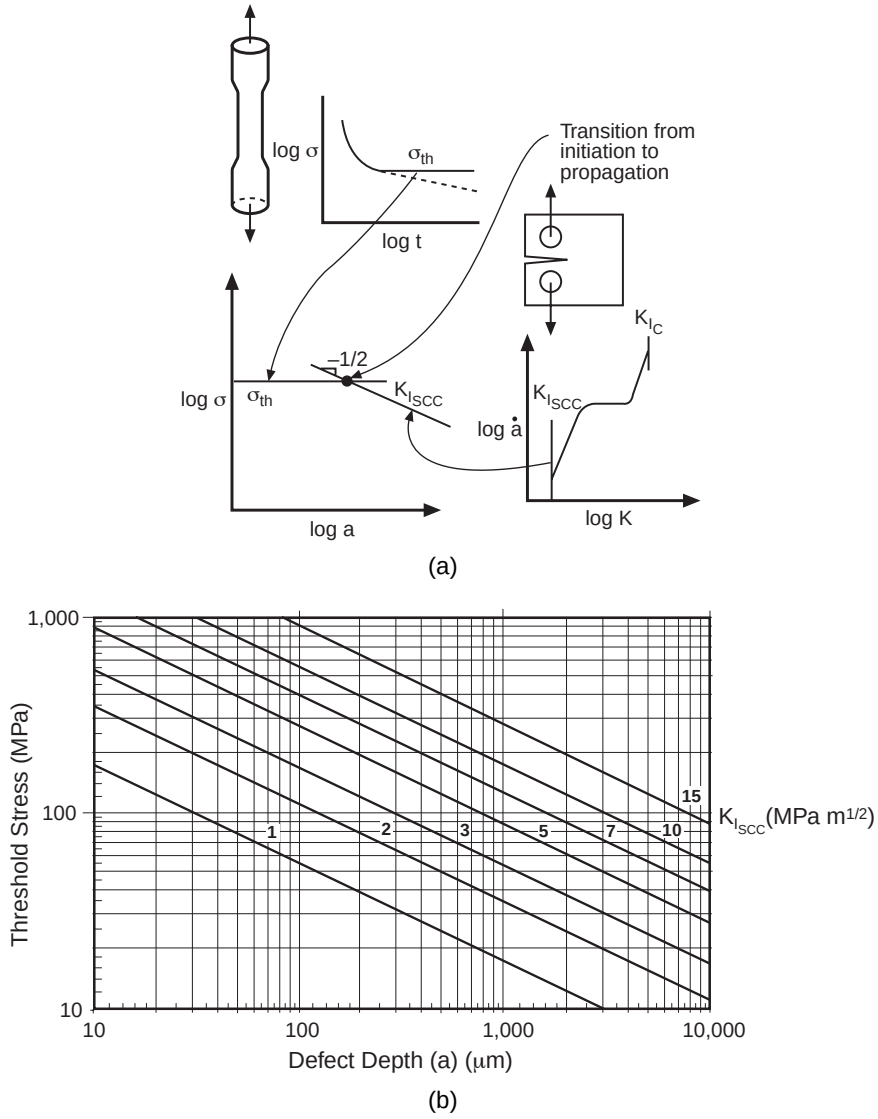

FIGURE 87. *Basis for distinguishing between initiation and propagation. (a) Schematic view of log stress vs log of defect depth for cases of stresses on smooth surface specimens and the locus of points associated with K_{ISCC} as determined from pre-cracked specimens. (b) Log of stress vs log of defect depth for determining the intersection of threshold stresses from smooth surface specimens with values of K_{ISCC}. From Staehle.*[224]

ture, excess cold work, and oxygen contamination during shutdowns and available Cu. The SCC was found to initiate at pits, and these pits seemed to be necessary precursors to SCC. This topic is not discussed here, but it emphasizes the importance of maintaining good water chemistry, including during shutdowns. Such water chemistry affects SCC not only in the vessel but also in the heat-transfer crevices as oxygen is stored in dissolved Cu^{2+} and Fe^{3+} for later reduction.

7. Statistical Behavior of SCC — The initiation and propagation of SCC as well as all forms of corrosion can be correlated using statistical distributions. The correlation of SCC failures from SGs using statistical distributions was first discussed by Staehle, et al.,[21] and Stavropoulos, et al.[74] Staehle has analyzed an extensive set of statistical evaluations of corrosion data with the goal of developing a method for predicting the earliest failure.[61] The statistical analysis of tube failures in steam generators is now widely applied, as shown in Figure 24. Based on these extrapolations the owners can determine when a new steam generator should be purchased, or they can evaluate tradeoffs such as lowering temperature or adjusting water chemistry.

Samples of correlations for LPSCC from the primary side and ODSCC from the secondary side are shown in Figures 94(a) and (b), where the Weibull cumulative distributions use a two parameter fit. On both primary and secondary sides, the Weibull β tends to be in the range of four to six. These results have changed somewhat using three parameter fits.

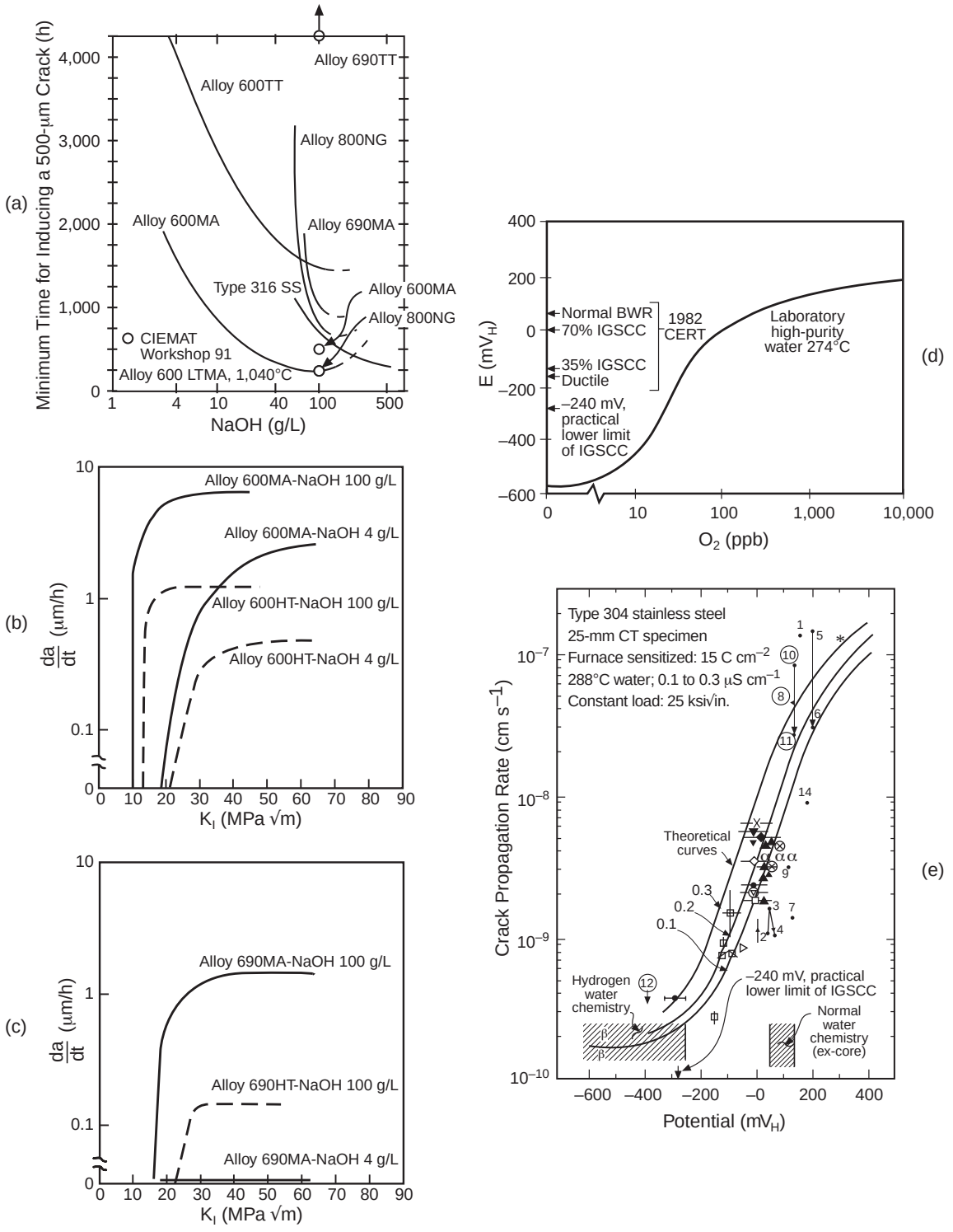

FIGURE 88. *(a) Minimum time for inducing a crack in a smooth surface specimen vs concentration of NaOH for various Fe-Cr-Ni alloys. Specimens are C-rings stressed to approximately the yield stress. The original curves of Berge and Donati[212] were redrawn, and data were added by McIlree (Courtesy of A.R. McIlree of EPRI, Houston, TX, November 1999. Private communication.). Data points added by McIlree were C-rings with 2% strain tested at 10% NaOH. Testing at 350°C. ©1981 by the American Nuclear Society, La Grange Park, Illinois. (b) and (c) da/dt vs K for Alloys 600 and 690 exposed to various concentrations of NaOH at 350°C with a wedge opening loading (WOL)-type specimen. HT corresponds to 700°C for 16 h. From Berge and Donati.[212] ©1981 by the American Nuclear Society, La Grange Park, Illinois. (d) Potential vs oxygen concentration for sensitized stainless steel in pure water showing dependence of open-circuit potential on oxygen and the dependence of SCC of smooth surface specimens on potential tested by CERT. From Indig and McIlree.[225] (e) Crack propagation rate vs corrosion potential for sensitized Type 304 stainless steel using CT specimens at constant load with water conductivity in the range of 0.1 μS/cm to 0.3 μS/cm. From Ford and Andresen.[226] Courtesy of Marcel Dekker Inc.*

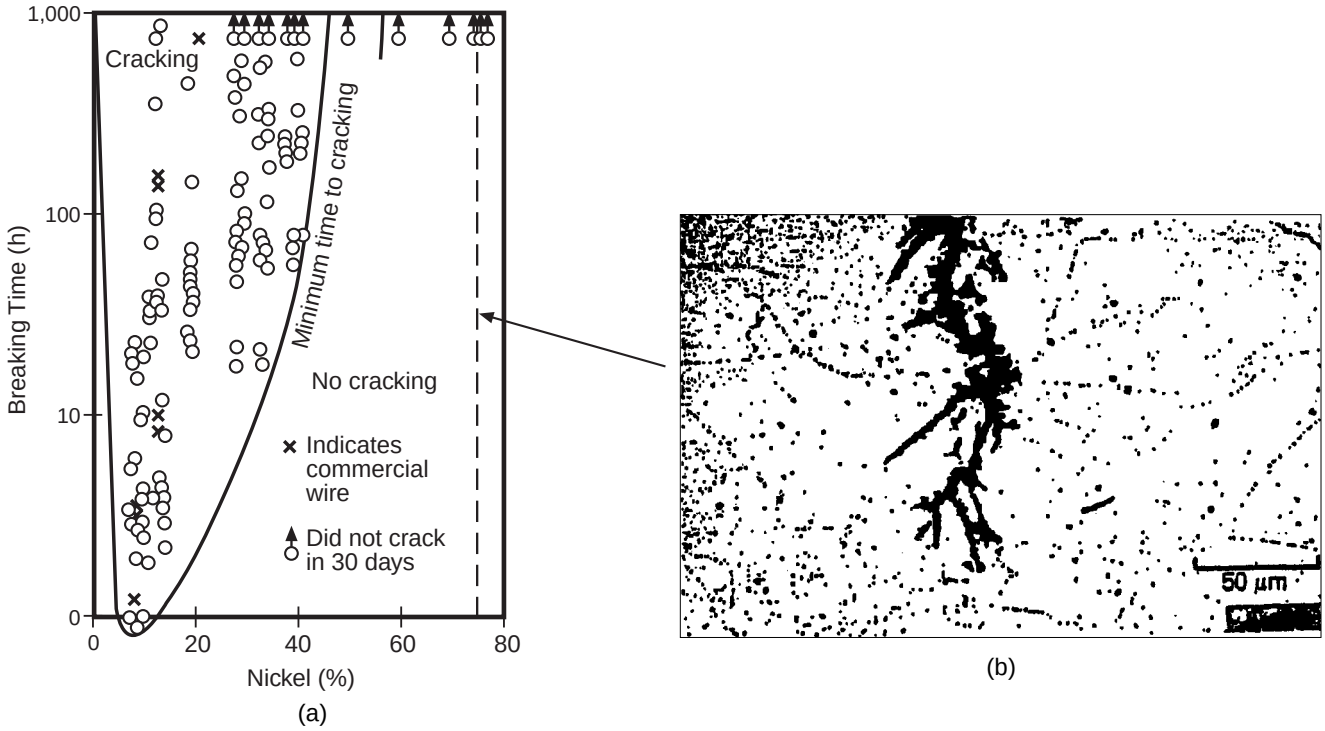

FIGURE 89. *(a) Breaking time vs Ni in w/o for Fe-20Cr-Ni alloys exposed to 42% boiling $MgCl_2$. pH of solution is about 4.1. From Copson and Chen.[227-228] ©1957 NACE International. (b) Photomicrograph of Alloy 600MA exposed at 100°C in a solution containing 50 g/L boron in H_3BO_4 and 2 g/L Cl^-. pH of solution is 2.0 to 2.3. U-bend specimen examined after 800 h. From Berge and Donati.[212] ©1981 by the American Nuclear Society, La Grange Park, Illinois.*

Laboratory testing performed by Norring, et al.,[251] as shown in Figure 94(c), was conducted in LPSCC conditions at 365°C. The individual plots for the data exhibited, like those that are in service, a Weibull β in the range from 1.7 to 7.1 and mainly in the same range as the field data in Figures 94(a) and (b). The data in Figure 94(c) were also aggregated since they were the same alloy in the same environment; the aggregate value of β is 1.5, which is typical of the result of aggregating sets of similar data with different values of θ.

Figure 24 shows Weibull correlations for a set of mode-location cases of tube failure. Figure 21 shows an array of mode-location cases of corrosion that have been observed in various steam generators over time. Here, it is possible to identify the various locations and modes by which failures occur. Also, in Figure 24, the failure rate of all mode-location cases are aggregated, and a total, $F_T(t)$, cumulative distribution of failures is calculated. It is this aggregate curve that is used to determine when the steam generator can no longer continue in service; i.e., this line is extrapolated to a fraction of tubes failed that is considered by the operators to be the condition of failure at which replacement is required. In the case of Figure 24, a fraction of 0.1 of the tubes would have failed after about 21 EFPY (equivalent full power years).

Such statistical analyses, as shown in Figures 24 and 94, are widely used in the nuclear industry to predict the course of corrosion-related failures.

5.2 Submodes of SCC

The purposes of Section 5.2 are: (a) to describe each of the submodes of SCC with their context, as shown in Figure 82, and their estimated respective importance to producing failures on the secondary side; and (b) to describe the extent to which submodes can be characterized by the seven principal variables—pH, potential, species, alloy composition, alloy structure, temperature, and stress—as shown in Figure 86.

Emphasis is placed on the SCC submodes; the dependencies of IGC are discussed but there are not extensive data. SCC is emphasized since it is, in the form of its various submodes, the most extensively observed and most aggressive mode of corrosion in SGs. Other modes such as pitting and GC are discussed briefly; but, in recent years with high-purity secondary water, these have not generally produced significant failures.

5.2.1 Alkaline SCC (AkSCC), Including Alumino-Silicates — AkSCC and AkIGC were the first submodes to be observed in modern operating plants with Alloy 600 tubing in about 1970, as identified in Figure 92, on the OD of tubes of operating plants as

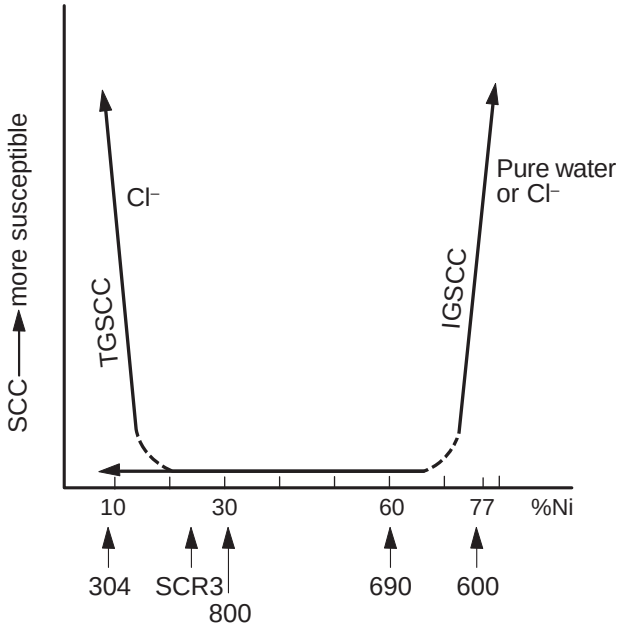

FIGURE 90. *Schematic view of SCC intensity vs Ni concentration for Fe-Cr-Ni alloys in high-temperature water for pure water and chloride-containing water. Important commercial alloys noted. From Coriou, et al.[233] ©1969 NACE International.*

discussed in Sections 3.4 and 3.5.3. Since that time, AkSCC/AkIGC have become less important as phosphate water chemistry was discontinued and as the purity of secondary water has been improved. Now, it is widely considered that the pH inside heat-transfer crevices is in the mid-range, as shown in Figures 53(a) and (b). Later modes of SCC are illustrated in Figure 82 and are discussed in Section 5.2.

AkSCC has been studied extensively, and the primary variables of this submode, together with LPSCC, are the best quantified of the submodes shown in Figure 82. Generally, AkSCC seems prototypic of the anodic submodes in terms of its symmetric bell-shaped dependence upon potential, its propinquity to an IGC region, and the fact that its intensity varies regularly with pH. Further, the rate of AkSCC decreases as the minimum solubility of NiO is approached, as shown in Figures 38 and 46. A similar pattern is shown for the SCC of steels in Figure 83.

Details of a mechanism for the AkSCC submode have not been substantially developed except for a proposal by Scott and Combrade,[140,217] who have suggested a variation of a film rupture process that is similar to the film rupture model of Forty and Humble,[252] where the brittle film is proposed to be one that is depleted of Cr according to its high solubility in alkaline solutions. No available model accounts for the dependency of AkSCC on the seven primary variables.

The alumino-silicate submode, ASSCC, identified in Figure 82(b), is included in the discussion of AkSCC since the former seems to be a variation on the theme of AkSCC. Aggregating ASSCC with AkSCC is similar to the approach of aggregating AcSCC, ClSCC, and CuSCC, which are shown in Figures 82(a) and (b), in Section 5.2.3. ASSCC, as a possible submode of SCC, is based on the extensive work of Sala and coworkers,[164-165,253-256] who have noted that

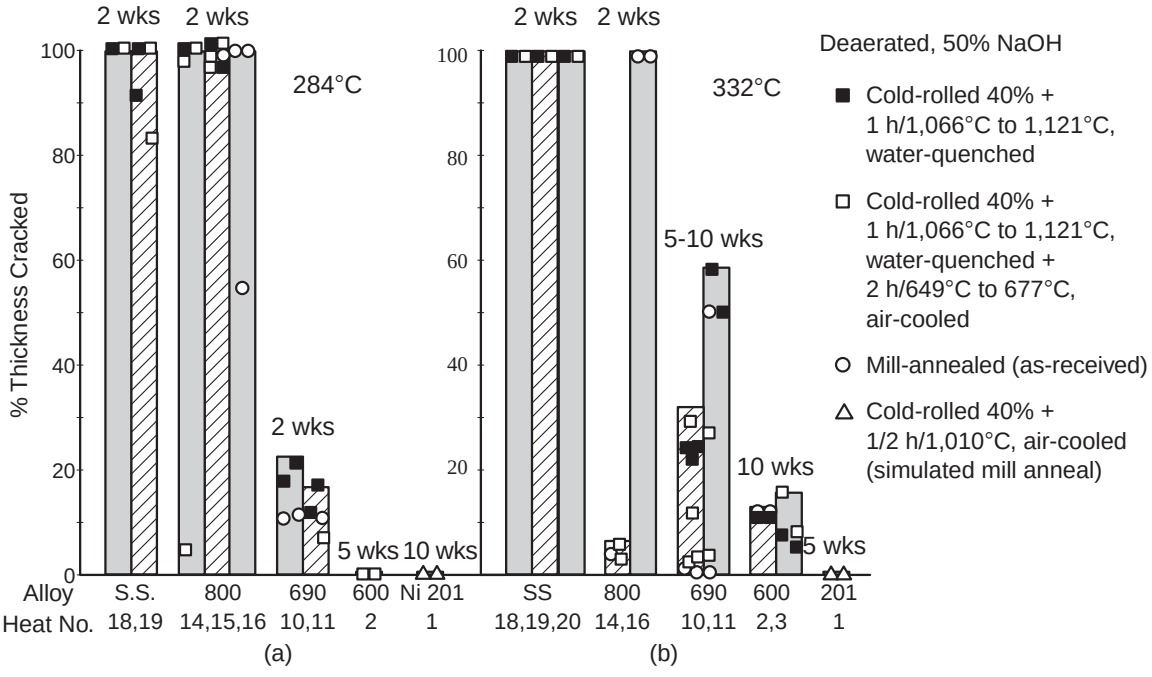

FIGURE 91. *Percent thickness cracked for U-bend specimens of various alloys with different heat treatments exposed in deaerated 50% NaOH at 284°C and 332°C. From McIlree and Michels.[238] ©1974 NACE International.*

TABLE 15

Effect of Oxygen Concentration, Heat Treatment, and Metallurgical Processing on SCC of Double U-Bend Specimens of Alloy 600 Exposed to 316°C Water[A]

Maximum Depth in Mils of Cracks in Crevice Area of Each Double U-Bend Specimen, With Gas Phase Above Solution as Indicated												
Heat[B]	Hydrogen		Argon		1% Oxygen 99% Nitrogen		5% Oxygen 95% Nitrogen		Air		Oxygen	
2–M	0	0	0	0	0	0	0	0	50	55	44[4]	55[4]
–CR	—	—	0	0	0	0	0	0	60[14]	104[16]	32[2]	36[4]
–A	0	0	0	0	0	0	0	0	0	—	21[4]	44[4]
–S	0	0	0	0	0	0	55	100[14]	70[2]	—	55[2]	60[2]
–P	—	—	[D]	[D]	(2)	[D]	80[12]	110[12]	60[2]	85[2]	110[2]	115[2]
–T	—	—	0	0	0	0	0	0	18	60[14]	16[4]	22[4]
4–M	—	—	[E]	0	0	0	0	23	30	35	43[4]	77[8]
–S	—	—	—	—	—	—	—	—	80[2]	80[8]	—	—
5–M	0	0	—	—	0	0	0	80[4]	80[8]	80[10]	61[8]	115[4]
–A	0	0	—	—	0	0	0	0	40	63[18]	26[8]	33[8]
–S	0	0	—	—	0	0	100[4]	110[4]	60[4]	110[10]	115[2]	115[2]
6–M	—	—	—	—	0	0	6	40	40[12]	60[12]	60[8]	60[8]
7–M	0	0	—	—	0	0	38	45	60[16]	80	17[8]	28[8]
–S	—	—	—	—	—	—	—	—	50[6]	100[6]	—	—
8–M	0	0	—	—	0	0	0	19	0	27	9[8]	59[8]
–S	—	—	—	—	—	—	—	—	60[4]	100[10]	—	—

[A] From Copson and Economy.[230] ©1968 NACE International.
[B] Heat treatments: M = mill-annealed; CR = M+cold-rolled 40%; A = 1 h, 1,121°C, WQ; S = A+2 h, 677°C, AC; P = S+24 h in 15%HNO_3+5%HF, RT; T = CR+40 min., 899°C, AC. pH at start-up, 10 (adjusted with NH_4OH); temperature: 316°C; duration of test: 18 weeks or 3,024 h, except as noted.[C]
[C] Numbers in parentheses indicate weeks if less than 18 weeks.
[D] Intergranular attack occurred during pickling to a depth of about 3 mils. This deepened somewhat during the test.
[E] One local penetration a few mils deep was found, but this may have been a surface defect present at start of tests.

most of the ODSCC examined from the secondary side is associated with deposits of alumino-silicates (Table 10 and Figures 59 through 65). While there is good agreement on the general dependencies of AkSCC on the primary variables as discussed in Section 5.2.1, there are apparent differences in the part of AkSCC that relates to alumino-silicates as well as to complex environments as follows:

1. Sala and coworkers[164-165,253-256] have identified clear correlations between the occurrence of ODSCC and the presence of alumino-silicates as identified in Figures 59 through 65.
2. The study of Lancha, et al.,[170] on removed tubes shown in Figure 66 seems to show the opposite of the work of Sala, although possible reasons for the discrepancies have not been explored.
3. The work of Baum, Prabhu, and coworkers,[160-161] shown in Figure 57(a), suggests that higher incidence of ODSCC is related to lower concentrations of SiO_2 in the blowdown. They suggest that this indicates that silica is functioning as an inhibitor and that the absence of this inhibitor permits more SCC. Parenthetically, this is similar to the action of silica proposed in Section 5.2.5. However, their observed lowering of SiO_2 in the blowdown could be caused by the sequestering of SiO_2 in the heated crevices as shown in Figures 67 and 68. By itself, the observation associated with Figure 57(a) does not prove an inhibitive role for SiO_2 any more than the findings of Sala prove a causative role for alumino-silicates. Prabhu[161] has summarized the important work concerning effects of silica in a comprehensive table.
4. Navas, et al.,[162] have shown in Figure 57(b) that silicates inhibit AkSCC significantly over a range of potentials in the presence and absence of chloride and sulfate impurities. These data would confirm the speculation of Baum and Prabhu associated with Figure 57(a) if the causative environment were AkSCC; however, AkSCC has not been important since the 1980s.
5. Bergen[163] has studied the AkSCC of Alloy 600 and Alloy 690 in the as-received condition over a range of concentrations in the system H_2O+Na_2O+SiO_2 at 325°C, as shown in Figures 57(c) and (d). He shows that AkSCC is inhibited at some concentrations but accelerated at others and that both Alloys 600 and 690 re-

TABLE 16

Effect of Heat Treatment and Fabrication on Failure at 350°C in Demineralized and Deoxygenated Water[A]

	Alloy A Alloy 600, C = 0.063 w/o			Alloy B Alloy 600, C = 0.040 w/o			Alloy C Cr 17%, Ni 77% C = 0.02 w/o	
Metallurgical Condition	**As-Received**	**As-Quenched**	**Sensitized**	**As-Received**	**As-Quenched**	**Sensitized**	**As-Received**	**Sensitized**
Determination σ_{max} at the outer fiber at 20°C (kg/mm^2) (±15%)	72	36	72	43	29	43	41	41
Samples cracked after:								
750 h	0/6	0/3	0/3	0/3	0/2	0/2	6/7	0/5
1,500 h	6/6	0/3	0/3	0/3	0/2	0/2	7/7	3/5
2,250 h	—	0/3	0/3	1/3	0/2	0/2	—	5/5
3,000 h	—	0/3	0/3	2/3	0/2	0/2	—	—
4,500 h	—	1/3	0/3	2/3	0/2	0/2	—	—
8,250 h	—	1/3	0/3	3/3	0/2	0/2	—	—
10,000 h	—	2/3	0/3	—	1/2	0/2	—	—

[A] From Blanchet, et al.[80] ©1977 NACE International.

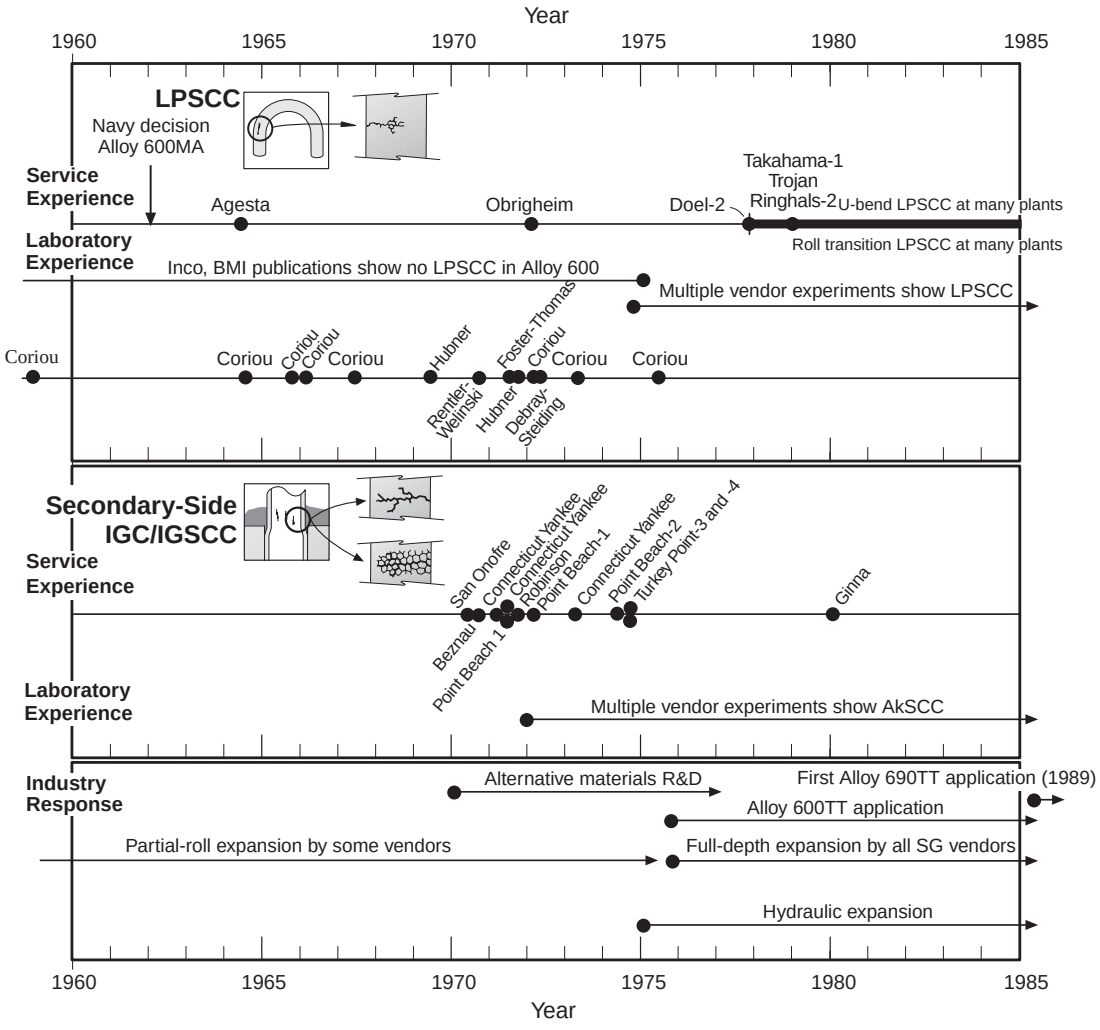

FIGURE 92. *Service and laboratory experience with LPSCC and AkSCC vs time. Industry response to these experiences vs time.*

TABLE 17

Chronology of LPSCC of Alloy 600-Type Materials in PWRs in Non-SG Tube Applications

Plant and Date	Experience
Ågesta, 1964	LPSCC of inspection tubes exposed to 217°C pure water with 1 ppm to 4 ppm LiOH or KOH and minor amounts of oxygen and chlorine.[A]
ANO-2 in 1982, many CE plants since then, continuing to present	LPSCC of pressurizer heater sleeves.[B] First occurred in sleeves with failed heaters, which bulge and apply stresses to the Alloy 600 sleeves. Later, starting about 1989, large-scale failures noted in heater sleeves without failed heaters.
San Onofre-3 in 1986, many CE, B&W, and EDF plants since then, continuing to present	LPSCC of pressurizer instrument nozzles.[B]
Shearon Harris in 1988	LPSCC of rolled-in steam generator head drain nozzle.[B]
North Anna-1 in 1989, many plants of several designs since then, 1989 to early to mid 1990s	LPSCC of Alloy 600TT steam generator tube plugs.[B] These plugs were machined from Alloy 600TT bar stock and mechanically expanded into the tubes.
Bugey-3 in 1989 and many additional plants since then around the world	LPSCC of control rod drive mechanism housings.[B] Cracking increases with time and reactor vessel head temperature. Despite lower temperatures, cracking was seen starting in 1992 at French "cold head" plants.
Palo Verde-2 in 1991, other CE plants up to the present	LPSCC of hot leg RCS instrument nozzle penetrations.[B]
Palisades in 1993	LPSCC of pressurizer relief valve nozzle safe end.[B]
V.C. Summer, 2000	Through-wall LPSCC of Alloy 182 weld metal in hot leg RCS nozzle discovered after about 16 years of service.[C] Similar cracking subsequently detected in Ringhals-3 and -4.
Oconee, 2000. TMI-1, 2001	LPSCC in thermocouple nozzle penetrations discovered after about 27 years of service.[D]
Oconee, 2000	LPSCC in Alloy 182 weld attaching control rod drive mechanisms to reactor vessel head discovered after about 27 years of service.[D]

[A] From Grönwall, et al.[244]
[B] From Hunt and Gross.[245]
[C] From NRC.[246]
[D] From Robinson.[247]

spond similarly to specific compositions of the environments. Thus, his work confirms both the acceleration and inhibition of AkSCC associated with SiO_2. He attributes the results to the roles of various polymers of SiO_2 but does not provide a mechanistic interpretation, although no other investigators provide such explanations either.

6. Vaillant and Stutzmann,[257] in investigating more complex environments, have observed that no SCC occurred with alumina, phosphate, or acetic acid (CH_3COOH) alone. In contrast, an all volatile treatment (AVT) environment containing silica, alumina, phosphate, and acetic acid produced significant SCC, although the same experiment without the alumina and silica produced similar SCC. They conclude that the alumina and silica may not be necessary for SCC. These experiments with more complex environments are difficult to interpret.
7. There is some question as to whether the ASSCC submode or the "complex" environments studied by Vaillant and Stutzmann[257] belong in the AkSCC submode as suggested in the discussion of Table 20 in this section on AkSCC. As additional data are forthcoming, it may be necessary to identify a new submode that is centered about the mid-range of pH. Such a submode also might include data from the discussion of the AcSCC submode shown in Figures 121 and 122, where the data that are the most intense in the acidic region nonetheless extend well beyond the neutral region into the mildly alkaline region. The extent of these submodes may have to be reconsidered in the near future.

It seems that the experiments of Bergen shown in Figures 57(c) and (d) have identified the essence of both the inhibition and acceleration due to at least silica, although the importance of alumina in his experiments was not assessed. While Bergen attributes

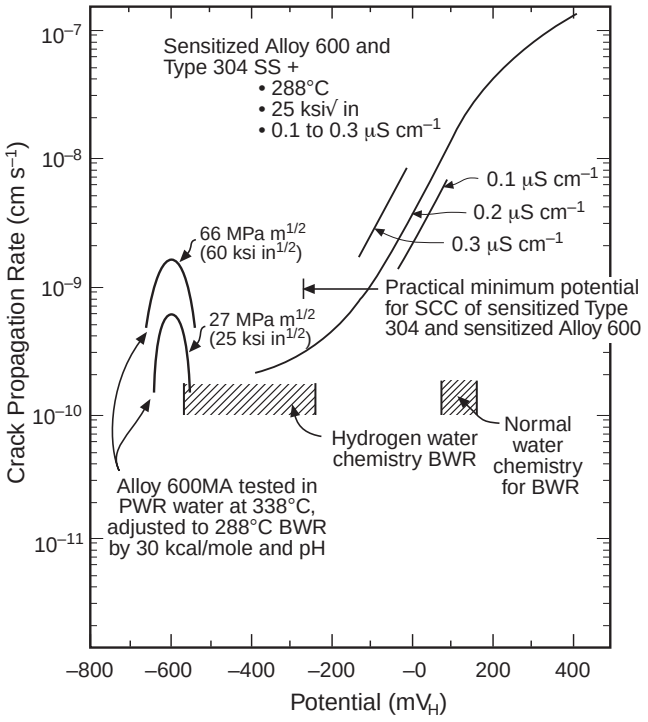

FIGURE 93. *Crack propagation rate vs potential for Type 304 stainless steel and Alloy 600 both in the sensitized conditions at higher potentials and Alloy 600MA at two stress intensities at lower potentials. Data for Alloy 600MA are normalized to BWR conditions using Q = 30 kcal/mol and applying at BWR pH. Data for sensitized materials taken from Figure 88(e)[226] and for Alloy 600MA from Figure 106(c).[304]*

the specific region of compositions where AkSCC is observed to aspects of silica polymers, this speculation requires more attention as well as an integration of the other work in items no. 1 through 6 in this introductory section.

The status of quantitative definition of the primary variables for AkSCC is described as follows:

1. pH

AkSCC decreases in intensity from concentrated solutions to negligible effects around $pH_{300°C}$ of 9 to 9.5, as shown in Figure 82(a); there are some indications, as discussed here, that the lowest pH for AkSCC could be somewhat less. It should be noted, parenthetically, that the submode of AcSCC extends from the acidic range to a pH in the range of 9, as shown schematically in Figure 82(a) and discussed in Section 5.2.3. The dependence of AkSCC for Alloy 600, as well as other alloys, on the concentration of NaOH is shown in Figures 88(a) through (c).

Figure 88(a) shows the minimum time for inducing a 500-μm crack in the various alloys from experiments in 10% NaOH at 350°C using C-rings with 2% strain;[212] and the minimum concentration for AkSCC here seems to be in the range from 0.1 g/L to 1 g/L ($pH_{350°C}$ = 9.7 to 10.3). This figure shows that Alloy 600MA is the most prone to SCC of the alloys including 600MA, 600TT, Type 316 SS, Alloy 800NG, Alloy 690MA, and Alloy 690TT. Data for the plateau crack velocity in NaOH environments is also shown in Figures 88(b) and (c), and the plateau velocities observed follow a pattern of dependence on concentration similar to that for the extent of SCC determined using initially smooth specimens.

Table 18, from Copson, et al.,[239] compares alloys with varying chromium and iron compositions in the sensitized condition in aerated solutions containing high concentrations of 50% and 90% NaOH ($pH_{300°C}$ = 11.3 and 11.8) and indicates that AkSCC is confined to less than 26% to 28% Cr for 50% concentration but that AkSCC continues even to 30% Cr in a 90% NaOH environment.

Copson's intention in Table 18 was to expose Alloy 600 to worst-case conditions: sensitization, aeration, and high concentrations of NaOH. From subsequent investigations, Figure 99(f) shows that sensitization improves the resistance of Alloy 600 to SCC while aeration places the alloy in the general range of the peak intensity of AkSCC according to Figure 97. The results shown in Table 18 are generally consistent with those of Figure 88(a).

Figure 95 shows a combined view of the dependence of AkSCC on potential and pH from the work of Nagano, et al.[123] Figure 95(a) shows a series of polarization curves for different concentrations of NaOH together with the ranges of potential where AkSCC is observed. These data are generally similar to those in Figure 88(a) but show the combined effects of pH and potential. This figure shows that the range of potential that sustains AkSCC narrows as the pH decreases and that the minimum pH for AkSCC is about $pH_{325°C}$ = 10. The occurrence of AkSCC at the locations shown on Figure 95(a) is consistent with Parkins[65,258] and Staehle,[18] who predicted that SCC should occur at unstable transitions of protective oxides. Consistent with the data of Figure 88(a), no AkSCC of Alloy 600MA occurs at 0.04% NaOH.

The minimum pH at which AkSCC occurs is shown in Figure 96 and Table 19. Figure 96 from the work of Kawamura and Hirano[260] identifies the minimum $pH_{350°C}$ for AkSCC as about 9.7. This is generally consistent with the data of Figures 95 and 88(a), although the latter show a somewhat lower minimum pH for the lower bound of AkSCC.

Table 19 shows a series of experiments by McIlree[261] at $pH_{315°C}$ = 8 and 10 as a function of potential. These experiments were undertaken to assess the importance of alumino-silicate additions to alkaline solutions; whereas, the work of Sala and coworkers involved AVT water containing alumino-silicates in connection with the observations summarized in Table 10 and Figures 59 through 66. Much of the elaboration and description of these deposits is the work of Sala and coworkers,[164-166,171] who observed that there was a tendency for the occurrence of SCC

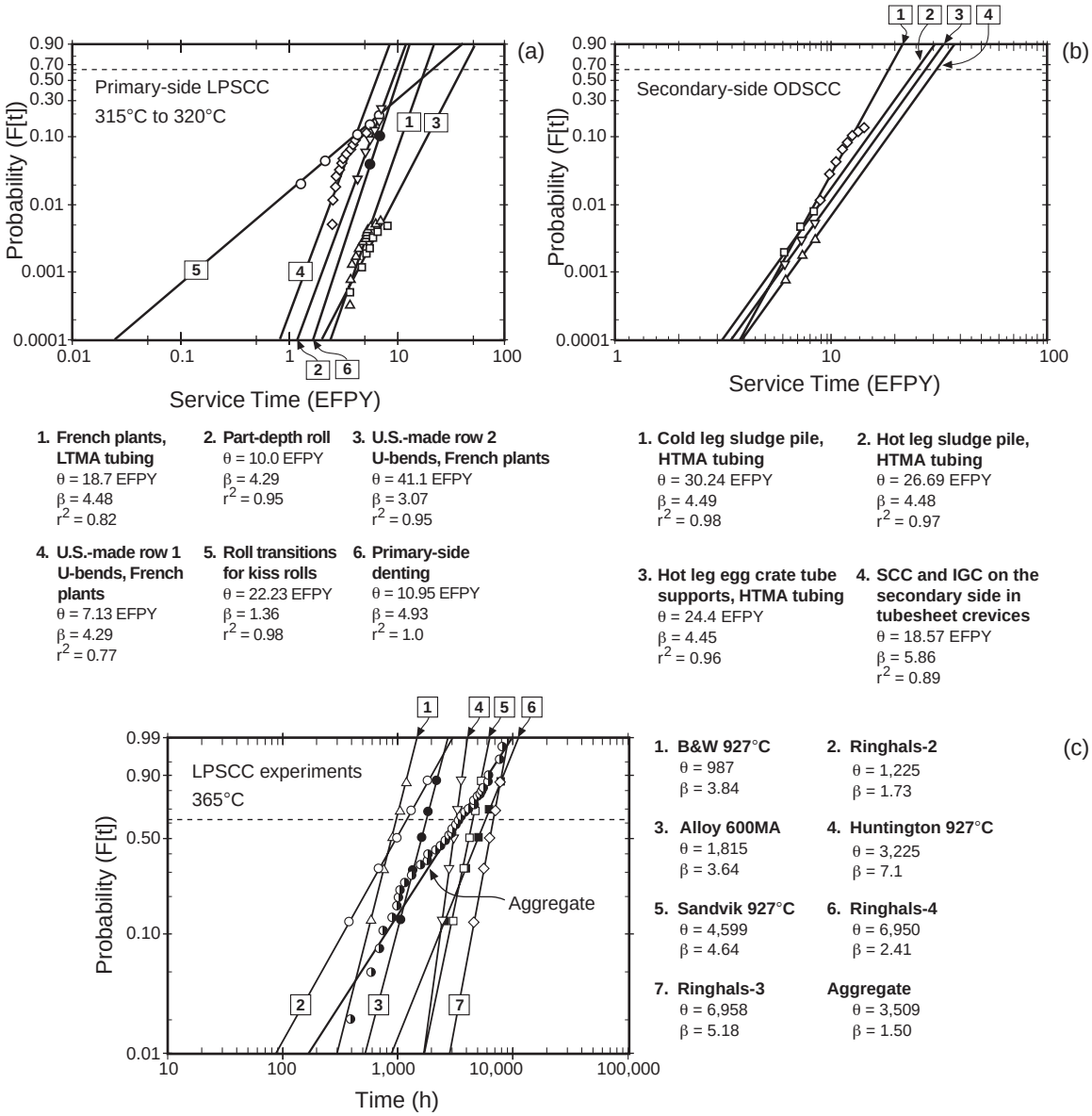

FIGURE 94. *(a) Probability vs service time (EFPY) for the LPSCC occurring on the primary side of tubes from operating SGs in PWRs. Temperatures in the range from 315°C to 320°C. From Staehle, et al.[21] ©1994 NACE International. (b) Probability vs service time for IGA/IGSCC occurring on the secondary side of tubes from operating SGs. SCC occurs at locations of heated crevices at tube supports, tubesheets, and top of the tubesheet sludge piles as shown in Figure 4. From Staehle, et al.[21] ©1994 NACE International. (c) Probability vs service time for seven heats of Alloy 600 exposed to high-purity water at 365°C with hydrogen addition using reverse U-bend specimens where failure occurs by the LPSCC submode. From Norring, et al.[251] Courtesy of TMS, Warrendale, Pennsylvania. (Detailed data not published with curves: for analysis, each distribution was assumed to represent five data points, and the analysis of the aggregate distribution was based on this assumption.)*

and IGC to be associated with extensive deposits of alumino-silicate. However, the data of Table 19 are more consistent with ordinary AkSCC, although the occurrence of SCC at pH_T 8 at 100 mV suggests some effect of the alumino-silicate chemistry relative to the minimum pH for AkSCC observed in Figures 88(a), 95(b), and 96. While the pattern in Table 19 indicates a possible effect of the alumino-silicate additions, the SCC here is more likely a part of the AkSCC submode with a slight extension below the minimum pH indicated in Figure 96, possibly caused by the alumino-silicates or by the high concentrations of dissolved solids and conductivity.

Recently, Vaillant and Stutzmann[257] have shown that complex environments, in the $pH_{320°C}$ range of 4.2 to 9.1, can accelerate SCC; whereas, simple environments with only additions of SiO_2, Al_2O_3, $Ca_3(PO_4)_2$ or CH_3COOH did not, as shown in Table 20. The most aggressive environment was in the liquid phase containing AVT+SiO_2+Al_2O_3+$Ca_3(PO_4)_2$+CH_3COOH+

TABLE 18

Results from Alkaline SCC Tests at 300°C with Various Chromium and Iron Concentrations[A]

Alloy		50% NaOH, 50 psig Air, 27 Days					90% NaOH, 150 psig Air, 7 Days				
				Penetration (mils)					Penetration (mils)		
%Cr	%Fe	Number Specs.	Percent Cracked	Max.	Min.	Avg.	Number Specs.	Percent Cracked	Max.	Min.	Avg.
20	<0.1	2	50	50	0	25	1	100	3	3	3
	6 to 11	2	100	80	4	42	4	100	110	110	110
	>12	4	0	0	0	0	—	—	—	—	—
24	<0.1	2[B]	50[B]	60[B]	0[B]	30[B]	1	0	0	0	0
	6 to 11	2	100	20	5	12	4	100	110	5	84
	>12	4	25	30	0	7	—	—	—	—	—
26	<0.1	—	—	—	—	—	—	—	—	—	—
	6 to 11	—	—	—	—	—	2	50	40	0	20
	>12	—	—	—	—	—	2	100	120	120	120
28	<0.1	2	0	0	0	0	2	0	0	0	0
	6 to 11	6	0	0	0	0	—	—	—	—	—
	>12	2	0	0	0	0	8	75	120	0	65
30	<0.1	2	0	0	0	0	2	0	0	0	0
	6 to 11	—	—	—	—	—	2	100	45	40	43
	>12	6	0	0	0	0	—	—	—	—	—

[A] From Copson, et al.[239] ©1972 NACE International.
[B] 1.6% Fe.

Na_2CO_3 at pH 9.1. While this liquid environment produced 100 μm of penetration in the liquid phase, it produced only 12 μm in the vapor phase. A similar environment but with calcium carbonate ($CaCO_3$) at pH 6.3 exhibited less SCC in liquid but more in the vapor than the one with sodium carbonate (Na_2CO_3). The meaning of these data needs clarification, but they do suggest that additional complexity may alter the underlying trend for NaOH alone. In this regard, the work of Bandy and van Rooyen in Figure 97(b) on AkSCC incorporated carbonate additions to accelerate the AkSCC.[262]

The combined observations of Figures 88(a), 95(b), 96, and Table 19 are the basis for the extent of pH in the mode diagram of Figure 82(a) that defines AkSCC. It appears that alumino-silicate additions produce some acceleration, or extension to lower pH, of AkSCC, although it is not clear whether the alumino-silicate is part of AkSCC, is a different submode, or is part of AcSCC.

2. Potential

The dependence of AkSCC on potential follows generally a bell-shaped curve as implied by the vertical extent of the AkSCC region of the mode diagram in Figure 82(a). Figure 97 shows four sets of results for the effect of potential on AkSCC and each set produces similar patterns being essentially bell-shaped with a peak at about 150 mV to 200 mV above the deaerated open-circuit potential. Figure 97(a) from Suzuki[263] shows that Alloys 600MA and 690TT sustain the same dependence upon potential, with Alloy 690 being less intense overall. This is similar to the data in Figure 85. It is surprising that Alloy 690TT is not more prone to AkSCC and AkIGC in view of both the high solubility of chromium in alkaline solutions as shown in Figures 7(b) and 73 and the 30% Cr in the alloy.

Figure 97(b) from Bandy and van Rooyen[262] shows the locations of regions of AkSCC and AkIGC as compared to the relevant polarization behavior. AkSCC occurs generally at the same location relative to the polarization curve as shown in Figure 95(a). Figure 97(c) from Pessall[264] shows the effects of various heat treatment on AkSCC; these results show that AkSCC depends greatly upon the temperature and duration of thermal treatment but that the general shape of the curve and its peak are the same.

The effect of potential is shown also in Figure 95(b). Here, an additional line is drawn on Figure 95(b) corresponding to the standard hydrogen electrode at 325°C. This line curves slightly, owing to the calculation for pH being slightly different from the concentration. The lower limit of the hatched region in Figure 95(b), indicating AkSCC, is about 200 mV above this standard hydrogen line. The dependencies upon potential and pH of the AkSCC submode of Figure 95 are consistent with the dependencies of potential and pH shown in Figures 88(a), 96, and 97.

Figure 97(d) shows the effect of potential vs the standard hydrogen electrode (SHE) rather than a potential relative to the deaerated open-circuit potential in the other figures. The shape is similar also for an alloy with 50 ppm of boron. The data in this figure were obtained at 4% NaOH; whereas, the others were obtained at 10% NaOH.

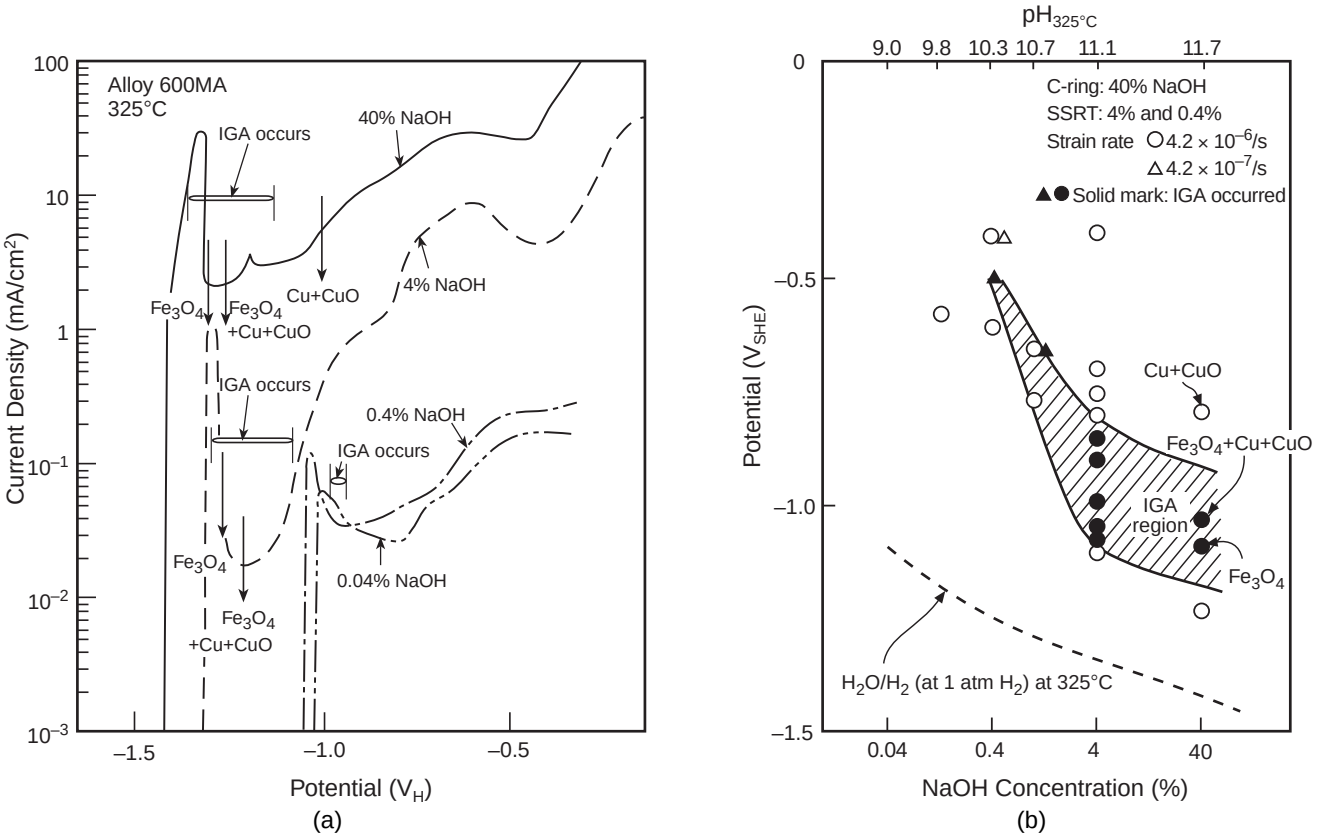

FIGURE 95. *(a) Current density vs potential for Alloy 600MA in alkaline solutions of various compositions at 325°C. Regions of potential for AkSCC are noted. From Yamanaka, et al.[259] (b) Applied potential vs concentration of NaOH for intergranular SCC and IGC, given as IGA, of Alloy 600 at 325°C. NaOH+Fe_3O_4+Cu+CuO added as appropriate to achieve target potential and pH for IGA tests. From Nagano, et al.[123] ©1990 NACE International.*

Figure 97(b) shows data for the SCC of Alloy 600MA in 10% NaOH as a function of potential but only for a range from the corrosion potential to 200 mV. This extent is about the lower 2/3 of the data in other plots in Figure 97. Similar effects of potential are shown in Tables 4 and 19 where effects of inhibitors and alumino-silicates have been examined as a function of potential. These data show the same patterns as in Figure 97.

The dependence on potential exemplified in Figure 97 is common for what is known of other anodic (meaning above the H_2O/H_2 standard half-cell equilibrium) submodes, although they have not been so thoroughly investigated.

The location of the peak rate of SCC as a function of potential for AkSCC is important relative to the location of the H_2O/H_2 equilibrium as shown in Figure 97. For the experiments in Figures 97(a) through (d), the zero of potential is the open-circuit potential in a deaerated solution. This potential may have been lowered depending on whether hydrogen was removed during the experiments. Nonetheless, Figure 97 implies that no, or minimal, AkSCC should be expected in the deaerated state, although Figure 97(b) suggests that some IGC should be expected. This is observed in service even though the causative environment is rarely knowable.

The dependence of AkSCC on potential, as shown in Figure 97, is the main basis for adding N_2H_4 to the secondary side; the addition of N_2H_4 also may reduce the potential with respect to other submodes such as AcSCC or PbSCC, which tend to exhibit the same potential dependence as for AkSCC and for corrosion modes such as pitting and denting. However, if no N_2H_4 were added, higher potentials, in view of the very low hydrogen present on the secondary side, would favor AkSCC because of the effect of the very low hydrogen on the H_2O/H_2 equilibrium potential, as shown in Figure 33. Effects of N_2H_4 on potential are shown in Figures 33 and 45(a). The extensive early AkSCC in several plants is not surprising in view of the patterns of Figure 97. Such a pattern is illustrated also in Figure 40(c).

3. Species

With AkSCC, other species, such as the cations Li and K, have not been investigated extensively for Alloy 600, although they have for AkSCC of stainless and low-alloy steels. AkSCC in Alloy 600 is accelerated by the presence of Na_2CO_3, although the reason is not so clear since carbonate by itself, as shown in

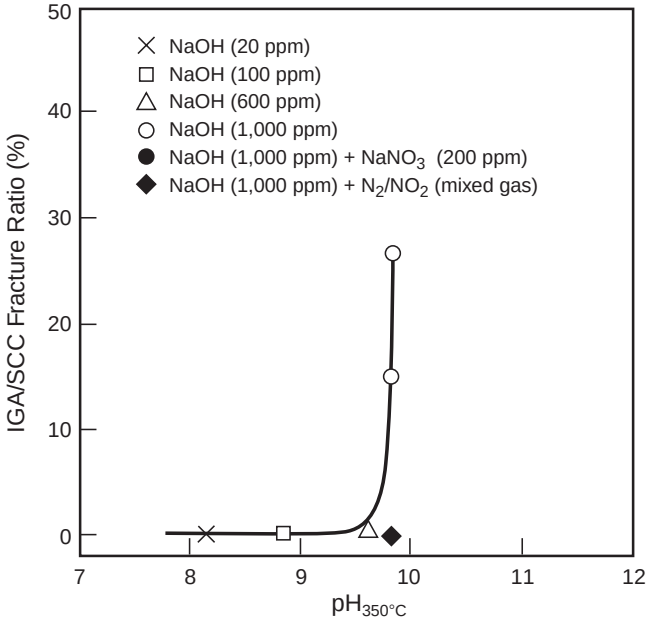

FIGURE 96. *IGA/SCC fracture ratio vs pH for AkSCC of Alloy 600MA at 350°C. From Kawamura and Hirano.[260] Courtesy of TMS, Warrendale, Pennsylvania.*

Tables 20 and 31, does not seem aggressive. Additions of Cu^{2+} also stimulate AkSCC, but this effect is readily interpreted in terms of its effect on electrochemical potential as shown in Figures 40(c) and 97.

Tables 29 through 31 in Sections 5.2.5 and 5.2.6 show effects of various species such as CuO, lead monoxide (PbO), and $Na_2S_2O_3$ added to 10% NaOH. Additions of PbO and $Na_2S_2O_3$ are shown to increase the intensity of SCC, especially for Alloy 690TT; however, these additions are in the category of separate submodes as described in Sections 5.2.5 and 5.2.6.

While the central environmental consideration in Section 5.2.1 is NaOH, effects of other species are important as they affect the occurrence and rate of AkSCC. Aside from other species like Cu^{2+}, N_2H_4, TiO_2, and H_3BO_3, little work has been performed, and these species have been introduced because they either affect the potential or pH or control it. These patterns are well known and are discussed extensively in other sections. Species such as PbO and lower valence sulfur are discussed as parts of separate submodes in Sections 5.2.5 and 5.2.6.

Only species related with the effects of alumino-silicates need to be considered here. Effects of these

TABLE 19
SCC of Alloy 600 in pH 8, 10[(A)] at 315°C Alumino-Silicate[(B)]

		Material; ECP (mV)	600MA Cracked/Tested		600SN Cracked/Tested		600TT Cracked/Tested		690TT Cracked/Tested	
		pH	8	10	8	10	8	10	8	10
Applied Potential	Without Organics	OC	0/1	1/1[(C)]	0/1	1/1[(C)]	0/1	0/1	0/1	0/1
		50	1/1	3/3[(D,F)]	0/1	1/1[(C)]	0/1	0/1	0/1	1/1[(C)]
		100	1/1	2/2[(E,G)]	0/1	0/2	0/1	2/2[(E,G)]	0/1	0/1
		150	0/1	2/3[(E,I)]	0/1	2/5[(E,J)]	0/2	1/2[(E,K)]	0/1	0/1
		375	—	—	—	0/1	—	—	—	—
		400	—	—	—	1/2[(L)]	—	—	—	—
	With Organics[(M)]	425	—	—	—	0/1	—	—	—	—
		–150	No SCC	—	—	—	—	—	—	—
		100	1/1	—	0/1	—	0/2	—	0/2	—
		150	0/1	—	0/2	—	0/2	—	0/2	—

(A) pH 8: 5.0 M NaCl + 0.5 M SiO_2 + 0.5 M K_2SO_4 + 0.12 M KOH + 0.1 M Fe_3O_4 + 0.05 M Al_2O_3
pH 10: 5.0 M NaCl + 0.5 M SiO_2 + 0.5 M K_2SO_4 + 4.0 M KOH + 0.1 M Fe_3O_4 + 0.25 M Al_2O_3
or
5.0 M NaCl + 0.5 M SiO_2 + 0.5 M K_2SO_4 + 5.3 M KOH + 0.1 M Fe_3O_4
**RUB specimens, 2-month test except where noted, alumino-silicate solution.

(B) From McIlree.[261] Licensed material used by permission of EPRI.

(C) SCC not detected by dye penetrant. Deformation of specimen legs required to observe SCC.

(D) Microscope required to detect SCC.

(E) Severe SCC visible to unaided eye.

(F) Three separate tests of 8-, 4-, and 3- (11+1) week durations. 1/1 specimens cracked after each test.

(G) Two separate tests of 4- and 3- (2+1) week durations. 1/1 specimens cracked after 4-week test, 0/1 after 2 weeks in second test, and 1/1 cracked after 1 week.

(6) Two separate tests, each of 8-week duration. 1/1 specimens cracked after 8-week test.

(I) Three separate tests of 4-, 2-, and 1-week durations. 1/1 specimens cracked after 4- and 2-week tests but no crack in 1-week test.

(J) Separate tests of 8 and 12 weeks. 2 and 3 polished specimens cracked at 8 weeks and 1 had no cracks after 12 weeks. 1 nonpolished sample had no cracks after 4 weeks.

(K) Two separate tests, one of 8 (4+4) weeks and one of 12 (4+4+4) weeks. 1/1 cracked at 8 weeks, 0/1 not cracked at 12 weeks.

(L) 1/1 cracked when polarized at 150 mV for 2 weeks and then 400 mV for 4 additional weeks. 1/1 polarized at 400 mV for 4 weeks did not crack.

(M) "Organics" is 10 ppm acetic acid + 100 morpholine.

TABLE 20

General Results of IGA/SCC and Surface Analyses on Alloy 600MA[A]

Test No.	Test Environment	$pH_{320°C}$ MULTEQ	Test Duration (h)	Liquid		Vapor		Deposit	Nonprotective Cr-Rich Layer
				Results	CSC	Results	CSC		
1	R[B] + SiO_2	6.0	2,500	—	NC EP	—	—	Continuous Si	?
3	R + SiO_2 + Al_2O_3	5.9[C]	2,498	NC EP	AR: in progress	—	—	Continuous AlSi	—
4	R + SiO_2 + $Ca_3(PO_4)_2$	5.2	2,500	—	NC EP	—	—	Continuous Si	?
2	R + SiO_2 + CH_3COOH	5.7	2,498	—	NC EP	—	—	Continuous Si	?
5	R + SiO_2 + Al_2O_3 + $Ca_3(PO_4)_2$ + CH_3COOH	5.2[C]	2,500	—	10 μm EP	—	—	Continuous Si	Yes Cr, Si
8	R + SiO_2 + Al_2O_3 + $Ca_3(PO_4)_2$ + CH_3COOH	5.2[C]	3,191	45 μm AR	NC EP	NC AR	—	—	—
7	Item 8 but morpholine instead of R (CH_3COOH[D])	4.2[C]	500 without phosphate +2,500	16 μm AR	NC EP	24 μm AR	Indent. EP	Semi-continuous AlSi	Yes Cr, Si
11	R + SiO_2 + Al_2O_3 + $Ca_3(PO_4)_2$ + CH_3COOH + Na_2CO_3	9.1[C]	2,425	100 μm AR	General corrosion EP	12 μm AR	NC EP	Continuous AlSi	?
10	R + SiO_2 + Al_2O_3 + $Ca_3(PO_4)_2$ + CH_3COOH + Ca_2CO_3	6.3[C]	2,500	30 μm AR	NC EP	28 μm AR	Indent. EP	Continuous AlSi	?
12	R + SiO_2 + Al_2O_3 + $Ca_3(PO_4)_2$ + CH_3COOH + ZnO	6.3[C]	2,260	NC AR	NC EP	—	—	?	?
6	R + SiO_2 + Al_2O_3 + CH_3COOH[D]	4.1[C]	2,500	NC AR	Indent. EP	—	—	Granular Al	Yes Cr, Fe
9	R + $Ca_3(PO_4)_2$ + CH_3COOH	5.2	2,473	25 μm AR	NC EP	45 μm AR	NC EP	No	Yes Fe, Cr

[A] From Vaillant and Stutzman.[257] ©2003 NACE International.
[B] Reference environment: deaerated solution of ammonia (pH_{25} 9.2) + 2 ppm hydrazine.
[C] Al_2O_3 not in MULTEQ database: calculated with Al.
[D] CH_3COOH concentration: 10,000 ppm instead of 10 ppm.

species vary from having a strong effect in producing SCC according to Sala and coworkers,[164-165,253-256] to having no effect as discussed in connection with Table 20, to being inhibitors as suggested in Figures 57(a) and (b) by Baum and Prabhu[160-161] and by Navas, et al.[162] Bergen,[163] in Figures 57(c) and (d), has shown data that suggest both acceleration and inhibition of SCC may occur with Alloys 600 and 690, at least in the as-received condition depending on the relative concentrations of H_2O+Na_2O+SiO_2.

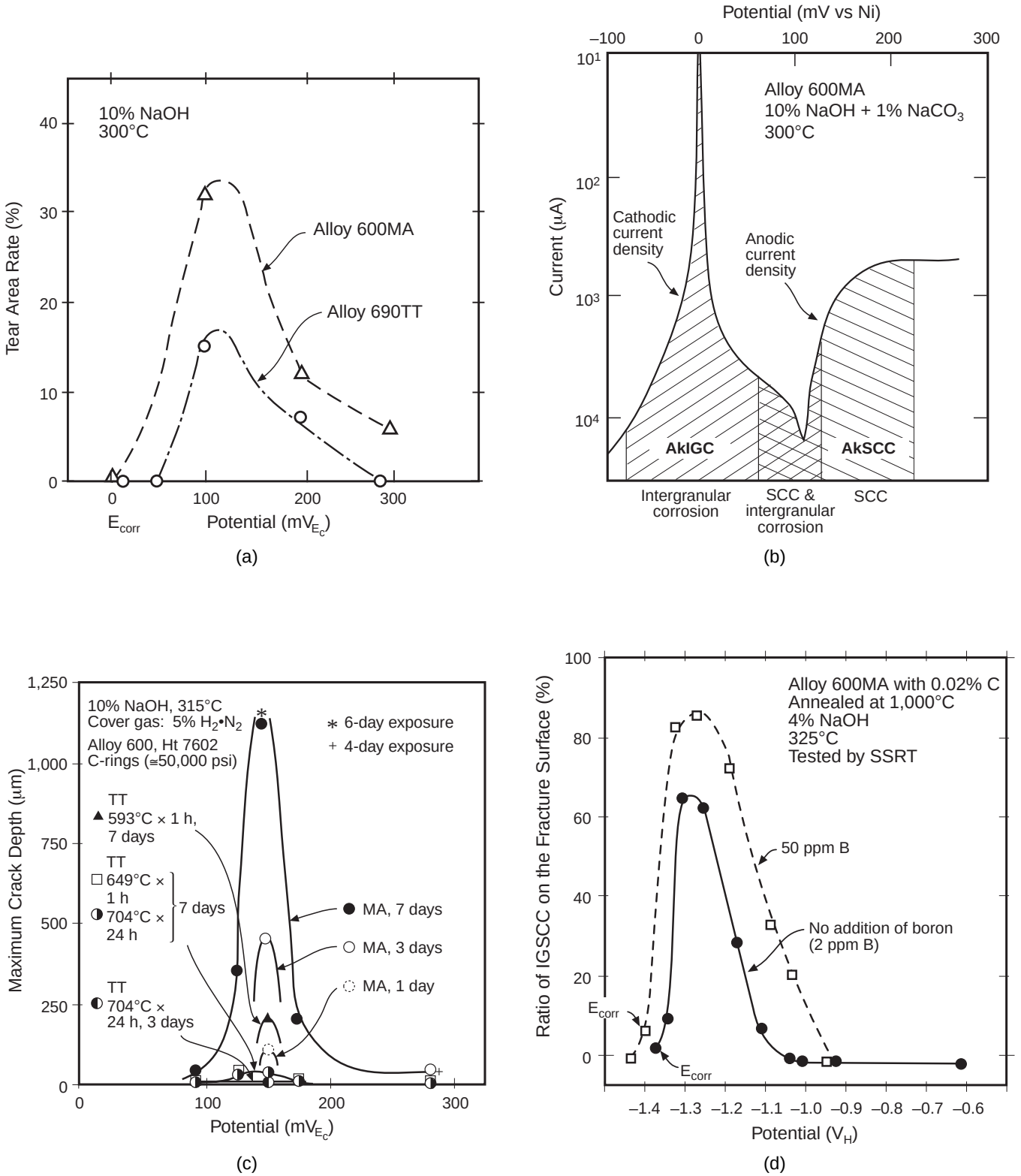

FIGURE 97. *Dependence of AkSCC on applied potential above the deaerated open-circuit potential. (a) Tear area rate (%) for Alloy 600MA and Alloy 690TT at 300°C as a function of potential in a 10% NaOH solution. From Suzuki.[263] ©1991 by the American Nuclear Society, La Grange Park, Illinois. (b) Effect of applied potential on the polarization current and modes of corrosion for Alloy 600 in 10% NaOH+1% $NaCO_3$ at 300°C. From Bandy and van Rooyan.[262] (c) Maximum crack depth vs potential for Alloy 600 exposed in 10% NaOH at 315°C for mill-annealed and various thermal treatments. From Pessall.[264] ©1980 Elsevier Science. (d) Ratio of IGSCC on the fracture surface vs potential for Alloy 600MA in 4% NaOH at 325°C. From Nagano, et al.[123] ©1990 NACE International.*

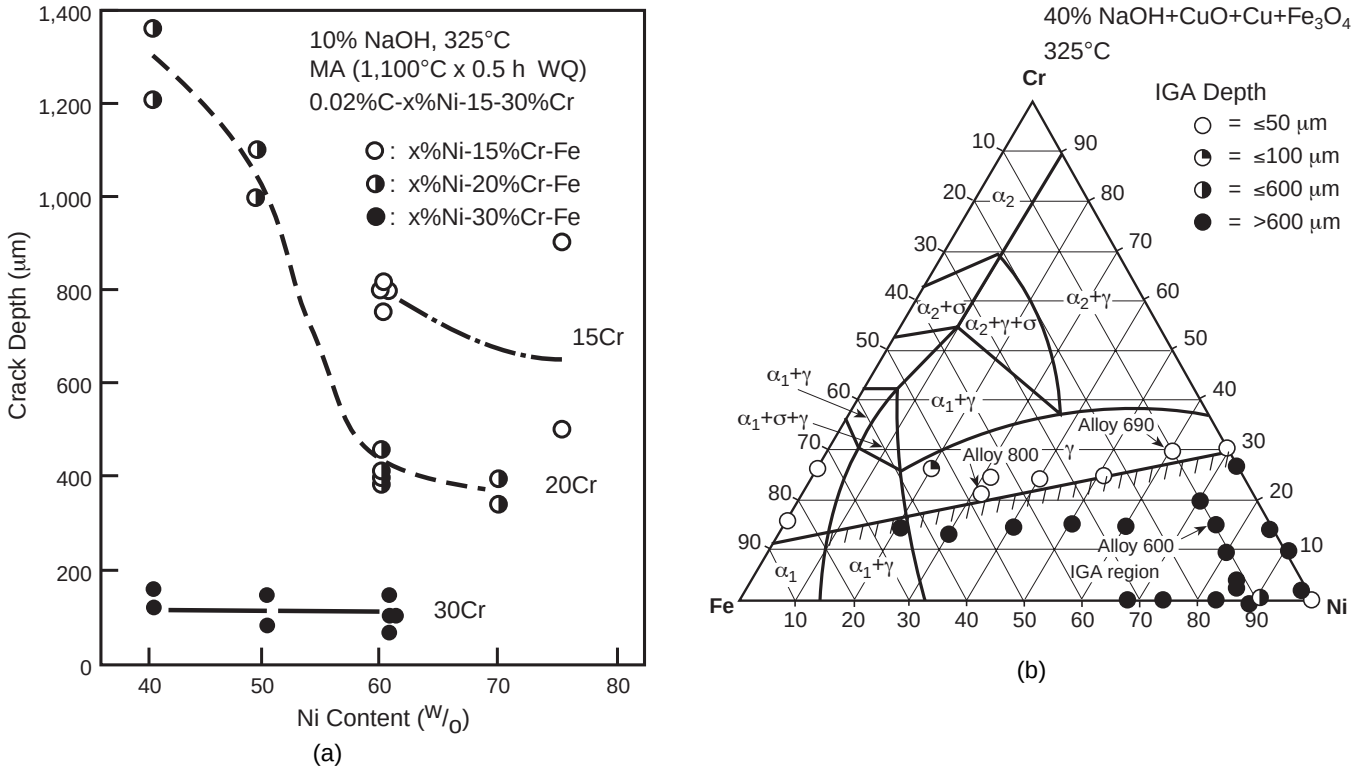

FIGURE 98. *(a) Crack depth vs Ni concentration for Ni-Cr-Fe alloys + 0.02% C exposed in a deaerated 10% NaOH solution at 325°C for 200 h as single U-bends. Specimens were mill-annealed. From Nagano, et al.[266] (b) Effects of alloying elements (Fe, Ni, Cr) on IGA in the solution of 40%NaOH+Fe_3O_4+Cu+CuO at 325°C for 200 h using U-bend specimens. All alloys were mill-annealed. The phase diagram of Fe-Ni-Cr ternary alloys is shown for 400°C and adapted from Pugh and Nisbet.[53] From Yamanaka and Yonezawa.[267]*

The essential observation of Sala and coworkers is that an alumino-silicate layer is associated with the occurrence of ODSCC in SGs. This layer has been shown to lead to a nonprotective layer on the metal that, in turn, promotes the SCC. Sala and coworkers have conducted extensive studies to characterize these layers. However, a specific connection between these layers and the occurrence of ODSCC has not been forthcoming. Nonetheless, the detailed work on these layers has greatly improved the understanding of general surface chemistries and structures that do occur.

The work of Bergen,[163] based on the idea of different polymers of silica being important, may provide a means for differentiating the conditions that promote and retard SCC. Like the work of Sala, Bergen's work lacks specific connection to a detailed explanation for the SCC.

4. Alloy Composition

In general, AkSCC is sustained by Fe-Cr-Ni alloys as shown by Figures 98(a) and (b) over a broad range of compositions but decreases with increasing Cr as shown in Figure 98(a) and Table 18. AkSCC is negligible for pure Ni as shown in Figure 98(b). The Fe, Ni patterns for SCC over most of the range of alloys are related to the active/passive juxtaposition as shown in Figures 95(a) and 7. The decrease of AkSCC with increasing Cr, as with Alloy 690, generally is surprising in view of the high solubility of Cr in alkaline solutions (Figure 73). However, Figure 91 shows that Alloy 690 in all heat treatments that were tested in 50% NaOH were more prone to AkSCC than Alloy 600. Lumsden and Stocker[265] have shown that surfaces of increasingly higher Cr alloys are progressively more enriched in nickel, but this does not seem to translate into greater proneness to SCC.

Figure 88(a) shows that Alloy 600MA is the most prone to AkSCC followed by Alloy 600TT. Alloy 800NG is much less prone, and Alloy 690 exhibits practical resistance, although this result is not consistent with the data in Figures 91 and 97(a). Bergen shows that Alloys 600 and 690 in the as-received form behave about the same at the critical combination of H_2O+Na_2O+SiO_2, which produces AkSCC. Further, in view of the high solubility of Cr in alkaline solutions, as shown in Figures 7 and 73, it is surprising that Alloy 690 is not substantially more prone to AkSCC than Alloy 600. However, the data from Table 20 show that Alloy 690TT was not prone to SCC in any of the complex environments in contrast to the results of Bergen in Figures 57(c) and (d),[163] although this comparison is not comparable in detail.

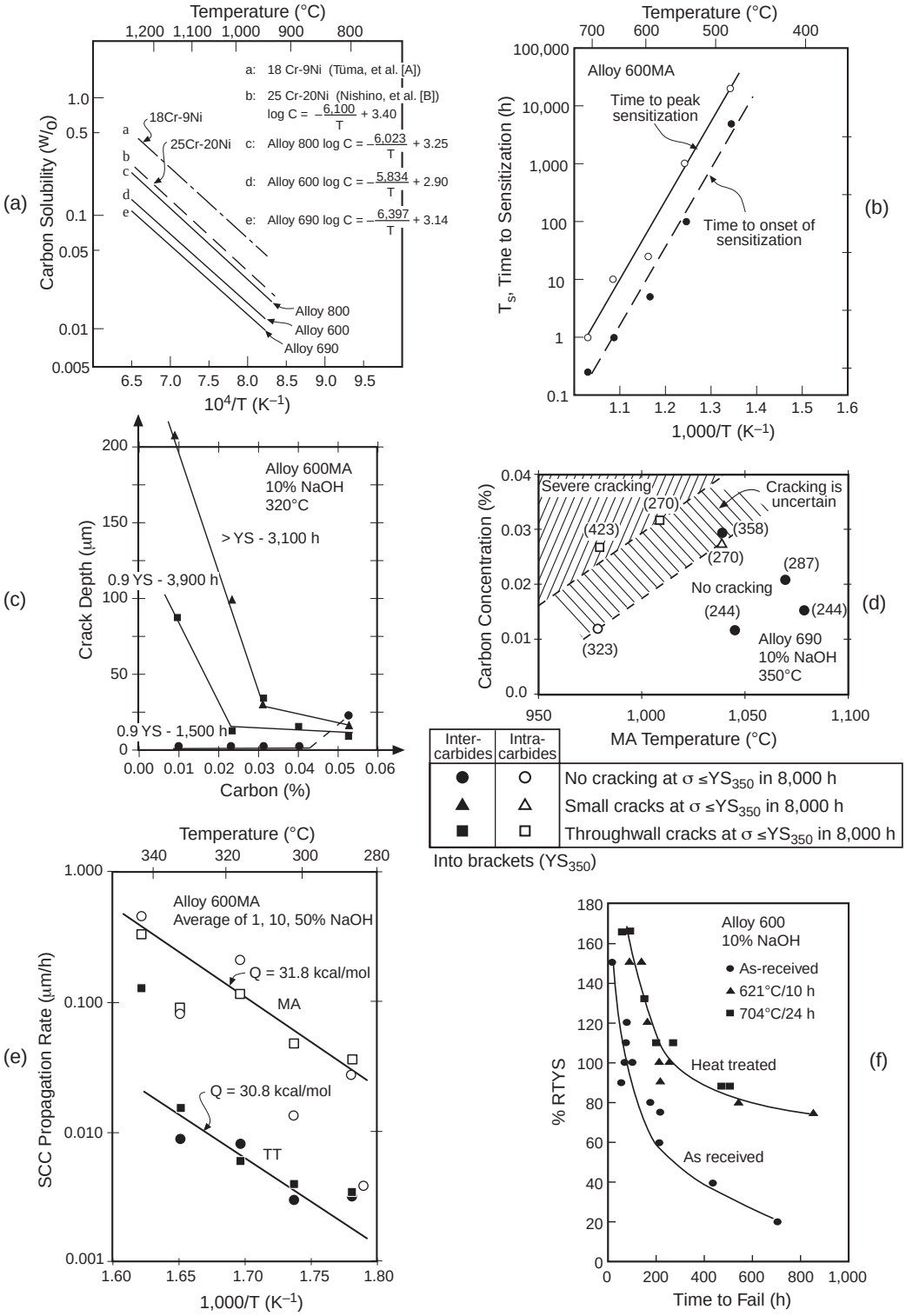

FIGURE 99. *(a) Relationship between carbon solubility and 1/T for various alloys including Alloy 600 and Alloy 690. From Yamanaka and Yonezawa,[267] including data from [A] Tuma, et al., and [B] Nishimo, et al. Refer to Yamanaka and Yonezawa[267] for Tuma and Nishimo references. (b) Time-to-peak sensitization (open symbols) and time-to-onset of sensitization (solid symbols) as a function of temperature for Alloy 600MA. From Airey.[275] ©1985 NACE International. (c) Crack depth as a function of carbon concentration of Alloy 600MA (10% NaOH, 320°C). From Vaillant, et al.[271] ©1996 NACE International. (d) IGSCC sensitivity of TT (700°C) Alloy 690 vs MA temperature and C content in 10% NaOH, 350°C. From Vaillant, et al.[271] ©1996 NACE International. (e) Propagation rate vs 1/T for Alloy 600 exposed to 10% NaOH in MA and TT heat treatments. The circle symbols identify specimens strained at 0.2%, and the squares represent a composite of all test specimens. From Jacko.[268] (f) % room temperature yield strength vs time-to-fail for heat-treated and as-received heat treatments exposed in 10% NaOH. From Theus.[276]*

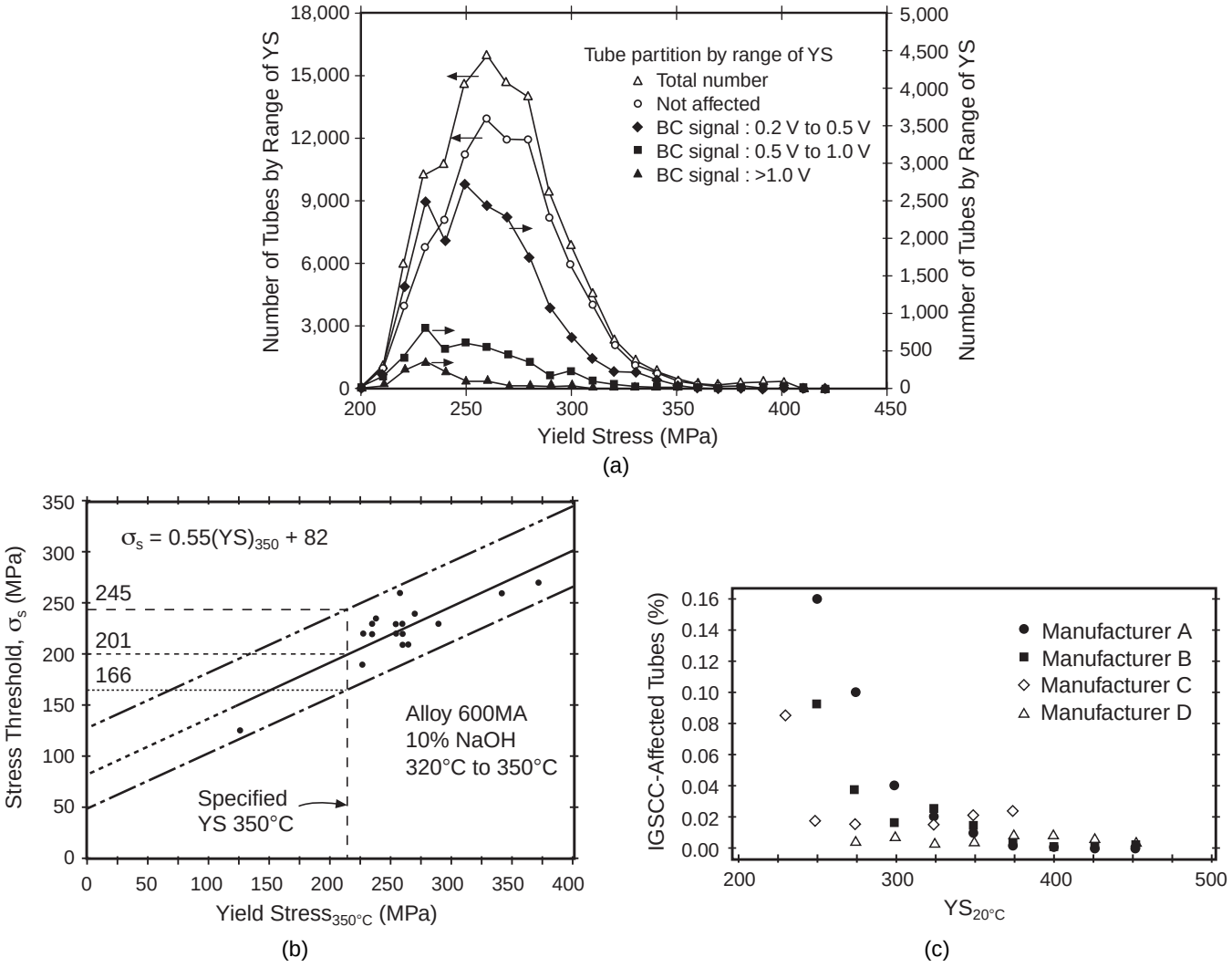

FIGURE 100. *(a) Number of tubes of given yield strength for total examined; total not affected by corrosion and totals with various voltages in Bobbin Coil examination for tubes taken from 30 steam generators. Data from tubes produced by a single manufacturer. From Vaillant, et al.[270] Courtesy of TMS, Warrendale, Pennsylvania. (b) Threshold for SCC vs yield stress at 350°C for Alloy 600MA in 10% NaOH over a range of 320°C to 350°C. From Vaillant, et al.[270-271] (c) Percent of tubes affected by IGSCC from French plants vs yield strength at 20°C for four manufacturers of tubing. From Vaillant, et al.[271] ©1996 NACE International.*

From the point of view of minor elements in the metal, Figure 97(d) shows that boron somewhat accelerates AkSCC, but the effect is small.

5. Alloy Structure

The major considerations of alloy structure with respect to AkSCC are distributions of carbides, sensitization, and cold work. The research on cold work is not extensive, but the effects would not be expected to be different from other submodes, such as LPSCC, where effects of cold work have been investigated extensively. Effects of carbide distribution and sensitization are shown in Figure 99. Since the work of Blanchet, et al.,[80] the improvement in resistance to AkSCC as well as LPSCC from sensitization and thermal treatment has been well known. This response is contrary to the proneness of sensitized Alloy 600 to HPSCC. This increased resistance to AkSCC provided by sensitization is partly related to the high nickel in the grain boundary of sensitized Alloy 600.

Figure 99(a) shows that the solubilities of carbon in Alloys 600 and 690 are both significantly lower than for Alloy 800, and the solubility of carbon in Alloy 690 is lower than for Alloy 600. This difference in solubilities has required different mill annealing temperatures and thermal treatment times and temperatures for Alloy 690 relative to Alloy 600, e.g., mill annealing at 1,000°C for Alloy 600 and >1,070°C for Alloy 690. Thermal treatment at 700°C for 15 h is required for Alloy 600 and at 716°C for 10 h for Alloy 690. Figure 99(b) shows the time to peak sensitization for Alloy 600; these data provide a basis for choosing optimum conditions for thermal treatment.

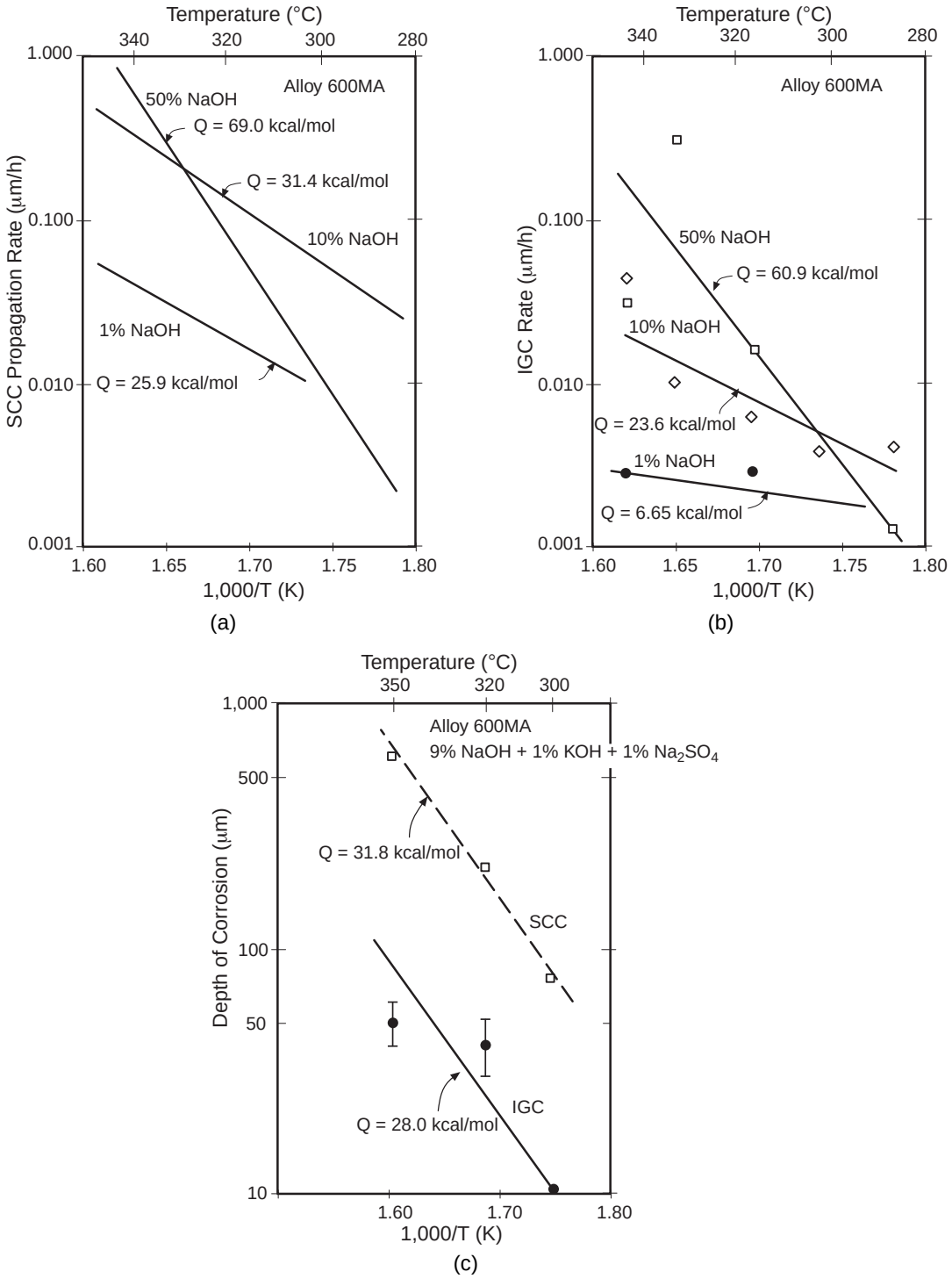

FIGURE 101. *(a) SCC propagation rate vs 1,000/T for AkSCC of Alloy 600MA in various concentrations of NaOH. From Jacko, et al.[268] (b) IGC rate constant vs 1,000/T for Alloy 600MA for various concentrations of NaOH. From Jacko et al.[268] (c) Depth of penetration vs 1,000/T for Alloy 600MA C-rings tested for 240 h in 9% NaOH + 1% KOH + 1% Na_2SO_4. From Pathania.[277]*

The effect of carbon concentration on the crack depth in NaOH of Alloy 600MA is shown in Figure 99(c). Here, about 0.030% carbon seems about optimum for reducing the rate of crack growth but lower concentrations promote substantial increases in crack depth.

The sensitivity of Alloy 690MA to AkSCC from the combined influences of carbon concentration and temperature of MA is shown in Figure 99(d) as a function of carbon concentration and MA temperature. Here, lower mill annealing temperatures are

TABLE 21

Stress Corrosion Tests for Alloy 600 in Argon/Steam Atmosphere[A]

Test No.	Test Stress	%RT Yield[B]	Test Duration (h)	Temp. (°C)	Corrodent + Steam/Argon	Results
Variable Stress Tests—Uniaxial Tensile Samples						
1	20	59	400	371	NaOH	No cracking
2	25	73	400	371	NaOH	No cracking, incipient intergranular penetration
3	30	88	400	371	NaOH	Intergranular cracking
4	40	118	305	371	NaOH	Intergranular cracking
5	20	59	1,200	426	NaOH	No cracking, incipient intergranular cracking
6	25	73	1,500	426	NaOH	No cracking, incipient intergranular penetration
7	27.5	81	89[C]	426	NaOH	Intergranular cracking
8	30	88	151	426	NaOH	Complete fracture
Corrodent Variable						
4	40	118	305	371	NaOH	Intergranular cracking
9	40	118	307	371	NaOH-Na_2CO_3	Intergranular cracking
10	40	118	308	371	Na_2CO_3	No cracking
Temperature Variable						
11	40	118	353	260	NaOH	No cracking
12	40	118	311	302	NaOH	Slight intergranular cracking
13	40	118	306	316	NaOH	Intergranular cracking
4	40	118	305	371	NaOH	Intergranular cracking
8	30	88	151	426	NaOH	Complete fracture

[A] From Kramer and Michael.[274] ©1975 NACE International.
[B] 34 ksi at 0.2% offset.
[C] Thermocouple failure.

shown to produce AkSCC at progressively lower carbon concentrations. Finally, as shown in Figure 99(e) for Alloy 600, the rate of AkSCC propagation is significantly slower for TT than for MA treatments; and sensitizing clearly increases the threshold stress for AkSCC in 10% NaOH as shown in Figure 99(f).

In general, the preferential occurrence of carbides at grain boundaries of Alloy 600MA (not sensitized) does not affect AkSCC or the other submodes as it does LPSCC. In fact, there is no correlation between the distribution of carbides and AkSCC according to Jacko[268] and Vaillant.[269]

The array of possible microstructures of Alloys 600 and 690 produces significant effects on corrosion and contributes to the wide range of heat-to-heat variations observed in practice as described in Figure 108 in Section 5.2.2.

Alloy composition and microstructure that are produced by various fabrication histories affect the yield strength. In turn, the yield strength seems to affect the proneness to AkSCC. Figure 100(a) from Vaillant and coworkers[270-272] shows data from tubes, which were pulled from 30 steam generators for a number of tubes with ranges of yield stress in terms of the total number examined, the total not affected by corrosion damage, and the totals having Bobbin Coil (BC) indications of various intensities. This figure shows first the general distribution of yield strength for the population of tubes. Second, the damage seems to be greatest in the lower range of yield strengths. The damages shown in Figure 100(a) include those from the tops of the tubesheet of both longitudinal and circumferential types and from drilled hole tube supports.

Following the implication of affected tubes in Figure 100, proneness to AkSCC increases with lower yield strength. A correlation for this effect has been developed by Vaillant and coworkers[270-272] and is shown in Figure 100(b) together with a correlation equation for Alloy 600 in 10% NaOH in the temperature range from 320°C to 350°C. The extent to which this can be extrapolated to lower values of yield stress is not clear; but, in the range of the data, the correlation appears credible.

The values of yield strength and the relative proneness to IGSCC as determined by measurements in French plants for four manufacturers is shown in Figure 100(c). This variability is similar to that shown in Figure 108.

From the data of Figure 100 it is not clear whether the main influence on SCC is the yield strength or the microstructure. However, the yield strength is a more accessible variable. There are also fundamental reasons for the lower yield strengths to exhibit lower thresholds for SCC relating to the ease and morphology of surface slip. Further, Figure 100 implies that the field failures shown in Figures 100(a) and (c) are due to AkSCC. This is questionable.

Finally, with respect to effects of surface condition on AkSCC, the data from Table 20, from Vaillant

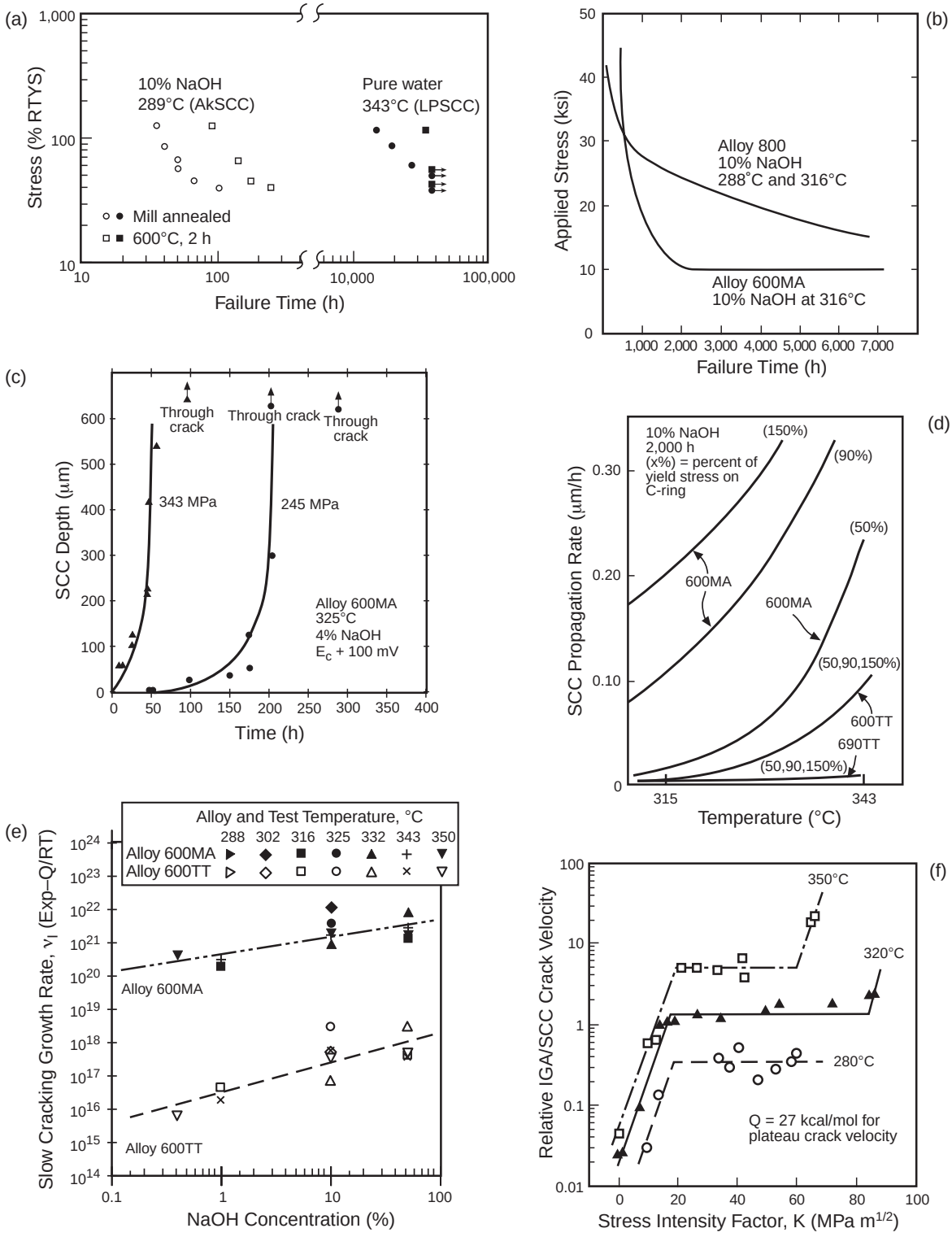

FIGURE 102. *(a) Stress vs time for AkSCC and LPSCC for Alloy 600MA. LPSCC at 343°C and AkSCC at 289°C in 10% NaOH. From Theus.[278] (b) Stress vs time for Alloy 800 in 10% NaOH at 288°C and 316°C for Alloy 600MA in 10% NaOH at 316°C. From Wilson, et al.[279] ©1975 by the American Nuclear Society, La Grange Park, Illinois. (c) SCC depth vs time for Alloy 600MA at 325°C exposed to 4% NaOH and E_c+100 mV for two stresses. Specimens taken from SG tubes. From Nagano, et al.[123] ©1990 NACE International. (d) Propagation rate vs temperature for Alloys 600MA, 600TT, and 690TT for various stresses exposed to 10% NaOH. From Smith, et al.[280] ©1985 by the American Nuclear Society, La Grange Park, Illinois. (e) Slow crack growth vs NaOH concentration for Alloy 600MA and Alloy 600TT with temperatures normalized by an exponential fit. From Vaillant, et al.[270] Courtesy of TMS, Warrendale, Pennsylvania. (f) Relative IGA/SCC crack velocity vs stress intensity for three temperatures for Alloy 600MA in 20% NaOH + 4% Na_2CO_3 solution. (For a relative crack velocity of 1.0, the absolute crack velocity is 0.37 μm/h). From Kawamura and Hirano.[260] Courtesy of TMS, Warrendale, Pennsylvania.*

and Stutzman,[257] show that electropolished surfaces are virtually immune to SCC over the ranges of conditions studied. This shows that abraded OD surfaces on Alloy 600MA strongly increase susceptibility to SCC.

6. Temperature

AkSCC of Alloy 600 has been observed at temperatures as low as 100°C.[273] However, in general, AkSCC follows a conventional 1/T relationship depending on the concentrations of NaOH, as shown in Figure 101(a).[268] A corresponding relationship is shown for IGC in Figure 101(b). The IGC also is related more to the region of lower potentials, as shown in Figure 97(b). These activation energies are in the range from 20 kcal/mol to 70 kcal/mol depending on the concentrations and a rationalization is speculative. However, the occurrence of ODSCC at the tube supports as shown in Figure 18(b) exhibits apparent activation energies in the range from 110 kcal/mol to 346 kcal/mol. This comparison suggests that the latter are somehow related to superheat and possibly to the accumulation of chemicals.

The observation that the apparent activation energies for both AkSCC and IGC increase with increasing concentrations suggests that their mechanisms are controlled by chemical processes at the low concentrations and by metallurgical processes at the high concentrations. However, what this means in detail is not clear. Further, while creep could be the metallurgical process for AkSCC, such an influence of stress is less applicable for AkIGC.

Comparable experiments for AkSCC and AkIGC are shown in Figure 101(c) where, again, the activation energies are essentially the same for the two modes although the rate of AkSCC is greater.

Table 21 from Kramer and Michael[274] shows the qualitative effects of increasing temperature from 260°C to 427°C where complete penetration by AkSCC is observed at 427°C. Similar data are shown in Figure 102(d) for Alloys 600MA, 600TT, and 690TT. The dependence of the crack growth rates on temperature for these materials decreases in the same order. An activation energy of 27 kcal/mol is shown for plateau velocities in Figure 102(f).

7. Stress

At a given stress, AkSCC occurs more rapidly than LPSCC, and the threshold for specimens having smooth surfaces is lower, as shown in Figure 102(a). The relative stress dependencies for Alloy 600 and Alloy 800 are compared in Figure 102(b). The behavior of Alloy 600 is significant for its relatively lower threshold stress of the two alloys. This relatively greater susceptibility of Alloy 600 is shown also as a function of concentration of NaOH in Figure 88(a).

In the case of propagation of AkSCC, Figures 88(b), 88(c), 102(c), 102(d), and 102(e) show crack propagation as a function of alloy, concentration of NaOH, stress, and temperature. In Figure 102(c), crack growth vs time starting with smooth surfaces is measured at two stresses. The pattern suggests a slow initiation step followed by a rapid propagation. Plateau velocities as a function of temperature and NaOH in Figures 102(f), 88(b), and 88(c) indicate that Alloys 600MA and 690TT exhibit relatively broad plateau ranges for crack velocity vs stress intensity. Figure 102(d) exhibits a significant dependence on stress for Alloy 600MA, where there are negligible dependencies on stress for Alloy 600TT and Alloy 690TT in 10% NaOH. The crack growth rates at the plateau velocity are more rapid at the higher concentrations of NaOH (Figure 102[e]) than for LPSCC (Figure 117). As the concentration of NaOH decreases, the plateau velocities decrease as in Figure 102(e) and in Figures 88(b) and (c). Figure 117 shows that as concentrations of NaOH decrease, the plateau velocities decrease and are more like those of LPSCC.